Monte Carlo-Based Reconstruction for Positron Emission Tomography

Monte Carlo-gebaseerde reconstructie voor positron emissie tomografie

Long Zhang

Promotoren: prof. dr. S. Vandenberge, prof. dr. ir. S. Staelens
Proefschrift ingediend tot het behalen van de graad van
Doctor in de Ingenieurswetenschappen: Biomedische Ingenieurstechnieken

Vakgroep Elektronica en Informatiesystemen
Voorzitter: prof. dr. ir. J. Van Campenhout
Faculteit Ingenieurswetenschappen en Architectuur
Academiejaar 2010 - 2011

UNIVERSITEIT
GENT

ISBN 978-90-8578-418-0
NUR 954
Wettelijk depot: D/2011/10.500/22

Universiteit Gent
Faculteit Ingenieurswetenschappen
Vakgroep Elektronica en Informatiesystemen

Monte Carlo-gebaseerde reconstructie voor positron emissie tomografie (PET)

Monte Carlo-based Reconstruction for Positron Emission Tomography (PET)

Long Zhang

Proefschrift tot het bekomen van de graad van
Doctor in Engineering:
Biomedical Engineering
Academic year 2010-2011

Ghent University
Faculty of Engineering
Department of Electronics and Information Systems

Promotoren: Prof. Dr. Stefaan Vandenberghe
Prof. Dr. Ir. Steven Staelens

Ghent University
Faculty of Engineering

Department of Electronics and Information Systems
Sint-Pietersnieuwstraat 41, B-9000 Gent, Belgium

This work was supported by the scholarship from the FWO (Fonds voor Wetenschappelijk Onderzoek, www.fwo.be) and Ghent University.

Proefschrift tot het behalen van de graad van
Doctor in Engineering:
Biomedical Engineering
Academic year 2010-2011

Acknowledgement

People often fail to realize that doing one's favorite job as a career is the most expensive luxury in the world. I was lucky that I joined MEDISIP, where I got such an opportunity and met people who were willing to help me to fulfill my dream. I would like to say thank you to all these people.

First of all, my thanks go to prof. dr. Ignace Lemahieu, who opened the gate to nuclear medicine imaging for me to start my PhD on a favorite topic of mine and kept helping me during this journey. I also would like to thank my promoters, prof. dr. Stefaan Vandenberghe and prof. dr. ir. Steven Stalens. Prof. dr. Stefaan Vandenberghe helped me the most on both my scientific research and my living in Belgium. He always has the correct answer to problems I encounted in my research. His brilliant ideas, deep thoughts and keen insight on research and future trends in nuclear medicine ensured my research to stay in the correct direction. He also helped me to go through the culture shock and much more, such as apartment renting and movement, etc. My thanks also go to prof. dr. ir. Steven Staelens. His suggestions usually hit the point of my problem and clarify the confusion of my research.

I also want to express my gratitude to the senior researchers in the nuclear medicine group, dr. Roel Van Holen and dr. Jan De Beenhouwer. Much of gratitude owns to dr. Roel Van Holen for his keen insight on my research, particularly in understanding ringing artifacts and performing experiment-based PSF modeling. I wish to thank dr. Jan De Beenhouwer for his innovative ideas and insights on Monte Carlo simulations for PET modeling.

In addition, my gratitude owns to all my former colleagues. Particularly, I am grateful to Yves, my first office mate, for his funny stories and help on the visiting VISA of my wife; Jeroen, for his explanation of many everyday products and many weekends spent together at INW; Peter (Van Hese), for his jokes during lunch at K12 and sharing stories about his cat to me; Mahir, for sharing me the history of middle Asia; Els, for teaching me her shopping experiences; Sara, for her desserts, which were as sweet as her; Erwann, for helping to find my first apartment in Gent, where I stayed for almost four years; Tom, for his funny stories, particularly those made after he was drunk; Eva, for her sunny smiles, and Steven (Deleye), for his

help on my trip to Brugge and lots of knowledge on football.

I would like to express my gratitude to my current colleagues. Much of gratitude is owed to Rita, the first Medisiper I met in person, who gave me lots of help; Anne-Marie, for her sweat small talks; Ayfer, for her pleasant laughter; Saskia, for sharing her experiences on children care; Roel, for his laughter and jokes through many parties; Jan, for his help on breaking the culture shock of mine; Hans, for his help on matrices and statistics; Enrico, for explaining me what "short gun" means; Vincent, for correcting my misunderstanding of allergy source with his knowledge on medicine; Pieter (Van Mierlo), for my cute nick name, longske (little long); Pieter (Mollet), for discussions on mathematics; Karel, for sharing his experiences on electronics and mechanical design; Bert, for his help on the cluster; Karen, for her help on planning a trip to Germany; Victoria, for teaching me Spanish; Hendrik, for teaching me Dutch; Kasper, for his help on translating my *artikel* into Dutch; Gregor for showing amazing slides on "mouse control" by analyzing EEG signals; Sinem, for her delicious Turkish food, and my new office-mates, Faruk, for showing me many useful Linux commands and other interesting stuffs, and Samuel for providing information on potential postdoc openings.

Next, I would like to thank all my collaborators. I wish to express my thanks to prof. dr. ir. Yves D'Asseler and his colleagues, for their help on preparing phantom, data acquisition and reconstruction at PET/CT center; Nurses at the PET/CT center (sorry for forgetting your names), for their help and tolerance the inconvenience during my PSF experiment; dr. Jeroen Verhaeghe, for sharing his experiences with scanners at UZ Gent; prof. dr. Iwan Kawrakow at NRC Canada, for his genius work on the development of egs_pet and insightful discussions on variance reduction techniques for resolution modeling in PET; dr. Juergen Scheins at FZ Julinch, for his wonderful talk and discussions on symmetries handling in PET reconstruction; Christopher Cloque at ULB, for his help and insightful discussions on resolution modeling for PET; S. Nasel and P. George from Philips Belgium, for their support on using the scanners at UZ. Your selfless help greatly accelerated the progress of my research.

Finally, I want to dedicate this work to my parents, family and friends, who have always supported me whenever needed. Particularly, my thanks go to my wife and my little. Without your support and encouragement, it would never been possible for me to complete this work and write these words.

Ghent, Jan 2011
Long Zhang

Table of Contents

Acknowledgement **i**
List of symbols xvii

Nederlandstalige samenvatting **xxvii**

English summary **xxxi**

1 Introduction **3**
1 Background 3
2 Organization of this dissertation 5

2 Positron Emission Tomography **7**
2.1 General Introduction 7
2.2 The Principle of PET 8
2.3 Nuclear medicine imaging physics 9
2.3.1 Common radiation forms in nuclear medicine 9
2.3.2 Interaction of β particles with matter 11
2.3.3 Interaction of Photons with Matter 12
2.3.3.1 Rayleigh scattering 12
2.3.3.2 Photoelectric Effect 13
2.3.3.3 Compton (incoherent) scattering 13
2.3.3.4 Pair production 13
2.4 PET Instrumentation 14
2.4.1 Geometry 14
2.4.2 Physics 14
2.4.2.1 Object Photon Attenuation 14
2.4.2.2 Physics in the scintillation detector 16
2.4.3 Detectors 17
2.4.3.1 PMT 17
2.4.3.2 Block detectors design 19
2.4.3.3 Energy resolution 20
2.4.4 Coincidence logic 20
2.4.4.1 Time of flight PET 21

2.4.5 Image quality degradation factors 22
2.4.5.1 Crystal penetration 22
2.4.5.2 Intercrystal scattering 22
2.4.5.3 Randoms 24
2.4.5.4 Scatters 24
2.4.5.5 Photon attenuation 26
2.5 PET Reconstruction 26
2.5.1 Problem formulation 28
2.5.2 Major Components in Iterative Reconstruction Algorithm 29
2.5.2.1 Object parameterization 29
2.5.2.2 System model 30
2.5.2.3 Statistical model 34
2.5.2.4 Cost function 35
2.5.2.5 Optimization algorithm 35
2.5.3 Quantitative techniques in PET reconstruction 36
2.5.3.1 Randoms correction 36
2.5.3.2 Attenuation correction 37
2.5.3.3 Scatter correction 37
2.6 Monte Carlo simulation in PET 38
2.7 General conclusion 41

3 VRTs in Resolution Modeling 43
3.1 Introduction 43
3.2 Materials and Methods 44
3.2.1 Figures of merit 44
3.2.1.1 Precision 44
3.2.1.2 Efficiency evaluation 45
3.2.2 SM simulation 45
3.2.3 Implemented variance reduction techniques 46
3.2.3.1 Polar angle biasing 46
3.2.3.2 Hit-testing 47
3.2.3.3 Positron history reuse 48
3.2.3.4 Forced the energy window passing 48
3.2.3.5 Fictitious transport in the crystal array 49
3.2.3.6 Transport parameters 50
3.2.4 Validation and efficiency evaluation 50
3.3 Results 51
3.3.1 Validation results 51
3.3.2 Precision and efficiency evaluation 51
3.4 Discussion and future work 55
3.5 Conclusion and original contribution 57

4 Resolution Modeling using Cubic Voxels **59**
4.1 Introduction . . . 59
4.2 Materials and Methods . . . 60
4.2.1 Imaging geometry . . . 60
4.2.2 System matrix simulation . . . 61
4.2.2.1 Simulation setup . . . 61
4.2.2.2 Symmetry handling . . . 62
4.2.2.3 System matrix quality index . . . 62
4.2.3 System matrix storage . . . 65
4.2.4 The rotator-based OS-EM . . . 65
4.2.5 Image quality evaluation . . . 66
4.2.6 Simulation study . . . 67
4.2.7 Measurement study . . . 67
4.3 Results . . . 68
4.3.1 System matrix quality index . . . 68
4.3.2 Calculation time . . . 69
4.3.3 Storage of the system matrix . . . 69
4.3.4 Image quality evaluation . . . 70
4.3.4.1 Simulation study . . . 70
4.3.4.2 Measurement study . . . 70
4.4 Discussion . . . 71
4.5 Conclusions and original contribution . . . 76

5 Experiment-based Resolution Modeling **77**
5.1 Introduction . . . 77
5.2 Materials and Methods . . . 78
5.2.1 The scanner . . . 78
5.2.2 PSF measurement . . . 78
5.2.3 PSF modeling . . . 80
5.2.3.1 Radial blurring modeling . . . 83
5.2.3.2 Axial blurring modeling . . . 86
5.2.4 System matrix construction . . . 88
5.2.5 Reconstruction . . . 90
5.2.6 Figures of merit . . . 90
5.2.7 Resolution properties . . . 92
5.2.8 Phantom study . . . 93
5.2.8.1 Jazsczak phantom . . . 93
5.2.8.2 Hoffman phantom . . . 93
5.3 Results . . . 94
5.3.1 Resolution properties . . . 94
5.3.2 Image quality evaluation . . . 95
5.3.2.1 Jazsczak phantom . . . 95
5.3.2.2 Hoffman phantom . . . 96
5.4 Discussion . . . 96
5.5 Conclusions and original contributions . . . 106

6 Ringing Artifacts in Resolution Modeling **107**
6.1 Introduction . . . 107
6.2 Theory . . . 108
6.2.1 The Ideal Rotator . . . 108
6.2.2 Analytical modeling of positron range and acolinearity . . 109
6.3 Materials and Methods . . . 109
6.3.1 The PET scanner . . . 109
6.3.2 System Matrix Simulation . . . 109
6.3.3 Figures of merit . . . 112
6.3.3.1 Contrast recovery . . . 112
6.3.3.2 Artifacts Evaluation . . . 113
6.3.4 Image reconstruction . . . 114
6.3.5 Noiseless Data Studies . . . 114
6.3.6 Simulation Studies . . . 115
6.3.7 Experimental Studies . . . 115
6.4 Results . . . 116
6.4.1 Noiseless Data Studies . . . 116
6.4.2 Simulation Studies . . . 116
6.4.3 Experimental Studies . . . 122
6.5 Discussion and future work . . . 130
6.6 Conclusion and original contributions . . . 134

7 General Conclusion **137**
7.1 Main conclusions . . . 137
7.2 Future work . . . 141

List of Figures

2.1 Illustration of the work flow in a real world PET examination. . . 9

2.2 Typical geometric setups in PET scanners. (a) Flat panel detectors with large detector blocks. This configuration has better sensitivity and more regular in-plane sampling. (b) Cylindrical PET scanner with small detector blocks. This configuration optimizes the system sensitivity and is the most popular geometry for commercial PET scanners. (c) PET scanners using monolithic curvature detector. This configuration optimizes the system sensitivity and event localization. (d) Two rotating-head-detector. This configuration is the most economic setup that meets the minimal requirements for PET imaging. 15

2.3 Schematic diagram of a photomultiplier tube. 18

2.4 2.4a A schematic illustration of the concept of a block detector, also called Anger logic or the Anger camera. The energy is the sum of signals of the four PMTs. The position of the event can be determined by the light share among illuminated PMTs or (b) positioning by numerical analysis. A 2D block map of a 6x6 BGO crystal array viewed by four PMTs. The relative light output is indicated by the isocount curves. The heavy white lines indicate which region is assigned to a crystal. 20

2.5 Illustration of coincidence detection. For an annihilation event, the two annihilation photons are detected. A pulse is formed on each detector channel. This pulse may trigger a window signal on the coincidence channel. If a second pulse appears within the window signal, a coincidence is formed between the two pulses. 21

2.6 Crystal penetration causes the parallax error. This effect can be found in a ring PET scanner composed of pixelized block detectors and most notably for LORs at the edge of FOV. The axial parallax error is not as pronounced as depicted because the length of the crystal is usually negligible compared to the radius of the scanner ring. 23

2.7 Illustration of the inter-crystal scattering. The positioning error is caused by the loss of information in photon detection. Unlike the parallax error, the positioning error caused by inter-crystal scattering cannot be formulated and solved in a closed form due to the difficulties in describing the geometry of a scanner. This effect is usually estimated by Monte Carlo simulation 23
2.8 Types of coincidneces: trues (left), scatters (middle) and randoms (right). 25
2.9 An example of the mesh object parameterization. 30
2.10 Representing a continuous object (1-D) by smooth basis functions and pixels. Courtesy Dr. J. A. Fesseler. 31
2.11 The user code - EGSnrc interface. The user code first initializes the EGSnrc package with user provided macro files. After initialization, the user code guides the transport of particles through the *howfar* and *hownear* routines. The score is extracted from the simulation in the routine *ausgab*. Courtesy NRC, Canada 40

3.1 The effective range of the polar angle is location-dependent. The maximum effective range of the polar angle is found at the edge of the FOV; the minimum effective range of the polar angle is found at the center of the FOV. 47
3.2 Illustration of the concept of forced passing the energy threshold. . 49
3.3 Point spread functions of the VRT simulation and the baseline simulation for a voxel source at the center of the FOV. 52
3.4 Point spread functions of the VRT simulation and the baseline simulation for a voxel source at 25 cm off-center. 53
3.5 The efficiency was plotted as a function of the number of reuse. The efficiency of a simulation using back-to-back gamma source was also plotted. 54

4.1 (NOT TO SCALE) Symmetries. (a) Axial symmetry. SM elements associated with crossed LORs are interchangeable under a mirror operation. SM elements associated with LORs in parallel are identical. (b) Rotational symmetry. The two SM elements are identical given detector blocks are identical. 63
4.2 (NOT TO SCALE) The base-symmetry LORs. (a) Axial base-symmetry LORs. (b) In plane base-symmetry LORs (Only two views were drawn for clarity). 64
4.3 Reconstruction examples. (a) Multi-ray Siddon projector method (iter 4, 22 subsets). (b) MCSM method (iter 4, 22 subsets). Ringing artifacts indicated by white arrows. 70
4.4 Contrast versus noise curves of the simulation study, each point represents one OS-EM iteration with 22 subsets. (a) Contrast-noise curve for hot lesions (b) Contrast-noise curve for cold lesions. 71

4.5 Reconstruction examples. (a) The spheres of the clinical software. (b) Cold rods of the clinical software. (c) The spheres of the MCSM method. (b) Cold rods of the MCSM method. 72
4.6 Profile extracted through 11.1- and 7.9-mm cold rods. 73
4.7 Contrast noise trade-offs of the measured data, each point represents a single iteration. (a) Hot lesions. (b) Cold lesions. 74
4.8 The Gaussian rotator blurs the PSF obtained by simulation. 75

5.1 The robot 79
5.2 The sampling grids in the x-y (transverse) plane. The grid area is slightly larger than the triangle formed by the origin, the middle of the detector block and the middle point of the two adjacent blocks. 81
5.3 Schematic drawing of the sampling grid in the z (axial) direction. . 82
5.4 The principle of the parameterization-based technique. The unknown PSF (dotted line) is obtained indirectly: the measured PSFs are first parameterized with a proper model. Another model is then fitted to the parameters. The unknown PSFs are finally sampled from the model of the parameters. 82
5.5 Fitting examples for a point source that is 1 cm off-center in measurement plane 0, (a) slice of ring pair (15,15), (b) slice of ring pair (15, 16). 84
5.6 An example of fitting models to the parameters at the slice of ring pair (15, 15) for point sources in the measurement plane 0. (a) (b) The parameter A and σ are fitted to a parabola function of the locations of point sources. (c) The parameter ρ is fitted to Equation 5.2 of the locations of point sources. 85
5.6 An example of fitting models to the parameters at the slice of ring pair (15, 15) for point sources in the measurement plane 0. (a) (b) The parameter A and σ are fitted to a parabola function of the locations of point sources. (c) The parameter ρ is fitted to Equation 5.2 of the locations of point sources. 86
5.7 An example of fitting models to the parameters at the slice of ring pair (15, 16) for point sources in the measurement plane 0. (a) (b) The parameter A and σ are fitted to a parabola function of the locations of point sources. (c) The parameter ρ is fitted to Equation 5.2 of the locations of point sources. 87
5.7 An example of fitting models to the parameters at the slice of ring pair (15, 16) for point sources in the measurement plane 0. (a) (b) The parameter A and σ are fitted to a parabola function of the locations of point sources. (c) The parameter ρ is fitted to Equation 5.2 of the locations of point sources. 88
5.8 An illustration of the proposed PSF model. 89

5.9 The PSF model and the radial and axial profile components. It can be seen that the PSF model is naturally a summation of all radial profiles. A summation model allows different radial profiles in different slices. This PSF model may degrade into a separable model if all the radial profiles have the same shape across different slices. 89
5.10 The forward- and back-projector. (a) The forward projection operation using the factorized matrix approach. (b) The backprojection operation using the factorized matrix approach. 91
5.11 Volumetric resolution of the PSF modeling (with or without axial blurring), the Monte Carlo-based method and the OSEM Siddon approach. The volumetric resolutions were measured at the fifth iteration with 23 subsets. 94
5.12 The volumetric resolution as a function of point source locations at the 5th iteration of the standard OS-EM using Siddon projector and the proposed method with and without axial blurring. 95
5.13 The mean volumetric resolution as a function of iteration number for a point source at the center of the FOV and a point source 10 cm off-center. 96
5.14 Reconstruction examples for the proposed method without axial blurring. (a), (d) and (g) show the transverse, coronal and sagittal views, respectively, of the model without axial blurring. (b), (e) and (h) show the transverse, coronal and sagittal views, respectively, of the model with axial blurring. (c), (f) and (i) are the transverse, coronal and sagittal views, respectively, of manufacture's method. 97
5.14 Reconstruction examples for the proposed method without axial blurring. (a), (d) and (g) show the transverse, coronal and sagittal views, respectively, of the model without axial blurring. (b), (e) and (h) show the transverse, coronal and sagittal views, respectively, of the model with axial blurring. (c), (f) and (i) are the transverse, coronal and sagittal views, respectively, of manufacture's method. 98
5.14 Reconstruction examples for the proposed method without axial blurring. (a), (d) and (g) show the transverse, coronal and sagittal views, respectively, of the model without axial blurring. (b), (e) and (h) show the transverse, coronal and sagittal views, respectively, of the model with axial blurring. (c), (f) and (i) are the transverse, coronal and sagittal views, respectively, of manufacture's method. 99
5.15 Contrast noise trade-offs of the image quality phantom. Each point represents a single iteration of the proposed method (PSF modeling with axial blurring), the Monte Carlo-based method and the manufacture's method (Philips). (a) Hot lesions. (b) Cold lesions. 100

5.16 Contrast noise trade-offs of the image quality phantom. Each point represents a single iteration of the proposed method with or without axial blurring in the system model. (a) Hot lesions. (b) Cold lesions. 101

5.17 Hoffman phantom at the 10th iteration. (a) (c) (e) The transverse, coronal, and sagittal view of the image reconstructed by the PSF method. (b) (d) (f) The transverse, coronal, and sagittal views of the image reconstructed by the clinical software. 102

5.17 Hoffman phantom at the 10th iteration. (a) (c) (e) The transverse, coronal, and sagittal view of the image reconstructed by the PSF method. (b) (d) (f) The transverse, coronal, and sagittal views of the image reconstructed by the clinical software. 103

5.17 Hoffman phantom at the 10th iteration. (a) (d) (g) The transverse, coronal, and sagittal view of the image reconstructed by the PSF method. (b) (e) (h) The transverse, coronal, and sagittal view of the image reconstructed by the Monte Carlo method. (c) (f) (i) The transverse, coronal, and sagittal views of the image reconstructed by the clinical software. 104

6.1 (NOT TO SCALE) Illustration of polar-pixel topology and image rotation. (a) Polar-pixel discretization. (b) Image rotation is "ideal" for radial symmetry positions. 108

6.2 Overall blurring of positron range and acolinearity (a) at the center and (b) at the edge (288 mm off-center) of the FOV. (c) FWHM as a function of the off-center distance 110

6.2 Overall blurring of positron range and acolinearity (a) at the center and (b) at the edge (288 mm off-center) of the FOV. (c) FWHM as a function of the off-center distance 111

6.3 ROI definitions. (a) ROI for lesions. (b) ROI for artifact evaluation: dark annular ROIs are for cold lesions and the edge of the background; white circular ROIs within hot lesions are for hot lesions. 113

6.4 The Ring Index (RI) for hot lesions. Left: artifact-free image, RI equals to 1; Middle: taper artifacts, RI > 1; Right: ringing artifacts, RI < 1. 114

6.5 Artifact illustration with noiseless data (a) Gaussian rotator method with SM $A^{p,v}$. (b) Gaussian rotator method with SM $A^{g,v}$. (c) Ideal rotator method with SM $A^{p,pol}$. 117

6.6 Artifact illustration with noiseless data. (a) and (b) Profiles extracted through hot lesions. 118

6.7 Artifact evaluation indices for different methods, PV: Gaussian rotator method with SM $A^{p,v}$, GV: Gaussian rotator method SM $A^{g,v}$, PPol: ideal rotator method with SM $A^{p,pol}$. (a) Ringing indices for hot lesions. (b) Ringing indices for cold lesions. (c) Ringing indices for the edge of the background. (d) Contrast recovery at 20th iteration. 119

6.7 Artifact evaluation indices for different methods, PV: Gaussian rotator method with SM $A^{p,v}$, GV: Gaussian rotator method SM $A^{g,v}$, PPol: ideal rotator method with SM $A^{p,pol}$. (a) Ringing indices for hot lesions. (b) Ringing indices for cold lesions. (c) Ringing indices for the edge of the background. (d) Contrast recovery at 20th iteration. 120

6.8 Artifact depiction in simulation data. Top row is of the high count study and bottom row is of the low count study. (a) Gaussian rotator method with SM $A^{p,v}$ of the high count study. (b) Gaussian rotator method with SM $A^{g,v}$ of the high count study. (c) Ideal rotator method with SM $A^{p,pol}$ of the hight count study. (d) Gaussian rotator method with SM $A^{p,v}$ of the low count study. (e) Gaussian rotator method with SM $A^{g,v}$ of the low count study. (f) Ideal rotator method with SM $A^{p,pol}$ of the low count study. 121

6.8 Artifact depiction in simulation data. Top row is of the high count study and bottom row is of the low count study. (a) Gaussian rotator method with SM $A^{p,v}$ of the high count study. (b) Gaussian rotator method with SM $A^{g,v}$ of the high count study. (c) Ideal rotator method with SM $A^{p,pol}$ of the hight count study. (d) Gaussian rotator method with SM $A^{p,v}$ of the low count study. (e) Gaussian rotator method with SM $A^{g,v}$ of the low count study. (f) Ideal rotator method with SM $A^{p,pol}$ of the low count study. 122

6.9 Profile extracted from hot lesions on simulation data. Top row is of high count and bottom row is of low count. (a) and (b) show profiles extracted through hot lesions in the high count study. (c) and (d) depicted profiles extracted through hot lesions in the high count study. 123

6.9 Profile extracted from hot lesions on simulation data. Top row is of high count and bottom row is of low count. (a) and (b) show profiles extracted through hot lesions in the high count study. (c) and (d) depicted profiles extracted through hot lesions in the high count study. 124

6.10 Artifact evaluation indices for different methods (I), PV: Gaussian rotator method with SM $A^{p,v}$, GV: Gaussian rotator method SM $A^{g,v}$, PPol: ideal rotator method with SM $A^{p,pol}$, Sid: the standard OS-EM. Top row is of the high count study. Bottom row is of the low count study. (a) Ringing indices for hot lesions in the high count study. (b) Ringing indices for the edge of the background in the high count study. (c) Ringing indices for hot lesions in the low count study. (d) Ringing indices for the edge of the background in the low count study. 125
6.10 Artifact evaluation indices for different methods (I), PV: Gaussian rotator method with SM $A^{p,v}$, GV: Gaussian rotator method SM $A^{g,v}$, PPol: ideal rotator method with SM $A^{p,pol}$, Sid: the standard OS-EM. Top row is of the high count study. Bottom row is of the low count study. (a) Ringing indices for hot lesions in the high count study. (b) Ringing indices for the edge of the background in the high count study. (c) Ringing indices for hot lesions in the low count study. (d) Ringing indices for the edge of the background in the low count study. 126
6.11 Artifact evaluation indices for different methods (II), PV: Gaussian rotator method with SM $A^{p,v}$, GV: Gaussian rotator method SM $A^{g,v}$, PPol: ideal rotator method with SM $A^{p,pol}$, Sid: the standard OS-EM. Top row is of the high count study. Bottom row is of the low count study. (a) Contrast recovery at the 20th iteration in the high count study. (b) Contrast recovery at the 20th iteration in the low count study. 127
6.12 Artifact depiction in acquired data (a) Gaussian rotator method with SM $A^{p,v}$. (b) Gaussian rotator method SM $A^{g,v}$. (c) Ideal rotator method with SM $A^{p,pol}$. (d) Profiles extracted through the largest and smallest hot lesions.. 128
6.12 Artifact depiction in acquired data (a) Gaussian rotator method with SM $A^{p,v}$. (b) Gaussian rotator method SM $A^{g,v}$. (c) Ideal rotator method with SM $A^{p,pol}$. (d) Profiles extracted through the largest and smallest hot lesions.. 129
6.13 Artifact evaluation indices for different methods, PV: Gaussian rotator method with SM $A^{p,v}$, GV: Gaussian rotator method SM $A^{g,v}$, PPol: ideal rotator method with SM $A^{p,pol}$, Sid: the standard OS-EM. (a) Ringing indices for hot lesions. (b) Ringing indices for the edge of the background. (c) Contrast recovery at the 5th iteration. 131
6.13 Artifact evaluation indices for different methods, PV: Gaussian rotator method with SM $A^{p,v}$, GV: Gaussian rotator method SM $A^{g,v}$, PPol: ideal rotator method with SM $A^{p,pol}$, Sid: the standard OS-EM. (a) Ringing indices for hot lesions. (b) Ringing indices for the edge of the background. (c) Contrast recovery at the 5th iteration. 132

List of Tables

2.1 Physical properties of scintillators commonly used in PET (the attenuation length and energy resolution are measured at 511 keV . 17

3.1 Efficiency improvement of different VRTs. 52

4.1 Philips Gemini GS PET/CT Characteristics 61
4.2 Image volume and LOR histogram configuration 61
4.3 Relationship with other indices 68
4.4 Simulation efficiency improvement 69
4.5 Storage reduction factors 69

5.1 image volume and LOR histogram configuration 78
5.2 The resolution properties from the manufacturer. Reproduced from [Surti and Karp, 2004]. 94

6.1 System matrix characteristics 112

Notation and Symbols

Notation

Vectors, Matrices, Tensors,...

x,$\mathbf{x}$,$\mathbf{X}$	scalars, vectors, matrices(tensors),...
$\mathbf{x}_i$	i-th element of vector $\mathbf{x}$
$\mathbf{X}_{ij}$	ij-th element of matrix or tensor $\mathbf{x}$

List of symbols

$\mathbf{A}$	The system matrix
$\mathbf{g}$	The measurement data vector
$\mathbf{f}$	The imaged object
$\mathbf{s}$	The noise vector
σ	The standard deviation
μ	The attenuation coefficient

Acronyms

0–9

1-D, 2-D, 3-D	1-Dimentional, 2-Dimentional, 3-Dimentional

A

ART	Algebraic Reconstruction Technique
APD	Avalanche Photo Diodes
ACF	Attenuation Correction Factor

B

BPF	BackProjection Filtration

C

CT	Computed Tomography
C-C	Continous to Continous
C-D	Continous to Discrete
CRC	Contrast Recovery Coefficient
CR	Computational Resource

D

D-D	Discrete to Discrete

E

EEG	ElectroEncephaloGram
ECG	ElectoCardioGram
EGS	Electron Gamma Shower

F

FOV	Field Of View
FWHM	Full Width at Half Maximum
fMRI	functional MRI
^{18}F-FDG	^{18}F Fluorodeoxyglucose

G

GATE	Geant4 Application for Tomography Emission
GNP	Generalized Natural Pixel
GKB	Generalized Kaiser-Bessel
GPGPU	General Purpose Graphics Processing Unit

I

IR	Ideal Rotator

L

LOR	Line Of Response
LHC	Large Hadron Collider

M

MRI	Magenetic Resonance Imaging
ML-EM	Maximized Likelihood Expectation Maximization
MAP	Maximum *a posteriori*
MART	Multiplicative ART

N

NM	Nuclear Medicine
NP	Natural Pixel

O

OS-EM	Ordered Subset Expectation Maximization

P

PET	Positron Emission Tomography
PE	Photonelectric Effect
PSF	Point Spread Function
(PS-)PMT	(Position Sensitive) Photon-Multiplier Tube

R

RAMLA	Row-Action Maximum Likelihood Algorithm
RMSE	Root Mean Square Error
RSD	Relative Standard Deviation
ROI	Regions Of Interest
RF	Radio Frequency

S

SM	System Matrix
SNR	Signal-to-Noise Ratio

SPECT	Single Photon Emission Computed Tomography
SIR(T)	Statistical Iterative Reconstruction (Technqiue)
SiPM	Silicon PM
SSS	Single Scatter Simulation
SART	Simultaneous ART
SimSET	Simulation System for Emission Tomography

T

TOR	Tube Of Response
TOF	Time Of Flight

U

US	UltraSound

V

VRT	Variance Reduction Techniques

Dutch/English Summary

Nederlandstalige samenvatting –Summary in Dutch–

Positron Emission Tomography (PET) beeldvorming is een tak van de nucleaire medische beeldvorming. Het is een relatief nieuwe en snel evoluerende modaliteit die gebruik maakt van het speurstof-principe. Zoals de naam al impliceert, maakt PET gebruik van straling gevormd door middel van positron-elektron annihilatie waarbij twee annihilatie fotonen worden uitgestuurd in tegenovergestelde richting. PET beeldacquisitie begint met het toedienen van een positron emitterend radiofarmacon in de patint. De moleculen van de speurstof zijn betrokken in fysiologische processen en worden verdeeld over het lichaam. De verdeling van het radiofarmacon onthult op zijn beurt informatie over fysiologische processen. Een PET-scanner meet de ruimtelijke informatie van alle gedetecteerde annihilatiefotonen, en organiseert deze in een histogram, genaamd sinogram. Door een reconstructieproces kunnen sinogrammen worden genverteerd en kan de verdeling van de radiotracer worden weergegeven.

Vaak wordt de data-acquisitie procedure vereenvoudigd gemodelleerd als een lijn-integraal, wat vergelijkbaar is met een verwante modaliteit: computed tomography (CT). De beeldvorming in PET is in realiteit echter heel wat complexer. Na emissie van het positron door radioactief verval van een isotoop (bvb. ^{18}F), legt dit positron een kleine afstand af vooraleer het annihileert met een elektron. Deze kleine afstand wordt het positron bereik genoemd. Na annihilatie (hetzij tijdens de vlucht of in rust), zijn de secundaire annihilatiefotonen niet perfect collineair en is er een kleine hoekafwijking ten opzichte van de gedealiseerde 180 $^\circ$ graden. Deze hoekafwijking noemt men acollineariteit. De twee annihilatiefotonen kunnen verschillende foton-materie interacties ondergaan in het lichaam van een patient. Bij Compton verstrooiing buigt het foton af van zijn oorspronkelijke pad wat gepaard gaat met energieverlies. Bij het foto-elektrische effect wordt het foton geabsorbeerd. Zodra de fotonen zijn aangekomen in de detector, kunnen nogmaals Compton verstrooiing en foto-elektrische effecten optreden. Als gevolg van al deze effecten en de beperkingen van een PET-detector, moeten we rekening

houden met een afwijking bij de waargenomen detectiepositie van elk foton.

Deze onvolmaaktheden kunnen in zekere mate worden gecompenseerd door middel van resolutie-modellering tijdens beeldreconstructie. In dit proefschrift richten we ons op het modelleren van deze degradatiefactoren tijdens het reconstructieproces om zo de beeldkwaliteit te verbeteren. Dit wordt meestal uitgevoerd aan de hand van een systeemmodel, dat alle bekende factoren omvat, gerelateerd aan een patintenscan: 1) de geometrie van de scanner, 2) de structuur van de scintillatiekristallen, 3) de energie- en tijdsresolutie, en 4) fysieke degradatiefactoren, met inbegrip van positron-bereik, de acolineariteit van de annihilatiefotonen, kristalpenetratie, en de verstrooiing tussen de kristallen onderling.

In de praktijk moeten we echter een aantal veronderstellingen maken om het genereren van een systeemmodel mogelijk te maken. Zo verschillen scanner configuraties (opnameparameters en patinten) meestal in de klinische praktijk, hetgeen het systeemmodel nog ingewikkelder maakt. Het zou nauwkeuriger zijn om een uniek systeemmodel op te stellen per opnameconfiguratie, maar dit is onhaalbaar. Daarom zijn we ervan uitgegaan dat het systeemmodel onafhankelijk is van de verschillende opnameconfiguraties. Dankzij tijdsonafhankelijke simulaties kan de koppeling tussen de verschillende gebeurtenissen gelimineerd worden. Patintafhankelijke factoren worden uitgesloten uit het systeemmodel omwille van dezelfde redenen .

Aan de hand van Monte Carlo simulaties kunnen alle bovengenoemde factoren gemodelleerd worden. Variantie Reductie Technieken (VRTs) zijn noodzakelijk voor het versnellen van simulaties van onder andere resolutie-modellering. Met de veronderstellingen uit de vorige paragraaf implementeren we een aantal eenvoudige VRTs om de simulatie-efficintie van egs_pet verder te verbeteren. De eerste techniek bestaat uit het limiteren van de polaire hoek (Eng.: Polar angle biasing), die wordt gebruikt om fotonen die niet in de richting van de detector vliegen tijdens de simulatie te elimineren. Een alternatief is om hit-tests uit te voeren om na te gaan of een foton de detector al dan niet kan raken, maar deze tests kunnen op hun beurt veel tijd in beslag nemen. 'Positron tracking' kan verder geoptimaliseerd worden door hergebruik van de positron geschiedenis van meerdere gelimineerde foton-paren. Voor het traceren van fotonen in de detector, is gebruik gemaakt van fictief transport in het kristal om de kost verbonden aan 'bound cross handling' te beperken, en 'forced energy window passing' verhoogt de simulatie-efficintie door analytisch de kans te berekenen dat een foton binnen het opgelegde energie-venster valt. Ten slotte kunnen de transportparameters geoptimaliseerd worden voor een betere efficintie, zonder verlies van nauwkeurigheid. Een geoptimaliseerde Monte Carlo simulator vormt de basis voor Monte Carlo gebaseerde resolutie-modellering, het centrale deel van dit proefschrift. In aanvulling op de eerder genoemde Monte Carlo simulator, hebben wij een nieuw rotator-gebaseerd algoritme voor beeldreconstructie voorgesteld voor het resolutie-compensatie probleem in PET. Met een rotator kan de rotatiesymmetrie in een cilindervormige PET-scanner worden uitgebuit voor alle soorten basisfuncties . Deze eenvoudige operatie verhoogt de efficintie van de resolutiemodelleringssimulatie aanzienlijk. Verder vermindert deze aanpak ook de redun-

dantie in het systeem-model, hetgeen dit systeem-model compact genoeg maakt voor een opslag op een PC. Met onze snelle Monte Carlo simulator en rotatie-gebaseerde technieken, kan op een week tijd een nauwkeurig systeem-model worden opgesteld op een klein computationeel platform.

Naast Monte Carlo-gebaseerde resolutie modellering, bespreken we ook de modellering van puntspreidingsfuncties (PSF) op basis van metingen in combinatie met het rotator-gebaseerde algoritme. De methode karakteriseert de profielen van de PSF. We voegen de belangrijkste parameters n voor n toe en evalueren telkens hun impact op de kwaliteit van het gereconstrueerde beeld. In dit werk wordt een eerste model voorgesteld. Radiale en axiale spreiding werden gemodelleerd en hun effecten op de beeldkwaliteit werden gevalueerd. Onderzoek toont aan dat axiale vervaging een kleine invloed heeft op de compensatie van de resolutie maar het contrastherstel voor kleine hete lesies verbetert. Hierdoor vormt het een belangrijke parameter in de modellering van de resolutie.

Hoewel een rotator de rotatie-symmetrie voor een Cartesiaanse discretisatie geschikt maakt, zijn er uitgesproken ringvormige artefacten in het gereconstrueerde beeld doordat een extra (artificile) vervaging gentroduceerd wordt. We karakteriseren de ringvormige artefacten in onze rotator-gebaseerde reconstructie door het toepassen van een nauwkeurig systeemmodel in een ideaal rotator-gebaseerd algoritme. De ideale rotator gebruikt polaire-pixels als basisfuncties. Omdat deze rotatiesymmetrisch zijn, vermijden ze de introductie van extra, ongewenste vervaging. De enige ringvormige artefacten die overblijven in de ideale rotator-gebaseerde aanpak behoren tot de bekende Gibbs effecten. Het verschil tussen de artefacten met de ideale rotator wordt gebruikt om de herkomst van de ringvormige artefacten in de algemene rotatorgebaseerde aanpak te onderzoeken. We onderzoeken ook de relatie tussen de artefacten en het contrastherstel voor kleine warme lesies. Dit werk suggereert dat de artefacten vooral worden toegeschreven aan de rotator. Onze studie geeft ook aan dat de ringvormige artefacten het contrastherstel van warme lesies kunstmatig verbeteren, in het bijzonder voor kleine lesies.

De ringvormige artefacten veroorzaken bias in de beelden op plaatsen waar er zich scherpe overgang van intensiteit voordoen. De artefacten zijn visueel meer uitgesproken bij ruisvrije data. In de praktijk zijn de ringvormige artefacten onzichtbaar geworden omdat er bij emissietomografie veel ruis aanwezig is in de data. De bias blijft echter in de scherpe overgangen van het beeld en duwt het contrast in de richting van de werkelijke waarde, in het bijzonder voor kleine lesies. Het verbeterde contrast kan het de detectie van kleine lesies verbeteren, dit is belangrijk in oncologie-toepassingen.

English summary

Positron Emission Tomography (PET) imaging is a branch of nuclear medicine imaging. It is a relatively new and rapidly evolving imaging modality. This imaging modality uses the tracer principle. As the name implies, PET uses radiation formed by positron-electron annihilation, which is two back-to-back (180° apart) annihilation photons. PET image acquisition begins with the administration of a positron emission radiopharmaceutical in the patient. The molecules of the radiotracer are involved in physiological processes and are distributed within the body. The distribution of the radiopharmaceutical in turn reveals information about the physiological processes. A PET scanner records the spatial information of all detected annihilation photons, organized as a histogram called a sinogram. Sinograms can be inverted into the distribution of the radiotracer through a process called reconstruction.

Often, the data acquisition procedure is simplified as a line integral model, which is similar to its sibling modality, computed tomography (CT). However, the true data formation procedure in PET is much more complex. After the positron emitted from an isotope (e.g. ^{18}F), it travels a small distance before annihilating with an electron. The small distance is called the positron range. After annihilation (either in flight or at rest), the secondary annihilation photons are not ideally collinear. Instead, the two photons fly back to back with a small angle deviation from 180°, which is called acolinearity. The two annihilation photons may undergo different photon-matter interactions in the patient body, namely Compton scattering, which deflects the photon from its original path with reduced energy, and photoelectric effects, where the photon absorbed. Once the photons arrived at the detector, Compton scattering and photoelectric effects may occur. Due to these effects and limitations of a PET detector, the location sensed by the detector is usually deviated from the travelling path of the annihilation photons.

To address these imperfections, resolution compensation is usually employed to recover the missing information. In this dissertation we focus on modeling and incorporating these degradation factors into the reconstruction procedure to improve the image quality. This work is usually performed through a system model, which in general includes all known factors related to a patient scan: 1) the geometry of the scanner, 2) the crystal configuration, 3) the energy resolution and time resolution, and 4) physical degradation factors, including the positron range, the

acolinearity of the annihilation photons, the crystal penetration, and inter-crystal scattering.

However, in practice , some assumptions are made in order to generate an accurate system model. For example, the acquisition configurations (acquisition parameters and patients) usually vary in clinical routines, which further complicate the system model. Constructing a system model for each acquisition configuration would be more accurate, but it is unfeasible. So we assumed that the system model is independent of acquisition configurations. In this way, coupling among different events can be eliminated by performing time-independent simulation. Patient-dependent factors have to be excluded from the system model for the same reason stated above.

Monte Carlo simulation is an ideal candidate to model all the aforementioned factors. Variance reduction techniques (VRTs) are necessary for speeding up simulations of for instance resolution modeling. With the assumptions mentioned in the previous section, we implement several simple VRTs to further improve the simulation efficiency of egs_pet. The first technique is polar angle biasing, which is employed to reduce the cost in simulating photons that are not flying toward the detector. An alternative way is to perform hit-testing on whether a photon can hit the detector or not, but this testing could be expensive. Positron tracking can be further optimized by reusing a positron history for multiple annihilation photon pairs. For photon tracking in the detector, fictitious transport in crystal arrays is used to save the cost in bound cross handling, and forced energy window passing improves simulation efficiency by analytically calculating the survive probability through the energy window. Finally, the transport parameters can be optimized for better efficiency without loss of accuracy.

The optimized Monte Carlo simulator provides a solid basis for Monte Carlo-based resolution modeling, which is the central part of this dissertation. In addition to the aforementioned Monte Carlo simulator, we proposed a novel rotator-based algorithm for the resolution modeling problem in PET. With a rotator, the rotational symmetries in a cylindrical PET scanner can be employed for any basis functions in resolution compensation. This simple operation improves the resolution modeling simulation efficiency by an order of magnitude. This approach also reduces the redundancy in a system model, which makes the system model compact enough for a personal computer. With our fast Monte Carlo simulator and symmetry handling techniques, an accurate system model can be obtained within a week on a small computational platform.

In addition to Monte Carlo-based resolution modeling, we also discuss the experiment-based point spread function (PSF) modeling with the rotator-based algorithm. Our method directly parameterizes the profiles of PSFs. We add key components progressively and evaluate their impact on the quality of the reconstructed image separately. An initial system model is presented in this work. Radial blurring and axial blurring are modeled and their effects on the image quality are evaluated. Axial blurring has been demonstrated as a minor factor in resolution compensation. However, axial blurring improves contrast recovery for small hot lesions, which makes it an interesting factor in resolution modeling.

Although a rotator makes the rotational symmetries open to a Cartesian discretization, pronounced ringing artifacts are detected in the reconstructed image due to the extra (artificial) blur introduced. We characterize the ringing artifacts occurring in our rotator-based reconstruction by applying an accurate system model into the ideal rotator-based algorithm. The ideal rotator uses polar-pixels as the basis functions, which is rotationally symmetric. This feature is used to implement an ideal rotator, which does not alter the detector response because no blurring is introduced during image rotation. Thus, the ringing artifacts in the ideal rotator-based approach belong to the well-known Gibbs effects because the ideal rotator provides a matched system model to the data. This fact is used to investigate the origin of the ringing artifacts in the rotator-based approach. We also investigate the relationship between ringing artifacts and contrast recovery for small hot lesions. This work suggests that the ringing artifacts are mainly attributed to the blurring rotator. Our study also indicates that the ringing artifacts artificially improve the contrast recovery of hot lesions particularly small hot lesions.

The ringing artifacts cause bias in the image at sharp transitions of image intensities. The artifacts are visually more pronounced in noiseless data. In practice, the ringing artifacts become invisible because noise artifacts in emission tomography are more pronounced. However, the bias remains in image sharp transitions and pushes the contrast toward the true value, particularly for small lesions. The improved contrast may improve the detection of small lesions, which is very important in oncology applications.

Monte Carlo-Based Reconstruction for PET

Chapter 1

Introduction

1 Background

Inspection is one of the most important medical diagnosis techniques. Over 2200 years ago, medical practioners in ancient China summarized a systematic non-invasive diagnosis technique, including Inspection, Listening and smelling examination, Inquiry and Palpation. Some components of this technique remain important components in modern medical practice, such as inspection and inquiry. Dissection is another category of diagnosis method, the invasive inspection technique. The emergence of modern medical imaging techniques, especially Ultrasound tomography (US), Computed Tomography (CT) and Magnetic Resonance Imaging (MRI) modalities, have brought revolutionary transformations in medical diagnosis by providing cross-sectional images without physical injury in the subject. Diseases are usually determined with regards to morphological changes. This milestone transformation is usually referred to as bringing "the invisible into the light" [Wernick and Aarsvold, 2004].

Another breakthrough lies in the raising of functional imaging techniques, namely single photon emission computed tomography (SPECT) and especially positron emission tomography (PET). It is well known that abnormal functions precede changes in anatomical structures [1]. In addition, abnormal functions could be temporal if treated in time, while morphological alterations are usually permanent and might not be restored even after normal function has been restored. Functional imaging modalities show their strongholds in detecting functional disorders with great sensitivity. For this reason, these modalities have been applied in molecular biology for inspecting cellular function and tracking the molecular processes of living organisms *in vivo*. This intersection forms the new discipline molecular imaging.

[1] Trauma is an exception

PET imaging is a branch of nuclear medicine imaging. It is a relatively new and rapidly evolving imaging modality in nuclear medicine imaging. This imaging modality uses the same tracer principle as the other nuclear medicine modalities (SPECT, planar imaging, etc.). As its name implies, PET uses the radiation formed by positron-electron annihilation, which is two back-to-back (180° apart) annihilation photons. PET image acquisition begins with administration of a positron emission radiopharmaceutical in the patient. The molecules of the radiotracer are involved in physiological processes and are distributed within the body. The distribution of the radiopharmaceutical, in turn, reveals information about the physiological processes. A PET scanner records the spatial information of all detected photons, organized into a special histogram called a sinogram. Sinograms containing the spatial information of detected annihilation photons can be inverted into the distribution of the radiotracer by a process called reconstruction.

Many reconstruction methods have been proposed. These methods can be subdivided into two major categories: analytical algorithms and iterative algorithms. Analytical algorithms find the radiotracer distribution by computing the analytical solution directly, representative algorithms are filtered backprojection (FBP) and backprojection filtration (BPF). Iterative algorithms search the radiotracer distribution through an iterative procedure. There are two types of iterative algorithms, algebraic algorithms and statistical iterative reconstruction (SIR) algorithms. Algebraic algorithms mainly refer to the Algebraic Reconstruction Technique (ART) and its variants. Typical SIR algorithms are the most popular reconstruction methods in PET imaging. Typical algorithms are maximum likelihood expectation maximization (ML-EM), ordered subset expectation maximization (OS-EM) and maximum *a posteriori* (MAP).

This PhD dissertation mainly focuses on statistical iterative reconstruction techniques (SIRT) with Monte-Carlo modeling or experimental modeling of the image formation process. Incorporation of a realistic model in the iterative reconstruction algorithm improves the image quality significantly. However, Monte Carlo simulations are very time-consuming, especially for state-of-the-art whole-body PET scanners. Even a reasonable Monte Carlo-based system model requires highly efficient simulation techniques and exploiting inherent symmetries of the scanner system. Proper choice of the basis function of image representation plays an important role in symmetry handling techniques. Thus, we investigate two different categories of techniques to solve the computational problem in Monte Carlo-based resolution modeling for whole-body PET scanners. These techniques are efficiency improvement techniques in Monte Carlo simulation and image representation techniques using different basis functions. Experimental modeling is also very time-consuming. A parameterization technique is used to reduce the measurement time and downsize the system model.

2 Organization of this dissertation

In chapter 2, a brief overview of PET imaging physics and scanner modeling, including image formation and, key components of reconstruction algorithms, is given. Preliminary knowledge of the physics relevant for PET imaging and the instrumentation of PET scanners are briefly described. Image quality degeneration factors are then summarized based on the physics and instrumentation knowledge. The first major component contains reconstruction algorithms, preceded by Monte Carlo- and experiment-based scanner modeling techniques, the other major component of this dissertation. This chapter ends with a discussion of open problems in both reconstruction algorithms and system modeling techniques.

In chapter 3, the general methodology of SM simulation is described. This methodology was implemented in egs_pet, a light-weight EGSnrc-based Monte Carlo C package. These variance reduction techniques (VRTs) are polar angle biasing, hit-testing, positron history reuse, forced energy window passing, fictitious transport in crystal arrays and optimal transport parameters. The VRTs are then validated using voxel sources located at the center of the field of view (FOV) and at the edge of the FOV. The simulation efficiency is improved by a factor of about 15 times without any degradation in image quality.

In chapter 4, a Monte Carlo-based resolution modeling technique using voxels as the basis functions is described. This method tries to utilize the inherent symmetry of the PET scanner by rotating the image volume. Rotation of image grids makes the voxel discretization rotationally symmetric. Hence, the rotator-based method is able to utilize inherent rotational symmetry while retaining voxel discretization. This characteristic reduces the cost of SM simulation and saves the storage requirement for storing the SM in main memory. The image quality was considerably improved. However, ringing artifacts were found. The origin and effects of the ringing artifacts will be discussed in the chapter 6.

In chapter 5, experimental system response modeling is investigated. The system responses were acquired with a scanning point source using a staging robot. The obtained point spread functions were then fitted according to an asymmetric Gaussian model. The parameterized point spread functions were applied in the rotator-based algorithm with considerably improved image quality. We also used the factorized matrix technique to further reduce the storage requirement of the system model.

In chapter 6, the ringing artifacts of the rotator-based method were characterized quantitatively when it was used with an accurate system model. Because the blur of the rotator may alter the system responses, i.e., increase the kurtosis of the point spread function, the study also reveals the effects of exploiting an over-blurred system response kernel in reconstruction. We also proposed an ideal rotator to serve as the baseline. The rotator was chosen to be the Gaussian rotator

as its blur is fixed and not angle-dependent. This characteristic of the chosen rotator enables a quantitative study as the extent of the blurring can be calculated. We also used the blurring of the rotator to compensate for positron range and acolinearity. However, the results indicate that the blurring of the rotator is wider than the blurring of these two physical factors when ML-EM or OS-EM is used.

Finally, in the last chapter, general conclusions are drawn. Possible points and directions that need further investigation are also briefly discussed and listed at the end of this chapter.

Chapter 2

Positron Emission Tomography

2.1 General Introduction

This dissertation lies in the exciting world of imaging science, which is a multi-disciplinary field concerned with the generation, collection, duplication, analysis, modification, and visualization of information [Hornak, 2002]. It is commonly assumed in psychology that vision is the most important channel of source of information to humans. Human beings rely on tools to convert invisible information into visible, interpretable, and understandable information. Telescopes help us to understand the universe. Similarly, medical imaging devices help people to not only "view" anatomical images for the diagnosis and treatment of the disease (what) but also investigate the functional mechanism of the human body at physiological, biochemistry, and molecular levels (how and why). Medical imaging techniques have became a very important component in modern clinical diagnosis and many routine procedures.

By definition, "medical imaging" refers to imaging techniques or processes that reveal the subject of interest, whether it be anatomical or functional for clinical purposes or for medical research. Many imaging modalities are employed in clinical and biological research. There are various criteria used in classifying these imaging modalities. Here, we use the properties of the information yielded by an imaging device to classify the modality into two general categories. The first category is the non-functional imaging techniques, which includes well-known computed tomography (CT), ultrasound (US) imaging, magnetic resonance imaging (MRI) and X-ray radiography. Non-functional imaging techniques usually depict the anatomical structure of the human body. A disorder is usually diagnosed by looking for a visible change in anatomical structures. The other class

is functional imaging, which includes most nuclear medicine imaging techniques, namely positron emission tomography (PET), single photon emission tomography (SPECT), scintigraphy (planar imaging), and other modalities, such as fluoresce imaging (FI) and optical imaging techniques. These imaging modalities produce images from which information can be derived about metabolic processes. Nonetheless, recent advances in medical imaging have enabled some traditionally non-functional imaging modalities to provide functional information as well. Typical examples of those imaging modalities are functional MRI (fMRI) and Doppler ultrasound. An fMRI image provides information about oxygen consumption and yields information related to the metabolism of oxygen. Doppler US is able to detect the velocity of blood flow in the vessels; thus it provides functional information about organs, e.g., the heart.

This work will focus on Positron Emission Tomography (PET), which is a functional imaging modality frequently used in clinical practice. A brief description of the principle, the basic physics, instrumentation, reconstruction techniques and Monte Carlo simulation of PET are presented. This introduction gives a brief overview of the basic knowledge that is required for the Monte Carlo-based resolution modeling in PET.

2.2 The Principle of PET

PET is a nuclear medicine (NM) imaging technique. It uses a positron-emitting isotope as a radiotracer to investigate functional information by employing the radiotracer principle. The radiotracers used in a PET scan are usually produced on-site by a cyclotron, which is a device that can accelerate charged particles to energy high enough to produce nuclear reactions.

Molecules that are significant for diagnostic purposes are labeled by positron emitting atoms. The most commonly used radiotracer is F18-FDG, which behaves like a glucose molecule inside the human body. After being emitted, the positron annihilates with a nearby electron and two back-to-back annihilation photons are produced. The back-to-back feature of the annihilation photons enables PET to work without employing collimators. This difference is the reason why a PET scanner has higher sensitivity than a SPECT scanner. The detection of such a photon pair, a special technique called coincidence detection is needed, which determines a valid pair of annihilation photons by examining the time of detection and accepts two detections that are close enough as a valid coincidence. Once a valid coincidence is determined, the origin of the two photons is known to approximately belong to a line of response (LOR). Given millions of such coincidences, the radioactive distribution can be estimated using tomographic image reconstruction. This process is illustrated in Fig. 2.1.

More details on physics, instrumentation and image reconstruction on PET can

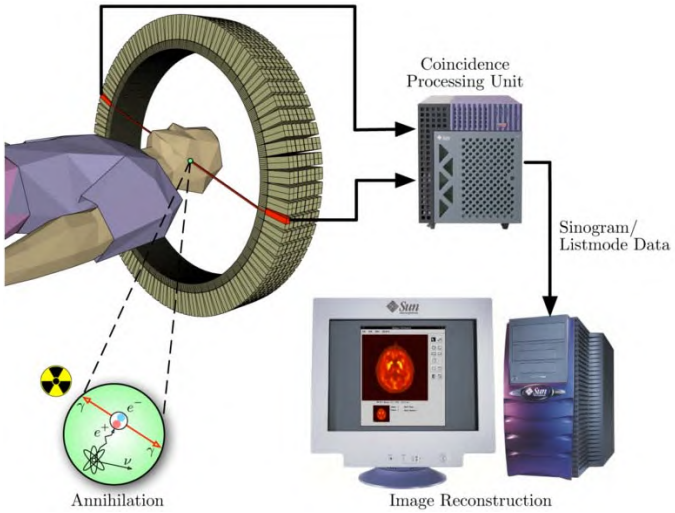

Figure 2.1: Illustration of the work flow in a real world PET examination.

be found in the following sections.

2.3 Nuclear medicine imaging physics

2.3.1 Common radiation forms in nuclear medicine

Radiation refers to the process of energy transfer in media or in space, in the form of wave or particle. For example, the sunshine broadcasts heat from the sun to the earth. The broadcasting of radiation can be utilized to transfer information, such as a wireless network or a radio. When travels in media, the energy of the radiation may be absorbed or reflected back by the media. By analyzing the remaining or the scattered radiation, information about the structure of an object can be investigated. This principle forms the basis of most imaging modalities found in a modern hospital.

In a radiology department, most imaging modalities, such as Nuclear medicine imaging and CT use *ionizing radiation*, which transfers large amount of energy and is capable of ionizing atoms. This radiation used in a nuclear medicine imaging modality or a CT is usually composed of high-energy photons. Non-ionizing electromagnetic radiation does not cause ionization of atoms. A typical example of non-ionizing radiation is the radio frequency (RF) radiation, which is used in MRI and fMRI to excite hydrogen protons in water molecules. Generally, particle radiation is not directly employed in nuclear medicine imaging techniques to due to their poor penetration capabilities. Some common ionizing radiation employed

in different imaging modalities will be briefly introduced here.

β^+ radiation The β^+ radiation consists of energetic positrons. The positron is the antiparticle of the electron. It occurs during the conversion of a proton into a neutron. This process can be expressed as:

$$ {}^{1}_{1}p^{+} \rightarrow {}^{1}_{0}\, n + {}^{0}_{1}\, \beta^{+} + \nu \tag{2.1} $$

A second particle is emitted, which is a neutrino. Similar to that of the electron, the energy spectrum of positron emission is also continuous. After positron decay, an electron is also ejected from the daughter nuclei to balance charge, which is often through an internal conversion. Positron emission nuclei may also decay by electron capture. The most commonly used isotope for PET imaging, 18-fluoride, has a positron emission branching ratio of 97% and electron capture branching ratio of 3%.

Annihilation radiation Annihilation radiation forms the basis of PET. Most annihilation of a positron and an electron occurs at rest. The combination of these two particles forms a metastable intermediate species called positronium, which exists for around 10^{-7} seconds (mean life) and then annihilates into two photons that have an energy of approximately 511 keV and traveling apart in opposite direction. At the time of annihilation, both the positron and the electron have residual momentum, which leads to the acolinearity of the two annihilation photons. The cross section of positron at rest is infinite, so all positrons will eventually annihilate with electrons. The positronium may annihilate into three or more photons. There are in flight annihilations. For in flight annihilation, the polar angle of the annihilation can be uniquely determined by the energy of the positron. The branch ratio is about $\frac{1}{k}$, where $k \approx 137$ is the fine structure constant.

γ radiation Gamma rays are another important form of electromagnetic radiation. Unlike X-rays, gamma rays are mainly involved in nucleus reactions such as spontaneous nuclear decay. Thus, gamma radiation could be accompanied by a decay schema. Despite different origins, X- and γ-rays are essentially the same substances (high energy photons). Gamma ray emission is also characteristic and its energy is determined by the difference in energy levels between the initial and final state of the nucleus.

X-ray radiation X rays are electromagnetic radiation produced when orbital electrons drop down to fill vacancies in the atom after an inner shell electron is displaced. Thus, X-ray radiation is naturally characteristic because the energy of the X ray is the difference in the quantized binding energies between the shells. Different atom species emit different characteristic X-rays.

However, an X-ray tube produces a continuous energy spectrum with several peaks in the physical world, which indicates that other sources of X-ray radiation exist. This radiation is called bremsstrahlung (German: "breaking"). Bremsstrahlung radiation is caused by the deceleration of an electron in the electromagnetic field of the nucleus. X-ray radiation is of special significance in the history of medical imaging because the first radiology image was made using X-rays.

Some other forms of radiation employed in therapeutic application also involve some nuclear medicine imaging techniques, for instance, the α radiation and the β^- radiation.

α radiation Alpha radiation involves with alpha particles, which are actually nuclei of helium ($^4_2He^{2+}$). Due to their large mass and electric charge, alpha particles are very likely to interact with surrounding materials and loss their energy over a short distance.

High energy alpha particles are frequently employed for therapeutic purposes. During the treatment, some positron emitting nuclei (predominantly ^{11}C and ^{15}O) may be created, which can be employed to perform PET imaging [Enghardt et al., 2004] [Parodi et al., 2005].

β^- radiation In β^- radiation, the energy is conveyed by electrons. It occurs in a β^- decay, where β^- particles are emitted from the nucleus, together with an anti-neutrino. The energy spectrum of the β^- particles is continuous with a maximum. Noting this phenomenon, Wolfgang Pauli discovered a new particle, which was the antineutrino.

β^- emitting isotopes are frequently employed in therapeutic applications. The bremsstrahlung emission can be imaged by a gamma camera to evaluate the dose distribution in treatment employing β^- emitting isotopes [Kallergi et al., 1992] [Balachandran et al., 1985] [Rault et al., 2008]

2.3.2 Interaction of β particles with matter

The emitted β particles have an initial energy whose value is in a continuous range from zero to a maximum. The β particle loses kinetic energy through interactions with the surrounding matter. For a positron, the distance from its original location to the point of annihilation is called the positron range, which ranges from 0.5mm to 8 mm for common isotopes used in PET imaging [Cherry et al., 2003]. This physical effect is one of the fundamental limitations of the spatial resolution of PET. For electrons, the range is of importance for dose localization during radioisotope therapy.

A β particle loses its kinetic energy by four types of interactions to its surroundings:

- Inelastic collisions with atomic electrons. The behavior of e^+ and e^- is different when interacting with atomic electrons. The e^-e^- interaction is described by Möller scattering, while e^-e^+ interaction is by Bhabha scattering. In this process, the β is deflected and energy is transferred to the electrons, which may cause ionization of the atom. This interaction is the most important mechanism of kinetic energy loss;

- Elastic collisions with atomic electrons. In this process, the β is deflected but energy and momentum are conserved;

- Inelastic scattering with a nucleus. This process can almost be ignored. The positron is deflected. Bremsstrahlung radiation can often be found in this process.

- Elastic scattering with a nucleus. The β is deflected with conserved energy and momentum (similar to elastic collisions with atomic electrons).

The β particle loses energy in inelastic interactions with surrounding matter, but it is deflected by both elastic and inelastic interactions. Thus, the path the β particle takes in traveling through matter is extremely tortuous. These characteristics of β particle-matter interactions pose major challenges in Monte Carlo simulations of positron/electron transport.

2.3.3 Interaction of Photons with Matter

Photon-matter interactions are very different from positron-matter interactions. Photons can pass through materials without a single interaction or with only a few interactions. For the same incident energy, photons are more difficult to stop than particles in the same material. Photon-matter interactions for the photon energy within the range of interest for medical imaging applications can be classified into four types: Rayleigh scattering, the photoelectric effect, the Compton Effect, and pair production. In addition, other mechanisms, such as triplet production and photonuclear reactions exist, but they usually involve energy more than 10 MeV. Thus, we only discuss the Rayleigh scattering, photoelectric effect, Compton effect and pair production.

2.3.3.1 Rayleigh scattering

Rayleigh scattering, also called coherent scattering, is an interaction between a photon and a whole atom. This effect predominates at energies less than 50 keV. This energy is of interest for low-energy CT or dual-energy CT imaging.

2.3.3.2 Photoelectric Effect

The photoelectric effect (PE) involves the incident photon with an inner shell electron of an atom. The energy of the incident photon is transferred completely to the electron, which is ejected from the atom. The removal of an inner electron ionizes the atom. The excited atom returns to the ground state by emitting a characteristic X-ray or by ejecting another electron, which is called an Auger electron. The PE holds a very important place in the development of modern physics. From his observations of this phenomenon, Einstein proposed the quantized theory of electromagnetic radiation, which won him the Nobel Prize in 1905.

PE is the dominant effect for photons with energy less than 100 keV. This characteristic is crucial for radiological imaging and CT imaging where the attenuation of photons is the source of the image contrast.

2.3.3.3 Compton (incoherent) scattering

Compton scattering involves interactions between photons and loosely bound outer shell electrons of an atom. It is also called incoherent scattering. These electrons can be regarded as unbound and the binding energy can be neglected in calculating the defection angle of the photon. After a Compton scattering, the incident photon is deflected in a new direction and the wavelength of the photon is shifted towards longer wavelengths. The major portion of this energy loss has been transferred to the ejected electron. The atom remains in excited state. The transition of the atom from the exited state to the ground state is generally negligible due to the small binding energy. Thus, the electron ejected due to the Compton Effect has an initial kinetic energy equal to the energy loss of the photon. The deflected angle is correlated with the energy loss of the photon, which can be expressed as:

$$E_{\gamma}^{'} = \frac{E_{\gamma}}{1 + \frac{E_{\gamma}}{m_0 c^2}(1 - cos(\theta))} \tag{2.2}$$

Where $m_0 c^2$ is the total rest mass energy of an electron. For PET, this equation can be simplified as:

$$E_{\gamma}^{'} = \frac{E_{\gamma}}{2 - cos(\theta)} \tag{2.3}$$

Compton scattering is of prime importance to radiobiology, as it happens to be the most probable interaction for the gamma rays and high-energy X-rays used in radiotherapy. Studies have shown that about 80% of the photons undergo Compton scattering only once in human tissue [Ollinger, 1996].

2.3.3.4 Pair production

Pair production refers to the creation of an elementary particle and its antiparticle. These particles are usually produced from a photon or another photon-like parti-

cle (a neutral boson). Due to energy conservation, this process can only happen when the photon has energy equal to the total rest mass energy of the two particles. This minimum energy is 1.022 MeV to produce an electron-positron pair production. This energy is usually beyond the energy of interest for photons in nuclear medicine imaging.

2.4 PET Instrumentation

2.4.1 Geometry

PET scanners need at least two detector heads to collect coincidences formed by back-to-back annihilation photon pairs. The two heads usually rotate to measure projections at different angle to perform tomography imaging. This is different from SPECT, where the data can be collected by a single rotating detector head. To improve the sensitivity, more detector heads and longer axial extensions are used. The most popular geometry setup for PET is the cylindrical scanners arrangement. Fig. 2.2 displays some of the geometry setups that are used in PET scanners.

A scanner with proper geometry may offer better scanner performance. A spherical geometry like Siemens Biograph (Hi-Rez) may offer better sensitivity, but causes difficulties in image reconstruction with resolution compensation [Panin et al., 2006c]. A tapered crystal may not only improve the sensitivity but also provides rotational symmetries and image reconstruction may benefit from this design [James et al., 2010] [Yang et al., 2011]. The spatial resolution of PET can be improved by a virtual pinhole PET geometry [Tai et al., 2008]. Recently, researchers evaluated stationary two-head scanner geometry for low cost preclinical PET imaging with large detector blocks compared to the subject [Zhang et al., 2010a].

2.4.2 Physics

2.4.2.1 Object Photon Attenuation

The end product of annihilation is mostly two back-to-back photons, each with energy of approximately 511 keV. These photons may interact with the surrounding human tissue through processes, such as Compton scattering, photon electric absorption or Rayleigh scattering. Thus, not all photons survive the journey to the detector.

The effect that the number of photons goes down after traveling through certain materials is called photon attenuation. This effect can be described by a monotonic exponential function [1]:

[1] Only for well-collimated narrow beams

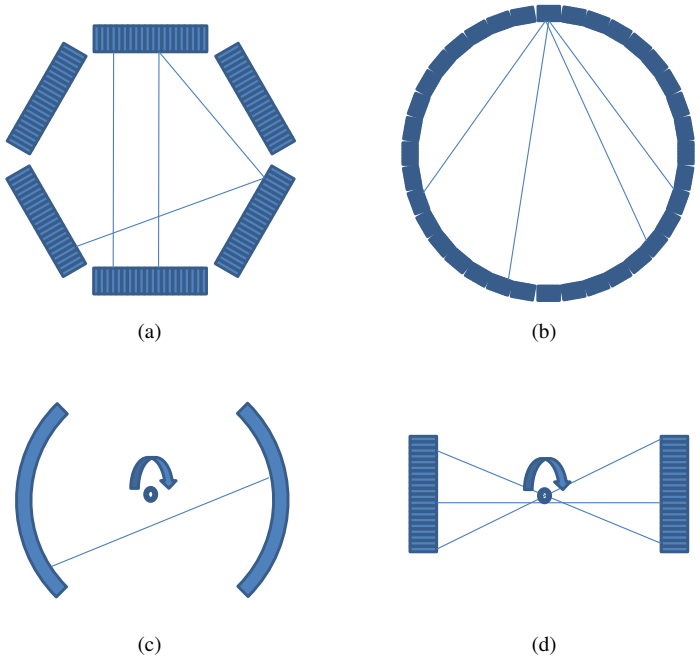

Figure 2.2: Typical geometric setups in PET scanners. (a) Flat panel detectors with large detector blocks. This configuration has better sensitivity and more regular in-plane sampling. (b) Cylindrical PET scanner with small detector blocks. This configuration optimizes the system sensitivity and is the most popular geometry for commercial PET scanners. (c) PET scanners using monolithic curvature detector. This configuration optimizes the system sensitivity and event localization. (d) Two rotating-head-detector. This configuration is the most economic setup that meets the minimal requirements for PET imaging.

$$I_d = I_0 e^{-\mu d} \tag{2.4}$$

where I_d is the intensity of a photon beam after travel through a material with thickness d, I_0 is the initial intensity of the beam and μ is the linear attenuation coefficient, describing the attenuation as a function of the distance traveled in a material. The photon attenuation effect depends on the energy of the incident photon and the characteristics of the material, mainly the electron density. Thus, a crystal made from high-Z material is preferred in nuclear medicine imaging for photon detection [Cherry et al., 2003].

2.4.2.2 Physics in the scintillation detector

X- and low energy gamma photons are the best candidates in medical imaging due to their properties, e.g., they travel along a straight line (one reason electrons cannot be used); they have stronger penetrating ability in human body (one reason α particles are not used); and most important of all, they can be easily stopped with heavy metal collimators and examined with scintillation detectors (the main reason neutrinos cannot be used).

Scintillation detectors are made of luminescent crystals. The atoms of such crystals often emit scintillation photons when transiting from an excited state to the ground state. Sometimes, no scintillation photons may be emitted during the state transition; this process is called quenching.

As discussed in section 2.3.1 and 2.3.3, there are three major photon-matter interactions in the energy range of interest for medical imaging. After a Compton scattering, the incident photon is deflected and a certain amount of its energy is transferred to a loosely bound electron. This energy is partially used by the electron to overcome the binding energy, and the remaining energy becomes the initial kinetic energy of the electron. The electron interacts with surrounding materials mainly by inelastic scattering with other electrons, resulting in a large number of excited atoms. These atoms return to the ground state by either a luminescence or quenching process. The situation is similar when an incident photon undergoes PE absorption: one (PE) or two electrons (internal conversion) are ejected from the atom. These electrons induce quenching or luminescence in the crystal. As there is no energy transfer in Rayleigh scattering, no scintillation photons are produced.

Crucial properties of a scintillator for imaging applications are stopping power, signal decay time, light output and energy resolution [Melcher, 2000]. The stopping power is measured by the attenuation length (mean distance) that a photon travels in the crystal before being absorbed. The stopping power is determined by density of electrons of the material or the density ρ and the effective Z_{eff}. The signal decay time is mainly attributed to the decay constant of the crystal. A fast decay constant usually leads to a faster signal and better time resolution of the

Property	NaI (TI)	BGO	LSO	LYSO	GSO	BaF_2
Density (g/cm^3)	3.67	7.13	7.4	4.53	6.71	4.89
Effective Z	50.6	74.2	65.5	34.2	58.6	52.2
Attenuation length	2.88	1.05	1.16,	2.58	1.43	2.2
Decay constant (ns)	230	300	40	70	60	0.6
Light output (photons/keV)	38	6	29	46	10	2
Energy resolution (%)	6.6	10.2	10	12.5	8.5	11.4

Table 2.1: Physical properties of scintillators commonly used in PET (the attenuation length and energy resolution are measured at 511 keV

scanner, which is key in time of flight (ToF) PET imaging [Lecoq et al., 2010]. The energy resolution is correlated to light output. Generally, a high light-output helps to attain better energy resolution when other conditions stay the same. High light output also improves the time resolution [Conti et al., 2009] [Schaart et al., 2010] [Lecoq et al., 2010]. In addition, a bright crystal enables finer pixelization of the crystals, which helps to achieve better spatial resolution. Commonly used scintillators in PET imaging are listed in Table 2.1 (the attenuation length and energy resolution were measured at 511 keV).

2.4.3 Detectors

2.4.3.1 PMT

The luminescence photons are collected by photon detectors and converted into electrical signals. Generally, photon detectors can be divided into two types: photon-multiplier tubes (PMTs) and semiconductor detectors. The PMT is very fast and has a very high gain (on the order of 10^6). The high gain is attributed to the high signal-to-noise ratio (SNR) of the PMT [Cherry et al., 1995].

Fig. 2.3 displays a schematic drawing of a PMT. The cathode, anode and dynode stages are encapsulated in a vacuum tube, and high voltage is applied to each dynode stage. The PMT actually multiplies photoelectrons. Luminescence photons entering the PMT first displace a photoelectron, which is then electronically focused onto the first-stage dynode. These photoelectrons are accelerated from one dynode to the next, displacing more electrons and the signal is amplified stage by stage. Usually, a PMT contains ten to twelve accelerating stages, causing large amplification by the end-stage dynode. These electrons are then collected and further amplified by the pre-amplifier.

Alternative photon detectors to PMTs are semiconductor detectors such as avalanche photo diodes (APDs). The advantage of semiconductor detectors lays in their compact package sizes. It is possible to couple a single crystal to a single APD in contrast to a PMT of 2 to 3 inches, which is too big for nowadays

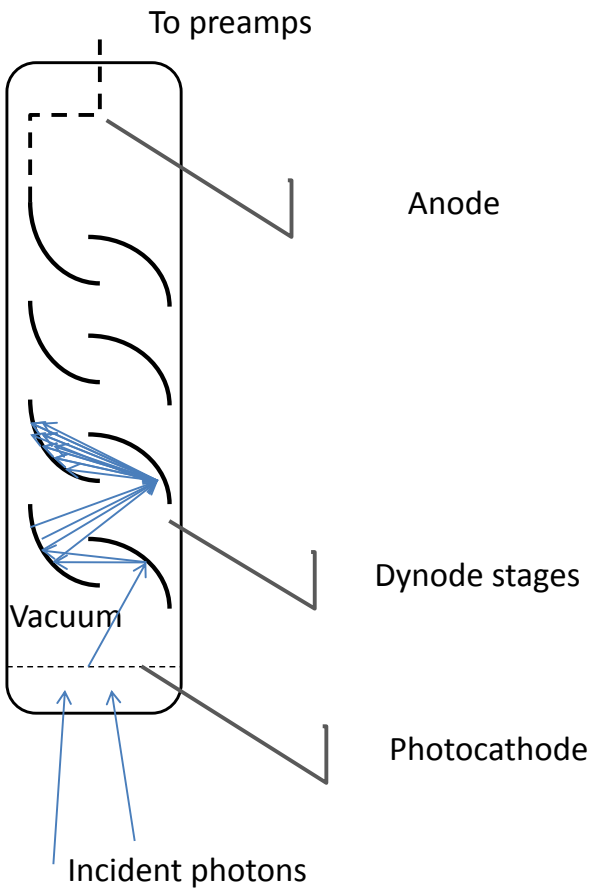

Figure 2.3: Schematic diagram of a photomultiplier tube.

crystal dimensions (4 mm $\approx$ 6 mm). However, APDs suffer from poor performance in practice due to their low gains and unstable performances [Moehrs et al., 2006] [Otte et al., 2006]. Geiger mode APDs or silicon PMs (SiPMs) do not have such constraints and are a promising alternative to PMTs, particularly for hybrid PET-MR imaging [Schaart et al., 2009] and ToF PET imaging [Schaart et al., 2010].

2.4.3.2 Block detectors design

Accurate positioning can be determined by one-to-one coupling between a crystal and photo detector pixel with position sensitive PMTs (PS-PMTs), SiPMs or APDs. However, by employing a clever design, the use of low-price PMTs yields reasonable results. This is done in the so called Anger camera, which was developed by Hal Anger in 1957 and is still widely used today [Cherry et al., 2003]. This design uses sets of PMTs arranged (usually, in hexagonal configurations) behind a slab of monolithic or pixelated crystal. The location of an incident photon can be estimated by using equation 2.5. Most human PET scanners use the centroid of the output of each PMT as the detection position. The centroid is equivalent to a linear least square estimate [Gray and Macovski, 1976]. For pixelized detectors, the crystal identification can be performed by using a 2D looking up table, or the crystal position map, as illustrated in Fig. 2.4b. The crystal position map can be determined by numerical analysis of a flood histogram [Wernick and Aarsvold, 2004]. Interested readers are encouraged to read literature [Chaudhari et al., 2008] for a comprehensive review.

Fig. 2.4 illustrates the structure of a block detector employing the same idea as the original Anger detector design. The total energy is the sum of the signals from the four PMTs. The position is determined by the light ratio collected by these PMTs:

$$p_x = \frac{(A+B)-(C+D)}{A+B+C+D} \tag{2.5}$$

$$p_y = \frac{(A+C)-(B+D)}{A+B+C+D} \tag{2.6}$$

For small animal systems, advanced techniques employ different statistical approaches to estimate the interaction positions of detectors with a monolithic crystal slab have been proposed [Gray and Macovski, 1976] [Joung et al., 2001] [Vinke et al., 2010]. These approaches involve a comprehensive calibration scan to determine the light response functions (LRFs), which links the PMT outputs and the spatial information of a photon beam. The most likely interaction positions are determined by matching the PMT outputs of a single event and those LRFs. The total sum of the voltages from each photomultiplier is proportional to the deposited energy of the incident photon.

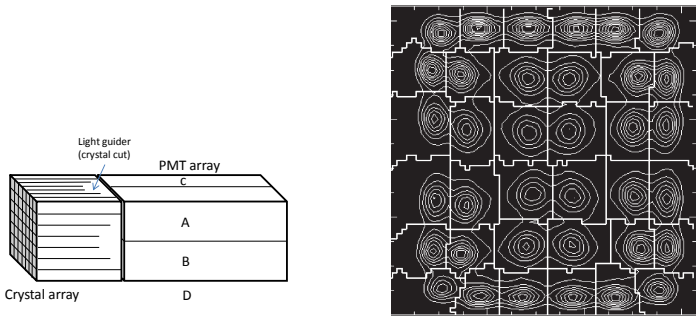

(a) (b)

Figure 2.4: 2.4a A schematic illustration of the concept of a block detector, also called Anger logic or the Anger camera. The energy is the sum of signals of the four PMTs. The position of the event can be determined by the light share among illuminated PMTs or (b) positioning by numerical analysis. A 2D block map of a 6x6 BGO crystal array viewed by four PMTs. The relative light output is indicated by the isocount curves. The heavy white lines indicate which region is assigned to a crystal.

2.4.3.3 Energy resolution

The energy resolution of a radiation detector is the resolving power in radiation beams with different energies. The energy resolution of a scintillation detector depends on the relative light output of the scintillator, variations of the photons collected by the coupled PMTs, the fluctuation of amplification of readout electronics, and the intrinsic energy resolution of the scintillator [Cherry et al., 2003]. The intrinsic energy resolution is determined by the physical properties of the scintillator and variations in light output [Bailey et al., 2003].

2.4.4 Coincidence logic

The detection of both photons of an annihilation event forms a valid detection that can be used for tomographic reconstruction. However, the detector cannot determine if the detected photons are from the same annihilation event. To overcome this problem, the arrival time is used to determine a valid detection, which occurs if the two photons are detected within a limited time span. This concept is called coincidence detection, and a valid detection is called a coincidence. The limited time span chosen is called the coincidence window. Fig. 2.5 illustrates this coincidence concept. For an annihilation event, the two annihilation photons are detected. A pulse is formed on each detector channel. This pulse may trigger a window signal on the coincidence channel. If a second pulse appears within the window signal, a coincidence is formed between the two pulses. Otherwise, both pulses are discarded.

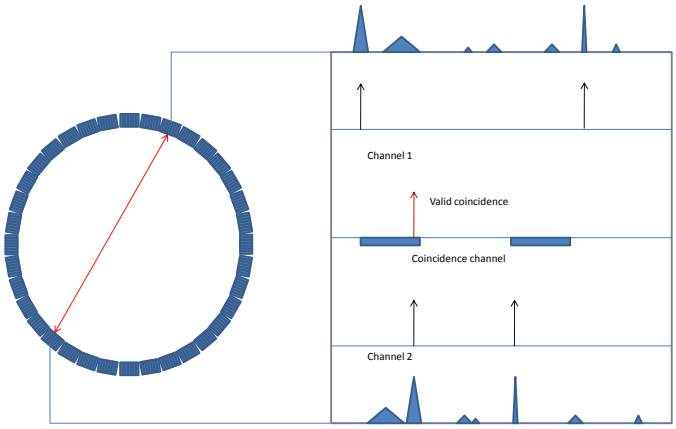

Figure 2.5: Illustration of coincidence detection. For an annihilation event, the two annihilation photons are detected. A pulse is formed on each detector channel. This pulse may trigger a window signal on the coincidence channel. If a second pulse appears within the window signal, a coincidence is formed between the two pulses.

To determine this time span, the time resolution of the detector and the time difference between the detection of the two photons has to be considered. The typical time resolution of a PET scanner ranges from 1 ns to 2 ns. The difference in detection times due to a different emitting location within the field of view (FOV) is about 3 ns (assuming that the scanner has a diameter of 1 meter). These two factors limit the minimum span of a coincidence window [Bailey et al., 2003].

2.4.4.1 Time of flight PET

Ideally, if the time resolution (the ability of the radiation detector to distinguish radiation with different arrival times) of the detector is high enough, the origin of the two back-to-back annihilation photons can be determined without reconstruction.

Even if the time resolution is not good enough to avoid reconstruction, the limited timing resolution of a PET detector can be used to estimate the annihilation point between the two detectors by looking at the difference in arrival times of the two photons. This extra information confines the origins of a detection event to a certain range on a LOR and improves the image quality. The improvement is inversely proportional to the time resolution and is related to the size of the object of interest. Generally speaking, if the range determined by ToF is smaller than the object size, improvement in image quality can be expected [Karp et al., 2008].

2.4.5 Image quality degradation factors

PET imaging is suboptimal. One reason for this deficiency lies in the poor counting statistics of the radionuclide imaging technique. This limitation is fundamentally due to the counting nature of nuclear events. Other limitations are due to various physical degradation factors, such as the positron range, acolinearity of annihilation photons, crystal penetration, inter-crystal scattering, photon attenuation, randoms and scatters. The positron range and acolinearity are inherent to PET imaging, while the other effects (crystal penetration, inter-crystal scattering, photon attenuation, randoms and scatters) could be reduced by improving the spatial, temporal and energy resolution of the detector. Details about the positron range and acolinearity can be found in section 2.3.2.

2.4.5.1 Crystal penetration

Crystal penetration refers to a phenomenon where a photon penetrates completely through a crystal and is detected by its neighboring crystal in a pixelized detector block, which results in a measured LOR that is different from the emission line. The LOR is defined as the straight line connecting the center of each detector in a detector pair, while the interaction site could be anywhere within the crystal pixel. The error caused by crystal penetration is also called the parallax error. This effect can be frequently found in a ring PET scanner composed of pixelized block detectors, and most notably for LORs at the edge of the FOV, as illustrated in Fig. 2.6. The axial parallax error may not be as pronounced as depicted in Fig. 2.6 because the length of the crystal is usually negligible compared to the radius of the scanner ring. This effect is geometric and can be modeled analytically [Rahmim et al., 2008] [Qi et al., 1998]. Employing depth-of-interaction (DOI) detector design may reduce the parallax error. In addition, the parallax error can be minimized by using 3-D detectors [Levin, 2008].

2.4.5.2 Intercrystal scattering

Intercrystal scattering refers to photon scattering among multiple crystals in a pixelized detector block. The Anger logic detector may not identify the crystal that contains the first interaction site. The centroid method may improve the localization accuracy of an Anger logic detector. Thus, registered line of response usually deviates from the emission line, which increases the positioning error. Fig. 2.7 displays the effects of inter-crystal scattering. Unlike the parallax error, the positioning error caused by inter-crystal scattering cannot be formulated and solved in a closed form due to the difficulties in describing the geometry of a scanner and the track of multiple scattering. This effect is usually estimated by Monte Carlo simulation and modeled in the system matrix to improve the image quality [Qi et al., 1998] [Rahmim et al., 2008].

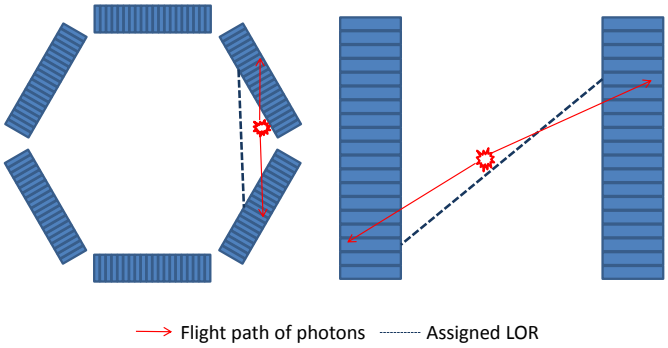

Figure 2.6: Crystal penetration causes the parallax error. This effect can be found in a ring PET scanner composed of pixelized block detectors and most notably for LORs at the edge of FOV. The axial parallax error is not as pronounced as depicted because the length of the crystal is usually negligible compared to the radius of the scanner ring.

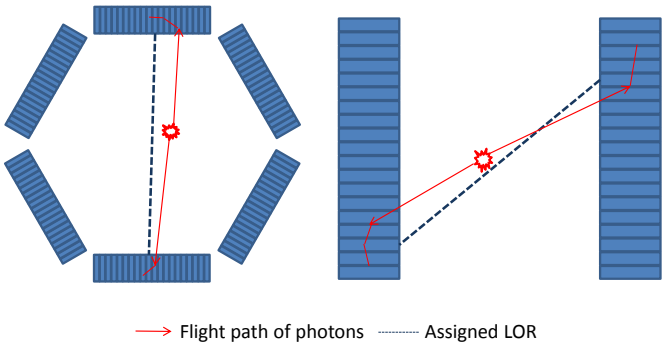

Figure 2.7: Illustration of the inter-crystal scattering. The positioning error is caused by the loss of information in photon detection. Unlike the parallax error, the positioning error caused by inter-crystal scattering cannot be formulated and solved in a closed form due to the difficulties in describing the geometry of a scanner. This effect is usually estimated by Monte Carlo simulation

2.4.5.3 Randoms

A PET scanner acquires three different kinds of coincident events: true, random, and scatter coincidences (Fig. 2.8). True coincidences arise from an emission from a single annihilation: both the annihilation photons are detected by the scanner without undergoing any directional changes on their paths. True coincidences convey the most accurate information about the origin position of an event despite the fact that they may suffer from crystal penetration and inter-crystal scattering as well.

Random coincidences, also named accidental coincidences, are coincidences composed of detections from different annihilation events. Randoms are a direct consequence of the coincidence detection principle of PET, and are especially present in PET scanners with poor timing resolution. Randoms arise when two photons from different annihilation events are detected by two well-separated detectors and are temporally close enough to be recorded within the coincidence timing window. The occurrence of randoms is illustrated in Fig. 2.8. Because the scanner cannot tag the photons with their annihilation origins, a false coincidence is produced. Randoms, as indicated by the nomenclature, are purely random. Random coincidences add uncorrelated background counts to an acquired PET image; hence they decrease image contrast if no corrections are applied to the acquired data.

The random coincidence rate in a PET scanner is proportional to $2\tau A^2$, where τ is the coincidence window and A is the activity present in the scanner field of view. However, the true coincident rate is linearly proportional to A. To reduce randoms, a narrow coincidence window is preferred. Hence, for PET imaging a fast scintillator with good timing resolution is desirable to reduce the number of random coincidences. However, the coincidence time window cannot be reduced to less than 3 ns (for a 1 m diameter ring scanner). Consequently, a PET scanner needs an optimized operational activity level with tolerable random coincidences and enough true coincidences for good imaging.

The random coincidence rate can be estimated during data collection. The randoms can be estimated by a delayed window method. All detected events are organized into a histogram as a function of the time difference between the two detector signals. The peak contains all prompt coincidences and randoms. The delayed window, located on the tails far away from the peak, contains only randoms. Techniques to improve the statistical properties are needed due to the limited count of randoms collected in a scan.

2.4.5.4 Scatters

Scattered coincidences are coincidences that arise from the same annihilation event but in which one or both of the annihilation photons undergo one or multiple scat-

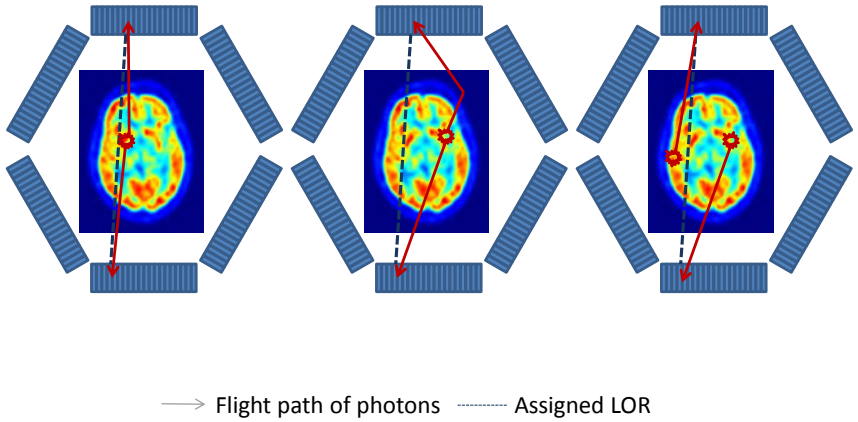

Figure 2.8: Types of coincidneces: trues (left), scatters (middle) and randoms (right).

tering interactions within the object. Photons that undergo scattering in the object lose part of their energy and they can be selected out by applying an energy threshold. However, photon detectors usually have a limited energy resolution to distinguish the scattered photons from the unscattered ones. Therefore, a significant fraction of the prompts are scatters.

A PET scanner needs good energy resolution to reject scatters. This ability is especially important in 3D volume imaging mode where high scatter fractions are present. A good energy resolution allows the application of a very narrow energy window, which results in more extensive and accurate rejection of scatter coincidences. The energy window-based technique may fail for certain scattered events because these events have the same energy as the true coincidences within the photo peak. Estimates from literature show that for whole-body imaging, up to 50% of the total detected coincidences are scattered coincidences and most (80%) of them are single scatter events [Ollinger, 1996] [Watson et al., 1997].

Scattered coincidences lead to wrongly positioned LORs, as illustrated in Fig. 2.8. Unlike random coincidences, the distribution of scattered coincidences is correlated with the distribution of the activity within the object. This effect leads to an incorrect activity distribution within the FOV. The overall effect reduces the image contrast.

Additional scatter-correction techniques are required to estimate the distribution of scattered radiation and remove scatters from the data to improve image contrast. As previously mentioned, about 80% of the total detections undergo only one scatter interaction in whole-body PET imaging, single scatter simulation (SSS) techniques have been proposed and implemented to correct for scatters [Watson

et al., 1997]. The attenuation map of the imaged object and an initial estimate of the radiotracer distribution are required for the SSS algorithms.

2.4.5.5 Photon attenuation

As described in section 2.4.2.1, the annihilation photons may undergo Compton scatter, photoelectric and other interactions within an object and may be absorbed or scattered with reduced energy. Thus, some annihilation events cannot be sensed by the scanner. Because the length of intersection of a LOR-object system varies spatially, different parts of the object may have different attenuation factors. This effect causes object-dependent sensitivity variation in the FOV, which leads to wrong activity distribution estimation if not compensated for.

The acquired data can be corrected for attenuation by applying the attenuation correction factor (ACF), which is a diagonal matrix and can be estimated from an external measurement by a transmission scan [Meikle et al., 1993] [Karp et al., 1995] or a CT scan [Kinahan et al., 1998] [Kamel et al., 2003] [Pan et al., 2005]. Recent approaches derive the attenuation map through MR images [Kops et al., 2007] [Montandon and Zaidi, 2005] [Schreibmann et al., 2010] [Keereman et al., 2010] [Catana et al., 2010].

2.5 PET Reconstruction

As described above, the signals detected by the PET scanner can only determine a line in the FOV or a certain portion of a line (for ToF PET), where the annihilation has occurred. This line is usually called a line of response (LOR) or more accurately a tube of response (TOR) when the finite crystal dimensions are considered [Terstegge et al., 1996]. In a real PET scanner, all of the collected events are sorted into a histogram, organized according to view angles and ring combinations. This histogram can be converted into a common sinogram (a term borrowed from CT imaging) by interpolation to correct for the special geometry of a PET scanner. Reconstruction is the process of estimating the radiopharmaceutical distribution from a PET measurement or the sinogram data. Some prior information is available for this "puzzle", namely, the geometry of the scanner, the material of the crystal and the attenuation map. In addition, some assumptions based on common sense (frequently called "priors") might be used in the image reconstruction such as non-negativity and smoothness of the activity distribution.

Various reconstruction techniques have been proposed. In general, these algorithms can be divided into two classes: analytical algorithms and iterative algorithms. Widely used analytical algorithms are filtered backprojection (FBP) and backprojection filtration (BPF). These algorithms are based on an analytical solution of the imaging reconstruction problem using the Fourier slice theorem [Kak

and Slaney, 2001]. The image can be calculated in one step. The limitations for these algorithms are oversimplifications of the system model and a lack of compensation for the underlying noise model. Iterative algorithms, on the other hand, estimate the image in an iterative way. Iterative algorithms can be further subdivided into two subclasses: algebraic reconstruction techniques (ART) [Gordon et al., 1970] and statistical iterative reconstruction algorithms (SIR). The ART algorithms treat the image reconstruction as an algebraic equation system. The image reconstruction reduces to finding the solution of a system of equations. Typical ART algorithms are simultaneous ART (SART) [AH and AC, 1984] and multiplicative ART (MART) [Herman, 1995]. SIRT algorithms are currently the most important algorithms for emission tomography. These algorithms are based on a certain statistical model e.g., a Poisson model or a Gaussian model of the data). Typical algorithms are maximum likelihood expectation maximization (ML-EM) [Shepp and Vardi, 1982] [Lange and Carson, 1984], MAP [Ganan and McClure, 1985], least squares (LS), and their variants, such as OS-EM [Hudson and Larkin, 1994]. An advantage of the iterative algorithms is that they allow a more detailed model of the image acquisition process, which is beneficial in resolution recovery and noise reduction [Rahmim et al., 2008].

Mathematically speaking, image reconstruction is an inverse problem, which is usually ill-posed. An ill-posed problem was first defined by Hadamard in 1917 [Bertero and Boccacci, 1998]. A ill-posed problem has no solution or many solutions. In addition, the solution does not depend continuously on the data. That is to say, when there is an arbitrarily small change in the data (e.g., contamination caused by noise), there may be an arbitrarily large error in the solution. Typical reconstruction problems have a solution but the solution is not unique. As a result, an arbitrarily small perturbation in the measurement may cause considerable noise in the reconstructed image. In numerical analysis, the term ill-posedness can be interpreted as ill-conditionedness because the error is considerably amplified. For medical imaging reconstruction, especially in emission tomography, the ill-posedness is mainly caused by the non-perfect detector, which cannot collect all the information required for an exact reconstruction. The ill-posedness can be reduced by introducing some priors, such as smoothness of the radiotracer distribution, etc. These priors are used in the regularization term to restrict the data matching term.

This section will introduce the basics of the reconstruction problem, with an emphasis on resolution modeling. The image quality degradation factors are of primary significance in this context. In practice, the resolution modeling largely depends on the choice of the object parameterization and the accuracy of the system model. The choice of an appropriate object parameterization could be the key to successful resolution modeling.

2.5.1 Problem formulation

The measured signal originates from decays of nuclides in emission tomography (both PET and SPECT). These nuclides are administrated to the patient. Thus, the imaged object in emission tomography is the distribution of radiopharmaceuticals, denoted as $f(\mathbf{r})$ where $\mathbf{r}$ is a vector representing the decay or annihilation location in three-dimensional (3D) Euclidean space. This principle is not the same as in CT or MRI, where the imaged object reflects the anatomical structure of the body. The object $f(\mathbf{r})$ can always be treated as a vector in Hilbert space $\mathbb{L}_2$. Thus, the function $f(\mathbf{r})$ can be further expressed as the linear combination of a set of basis functions as:

$$f(\mathbf{r}) = \sum_{j=1}^{\infty} x_j b_j(\mathbf{r}) \tag{2.7}$$

where $b_j(r)$ are the basis functions, and x_j are the coefficients of the linear combination.

The measurement, on the other hand, is discrete. The data are denoted as $\mathbf{y} = (y_0, y_1, , y_N)$, which is a vector with each element y_i representing the number of detected events of a detector bin or LOR, and N is the total number of detector bins. Consequently, the image reconstruction problem becomes a continuous-to-discrete mapping problem [Lewitt and Samuel, 2003]. For emission tomography, the imaging formation can be expressed as:

$$E(y_i) = \int h_i(\mathbf{r}) f(\mathbf{r}) d\mathbf{r} + s_i \tag{2.8}$$

The expected count $E(y_i)$ at detector pair i is determined by the sensitivity function $h_i(\mathbf{r})$ associated with LOR i at r and s_i is the expectation of scattered events. Using 2.7, equation 2.8 can be expanded as:

$$E(y_i) = \int h_i(\mathbf{r}) x_j b_j(\mathbf{r}) dr + s_i = x_j \int h_i(\mathbf{r}) b_j(\mathbf{r}) dr + s_i \tag{2.9}$$

It is not feasible to estimate the infinite radiotracer distribution $f(\mathbf{r})$ from the finite observations y_i because the problem is extremely under-determined. In practice, especially for tomographic reconstruction, the large demand on computational power requires the object to be represented in a discretized form in order to perform an image reconstruction on a computer. The object is truncated and approximated by a linear combination of M basis functions. Thus, equation 2.7 can be modified to the following form:

$$f(\mathbf{r}) \approx \tilde{f}(\mathbf{r}) = \sum_{j=1}^{M} x_j b_j(\mathbf{r}) \tag{2.10}$$

Consequently, equation 2.8 can be expressed as:

$$E(y_i) = \int h_i(\mathbf{r}) f(\mathbf{r}) d\mathbf{r} + s_i = \int \sum_{i=1}^{N} x_j h_i(\mathbf{r}) b_j \mathbf{r} + s_i = \sum_{j=1}^{M} x_j a_{i,j} + s_i \quad (2.11)$$

where $a_{i,j}$ is defined as:

$$a_{i,j} = \int h_i(\mathbf{r}) b_j(\mathbf{r}) dr \quad (2.12)$$

Equation 2.12 is the link between the emission distribution and the measured data. It represents the expectation of an emission originating from location r to be detected by LOR i. This term is usually called the system matrix or system transition matrix.

2.5.2 Major Components in Iterative Reconstruction Algorithm

Fessler et al. summarized the major components of an iterative reconstruction algorithm [Fessler, 1994]. The first component is the object parameterization, or basis functions used to represent the object. The second component, the system model, is also called the system matrix that models the system characteristics based on the chosen basis functions. The third component is the statistical model, or the statistical distribution that is assumed for the measured data. The fourth component is the cost function of the optimization problem, which an iterative reconstruction algorithm tries to either maximize or minimize. The cost function has two terms, the data-mismatch term and the regularization term. The last component is the optimization algorithm, by which we achieve a maximum or minimum of the cost function.

2.5.2.1 Object parameterization

The object is truncated and represented by a linear series expansion of a set of basis functions, as described in section 2.5.1. Thus, the object is now represented as a vector $\mathbf{x} = (x_1, x_2, ..., x_M)$, where x_j is the coefficient of the basis function b_j, denoted as:

$$f(\mathbf{r}) \approx \tilde{f}(\mathbf{r}) = \sum_{j=1}^{M} x_j b_j(\mathbf{r}) \quad (2.13)$$

Typical linear basis functions are cubic voxels, polar-pixels [Mora and Rafecas, 2006, Leroux et al., 2007b, Ansorge, 2007], blobs (generalized Kaiser-Bessel window functions) [Matej and Lewitt, 1995, Matej and Lewitt, 1996], natural pixels $\{h_i(\mathbf{r})\}$ [Buonocore et al., 1981], and B-splines [Verhaeghe et al., 2008]. There

are many non-linear basis functions of choice, such as the mesh model and adaptive mesh models [Brankov et al., 2004], as illustrated in Fig. 2.9.The criteria for choosing an appropriate basis function are largely requirement-driven. However, in all cases, the object must be well represented by the basis function. The choice of basis function has a large influence on the image quality and the complexity of the reconstruction problem (e.g., the blob and polar pixels). Generally, a smooth basis function is preferred because the objects are continuous in the physical world. This concept is illustrated in Fig. 2.10.

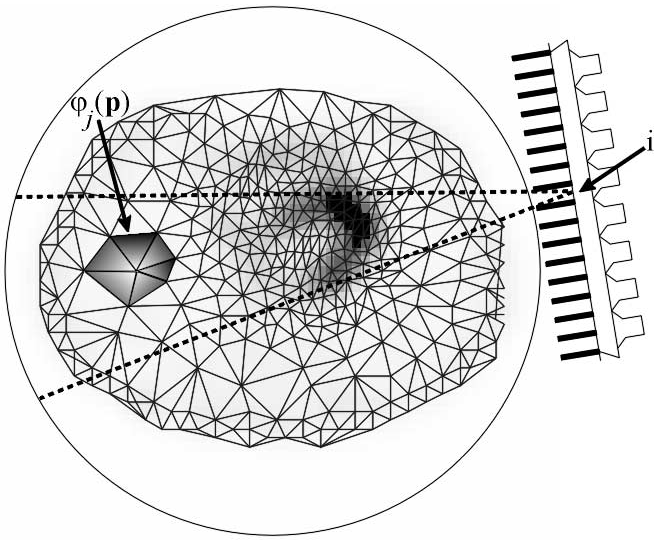

Figure 2.9: An example of the mesh object parameterization.

2.5.2.2 System model

Definition With the definition of the object parameterization, the system model can be defined as a matrix $\mathbf{A} = \{a_{i,j}\}$:

$$a_{i,j} = \int h_i(\mathbf{r}) b_j(\mathbf{r}) d\mathbf{r} \tag{2.14}$$

The system model, generally speaking, includes all known factors related to the patient scan, such as the geometry of the scanner, the crystal configuration, the detector efficiency and dead time, the energy resolution and time resolution, the geometry and composition of the patient, and physical degradation factors, including the positron range, the acolinearity of

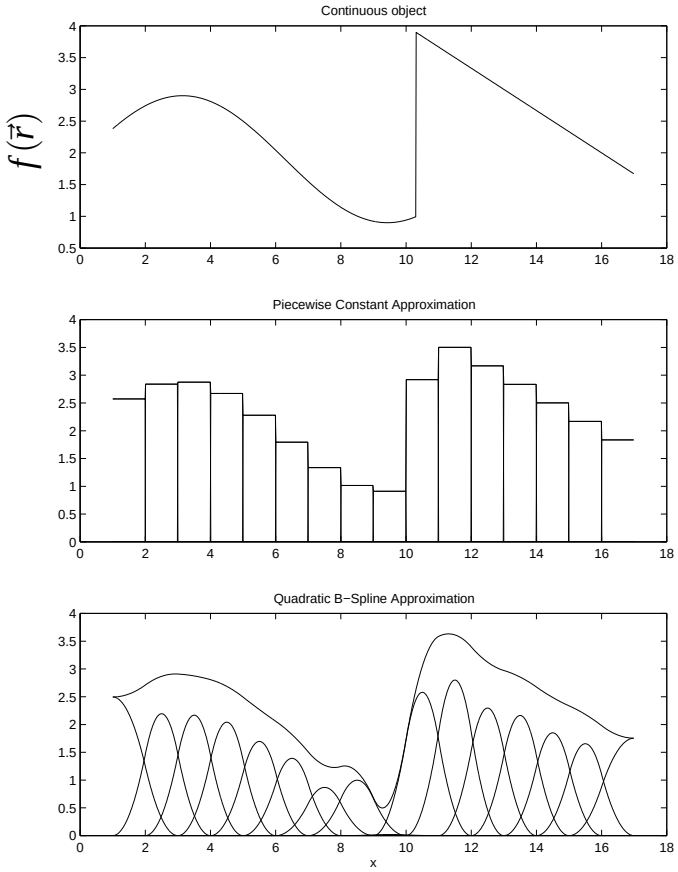

Figure 2.10: Representing a continuous object (1-D) by smooth basis functions and pixels. Courtesy Dr. J. A. Fesseler.

the annihilation photons, the crystal penetration, and inter-crystal scattering. These factors are known prior to the emission tomography reconstruction and can be divided into two classes: the object-dependent factors and system-dependent factors [Zhang et al., 2010c]. Object-dependent factors refer to effects that are primarily determined by the properties of the object, e.g., photon attenuation and scattering within the patient. System-dependent factors are the factors that are mainly related to the scanner of interest. Typical system-dependent factors are scanner geometry, crystal configuration and of course the material of the crystals. These parts of the system model (together with photon attenuation inside the study subject) are often used in practice in the resolution compensation of a scanner. Some tricky parts such as positron range and acolinearity of the annihilation photons are usually clustered with the system-dependent factors and modeled in projection space even though the positron range is primarily an object-dependent factor [Zhang et al., 2010c] and the acolinearity is dependent on both the system and the object [Iwata et al., 1997]. We found that image space modeling is algorithm-dependent if it has to be estimated by an inverse process [Zhang et al., 2010d]. The same phenomenon has been reported by other researchers [Cloquet et al., 2009]. This classification is reasonable because researchers usually use the positron range and acolinearity measured in water to reduce the object-dependency of these two effects [Zhang et al., 2010c]. In a measured system model, these effects only depend on the composition of the point source and are also independent of object properties.

Calculation Various methods have been proposed to calculate the system model. These methods can be divided into three categories: the analytical approaches, the Monte Carlo-based approaches, and the measurement-based approaches. Analytical resolution models are usually biased and under-estimate the blurring of system responses due to over-simplifications in describing the scanner model and the acquisition process. For instance, the line-length of intersection with a voxel has been used to represent the solid angle effects [Siddon, 1985]. Less biased approaches use more accurate models to approximate the geometric response by calculating the area of intersection or volume of intersection [Scheins et al., 2006]; studies have shown that a tube of response (3-D) or a strip of response (2-D) is more appropriate than the line of response [Terstegge et al., 1996] [Vandenberghe et al., 2001]. Recently, detector responses and physical effects, e.g., the positron range, acolinearity, parallax error, and inter-crystal scattering have been included in analytical models with [Rahmim et al., 2008, Moehrs et al., 2008a] or without the help of Monte Carlo simulations [Staelens et al., 2004, Selivanov et al., 2000].

Theoretically, a bias-free system model can be measured using a scanning

point source. One limitation of these methods is the need for extensive scanning [Panin et al., 2006a]. These methods assume a certain distribution of the system response (e.g., an asymmetric Gaussian) to parameterize it because the scanning grid is relatively sparse compared to the voxel grid [Panin et al., 2006b, Panin et al., 2006a, Alessio et al., 2010, Wiant et al., 2010]. Unfortunately, this assumption introduces bias in the system model. In addition, these methods cannot address object-dependent factors, such as photon attenuation and scattering.

In contrast to analytical methods and measurement approaches, Monte Carlo resolution modeling (MCRM) methods are bias-free[2] and have the potential to model both system-dependent factors [Johnson et al., 1995,Qi et al., 1998, Rannou and Chatziioannou, 2004, Rafecas et al., 2004b, Shokouhi et al., 2004, Mora and Rafecas, 2006, Ansorge, 2007, Leroux et al., 2007a] and object-dependent factors [Watson et al., 1997] [Rehfeld and Alber, 2007] [Rehfeld et al., 2010]. However, the computational load to calculate the SM has limited the use of these methods for state-of-the-art whole-body PET scanners [Buvat and Lazaro, 2006, Panin et al., 2006a]. To address these problems, symmetries have been exploited to reduce the redundancy in the SM [Johnson et al., 1995, Qi et al., 1998, Rannou and Chatziioannou, 2004, Rafecas et al., 2004b, Shokouhi et al., 2004, Mora and Rafecas, 2006, Vandenberghe et al., 2006, Ansorge, 2007, Leroux et al., 2007a]. Alternative symmetry handling methods have been proposed by using a rotationally invariant object model, such as polar pixels [Mora and Rafecas, 2006], [Ansorge, 2007], [Leroux et al., 2007a], [Scheins and Herzog, 2008] and the generalized natural pixels [Vandenberghe et al., 2006]. Non-exact approaches, i.e., "quasi-symmetry" [Herraiz et al., 2006] and approximate rotational symmetry [Qi et al., 1998], have also been proposed.

The system model can be expressed as a factored matrix approach [Qi et al., 1998] [Reader et al., 2003] [Rahmim et al., 2005]:

$$\mathbf{A} = \mathbf{PGW} \tag{2.15}$$

where $P^{N\times N}$ represents projection space factors, such as photon attenuation correction factors (ACF), detector efficiency correction factors, and in-projection space blurring (unless it is clustered in G, e.g., when a measured system model is used), $G^{N\times M}$ represents effects that contribute to the mapping of the source distribution to the projection (such as geometric responses), depth-dependent system sensitivity, crystal penetration, and inter-crystal scattering, and W represents effects in image space (such as

[2]This conclusion is valid if and only if the simulator is validated against the physical scanner

the positron range). A constraint of this factored matrix approach is blurring in projection space [Tohme and Qi, 2009] and image space [Cloquet et al., 2009], which is found to be algorithm-dependent if blurring were estimated as an inverse problem.

Projectors Measured data are obtained by the integral of the source distribution weighted by the sensitivity function over the object:

$$\int h_i(\mathbf{r}) f(\mathbf{r}) \tag{2.16}$$

Using equation 2.10, the forward projection in a D-D model becomes a summation, which can be expressed as:

$$\bar{y_i} = \int h_i(\vec{r}) \tilde{f(\mathbf{r})} \quad = \int h_i(\mathbf{r}) \left[\sum_{j=1}^{M} x_j b_j(\mathbf{r}) \right] = \sum_{j=1}^{M} \int h_i(\mathbf{r}) \left[x_j b_j(\mathbf{r}) \right] \tag{2.17}$$

Using equation 2.14, equation 2.17 can be written as:

$$\sum_{j=1}^{M} a_{i,j} x_j = [\mathbf{Ax}]_i \tag{2.18}$$

The backprojection maps the measurements or the errors back into the image space:

$$x_j = \sum_{i=0}^{N} a_{i,j} y_i = \left[\mathbf{A}^{'} \mathbf{y} \right]_i \tag{2.19}$$

2.5.2.3 Statistical model

The system model gives the expected response of the scanner. Thus, it is a deterministic model:

$$\bar{y_i} = [\mathbf{Ax}]_i \tag{2.20}$$

However, the measurement $\mathbf{y} = \{y_i\}$ is typically very noisy in emission tomography. Thus,

$$y_i \neq \bar{y_i} = [\mathbf{Ax}]_i \tag{2.21}$$

To solve this discrepancy, we need to assume that the data has a certain statistical distribution. The most common data model for emission tomography is the Poisson model, and by ignoring or pre-correcting for background, it can be expressed as:

$$y_i \sim Poisson \{[\mathbf{Ax}]_i\} \tag{2.22}$$

or with the background r_i considered:

$$y_i \sim Poisson\left\{[\mathbf{Ax}]_i + r_i\right\} \tag{2.23}$$

With a proper statistical model, the inconsistency in the data can be reduced. This leads to improved image quality, and naturally, lower variance.

2.5.2.4 Cost function

The cost function, also called the objective function, is a function which needs to be minimized (or maximized) in order to get a solution.

$$\hat{\mathbf{x}} = \arg\max_{\mathbf{x}\geq 0} \Psi(\mathbf{x}) \tag{2.24}$$

For emission tomography, the most popular algorithm is the maximum likelihood expectation maximization (ML-EM). For Poisson likelihood, the cost function used in this algorithm is:

$$\Psi(\mathbf{x}) = -L(\mathbf{x};\mathbf{y}) \tag{2.25}$$

$$= -logp(\mathbf{y}|\mathbf{x}) \tag{2.26}$$

$$= \sum_{i=1}^{N}([\mathbf{Ax}]_i + r_i) - y_i log([\mathbf{Ax}]_i + r_i) + log(y_i!) \tag{2.27}$$

2.5.2.5 Optimization algorithm

Once a cost function is defined, the (global) maximum can be found through the use of an optimization algorithm, which is usually an iterative process. A good optimization algorithm is stable and convergent, which means that $\{\mathbf{x}^n\}$ always converges to $\hat{\mathbf{x}}$ if the algorithm is iterated indefinitely. In practice, we would prefer an optimization algorithm that converges quickly (i.e., it approaches to $\hat{\mathbf{x}}$ in a few iterations).

The ML-EM algorithm, for instance, optimizes the cost function ML (equation 2.27) using the optimization algorithm EM. The object parameterization can be voxels or polar-pixels, which will be addressed in details in chapter 4, 5 and 6. The system model can be a line-length model, a Monte Carlo-based model (see Chapter 4 or a experimental model (see Chapter 5). The EM algorithm is frequently used in parameter estimation with incomplete data. The algorithm is composed of two steps, the E-step and the M-step.

The E-step calculates the expectation of the log-likelihood of a Poisson likeli-

hood, which is the statistical model.

$$L(\mathbf{x};\mathbf{y}) = \sum_i \left[-\sum_j a_{i,j}x_j + y_i ln(\sum_j a_{i,j}x_j) \right] \tag{2.28}$$

$$\geq -\sum_i \sum_j a_{i,j}x_j + \sum_i y_i \sum_j \frac{a_{i,j}x_j^n}{\sum_k a_{i,k}x_k^n} ln(x_j) + const \tag{2.29}$$

The M-step gets a new estimate of $\mathbf{x}^{n+1}$ by maximizing equation 2.29:

$$x_j^{(n_1)} = \arg\max_{x_j \geq 0}(x_j^n \sum_i \frac{a_{i,j}y_i}{\sum_k a_{i,k}x_k^{(n)} ln(x_j)} - x_j \sum_i a_{i,j}) \tag{2.30}$$

Let the first order derivative of M-step 2.30 to be zero and solving it analytically, one gets:

$$0 = x_j^{(n)} \sum_i \frac{a_{i,j}y_i}{\sum_k a_{i,k}x_k^{(n)}} \frac{1}{x_j} - \sum_i a_{i,j} \tag{2.31}$$

$$\Rightarrow x_j^{(n+1)} = \frac{x_j^{(n)}}{\sum_i a_{i,j}} \sum_i \frac{a_{i,j}y_i}{\sum_k a_{i,k}x_k^{(n)}} \tag{2.32}$$

Equation 2.32 is the well-known ML-EM algorithm. This ML cost function implies a Poisson statistical model of the data, which is the statistical model. It can be seen that the ML-EM algorithm implies a non-negative constraint on the object for a Poisson noise model.

2.5.3 Quantitative techniques in PET reconstruction

2.5.3.1 Randoms correction

The orgins of randoms have been described in section 2.4.5.3. For PET, the rate of random coincidences of a LOR is estimated by:

$$R_{i,j} = 2\tau r_i r_j \tag{2.33}$$

where $R_{i,j}$ is the random rate of a LOR defined by detector i and j, τ is the coincidence window, and r_i and r_j are the rate of singles on the corresponding detector.

The randoms rate is often determined by experimental method by the dual window method (also called the delayed window method). In this method, the timing signals from one detector are delayed by a time significantly longer than the coincidence window. Thus, the timing signals are not correlated with the signals from the other detector. These "coincidences" are the measured randoms and are then subtracted online or stored for later processing. This method suffers from

poor counting statistics because the number of randoms is very limited. Methods to improve the noise characteristics of the random estimate have been developed by utilizing randoms collected for a detector and a 2-D or 3-D fan of detectors opposite to it [Casey and Hoffman, 1986] [Badawi et al., 1999].

2.5.3.2 Attenuation correction

The photon attenuation of a patient is assumed to be a known factor prior to reconstruction. Thus, photon attenuation must be measured along or before the emission acquisition. For a PET/CT scan, the attenuation map is usually estimated from the CT image. As the energy of interest is different in PET and CT scanners, a linear or bilinear conversion has to be performed to translate a CT image into a PET attenuation map for typical biological materials [Kinahan et al., 1998] [Kamel et al., 2003] [Pan et al., 2005]. For a PET only scanner, the attenuation map is usually estimated by performing a transmission scan using a positron emission isotope or a gamma emission isotope separately or simultaneously [Meikle et al., 1993] [Karp et al., 1995] [Meikle et al., 1995] or from the emission scan itself [Nuyts et al., 1999] [Liu et al., 2006]. A similar transformation has to be performed if the energy of the gamma photon is not 511 keV for the same reason as in the PET/CT case. The attenuation map can also be determined by a segmented MRI image in a PET/MR scanner [Kops et al., 2007] [Montandon and Zaidi, 2005] [Schreibmann et al., 2010] [Keereman et al., 2010] [Catana et al., 2010].

2.5.3.3 Scatter correction

As mentioned in Section 2.4.5.4, the scatters are usually estimated in a separate step, which yields a scattering sinogram. One well-established method is the single scatter simulation (SSS) technique [Watson et al., 1997] [Werling et al., 2002] [Accorsi et al., 2004]. This method requires a rough estimation of the source distribution and an attenuation map of the imaged subject. The rough estimation can be either the post-smoothed FBP reconstruction or a 2-D statistical iterative reconstruction.

Recent approaches [Rehfeld and Alber, 2007] [Rehfeld et al., 2010] models the scattering SM as an additive term in Equation 2.15:

$$\mathbf{A} = \mathbf{A_{sf}} + \mathbf{S} \tag{2.34}$$

where $\mathbf{S}^{N \times M}$ is the scattering matrix, which determinates the scattered contribution to an LOR-basis function pair, and the term $\mathbf{A_{sf}}$ refers to the scatter-free SM.

However, it is not practical to include the effects of object scattering in the resolution compensation of a PET scanner because of constraints in computational resources.

2.6 Monte Carlo simulation in PET

Monte Carlo methods (or Monte Carlo experiments) are a class of numerical algorithms that mimic a real physical process by sampling from known probability density functions to compute the result of a problem. Monte Carlo methods are essentially "numerical" experiments. The accuracy of this algorithm depends on how accurately the process is simulated and the number of "experiments" performed. Thus, these algorithms are mostly implemented on computers and are usually applied in problems where it is not feasible or necessary to obtain an exact result by a closed-form analytical formula. Monte Carlo simulation is heavily used in medical imaging physics because the scanner geometry and the topology of a patient cannot yet be modeled by analytical means. Literature [Zaidi, 1999] [Buvat and Castiglioni, 2002] gives a more complete description of the significance and applications of this method in medical imaging.

The applications of Monte Carlo simulations in PET generally lie in the following fields:

Quantitative techniques The modeling of imaging physics of PET has been largely employed in quantitative techniques, particularly, scattering correction [Watson et al., 1997] [Werling et al., 2002] [Accorsi et al., 2004] [Wollenweber et al., 2000] [Qi and Huesman, 2002] [Holdsworth et al., 2003] [Barret et al., 2005].

Modeling of PET detectors Simulations of detectors are frequently performed in PET instrumentation to optimize scanner design such as, scintillation materials choice, crystal size, signal processing chain optimization, etc [Derenzo, 1981] [Cherry et al., 1995] [Binkley, 1992] [Choong, 2009].

Image Reconstruction The reconstruction algorithm, particularly, newly developed algorithms, are usually first evaluated by Monte Carlo simulated data. This method is capable of providing a baseline performance of the algorithm with trues only. As mentioned in Section 2.5.2.2, Monte Carlo-based reconstruction is capable of modeling all system-dependent factors [Johnson et al., 1995, Qi et al., 1998, Rannou and Chatziioannou, 2004, Rafecas et al., 2004b, Shokouhi et al., 2004, Mora and Rafecas, 2006, Ansorge, 2007, Leroux et al., 2007a, Zhang et al., 2010c] and object-dependent factors [Rehfeld and Alber, 2007, Rehfeld et al., 2010].

Acquisition protocol Monte Carlo simulation techniques can be used to optimize the acquisition protocols of clinical PET scans [Tang et al., 2008].

Pharmacokinetic modeling Monte Carlo techniques can be applied in pharmacokinetic modeling to estimate the cumulated activity distribution in the body [Zeng et al., 1994a] [Millet et al., 1996] [Wang and Qi, 2009].

This book is also an example of exploiting Monte Carlo simulations in PET image reconstruction. For this particular task, a highly optimized and yet realistic Monte Carlo PET simulator is required. In addition, the code needs an architecture that allows development of various variance reduction techniques for better simulation efficiency. There are many existing PET Monte Carlo simulators, such as PETSIM [Thompson et al., 1992], SimSET [Lewellen et al., 1998], GATE [Jan et al., 2004], PenelopePET [Espana et al., 2009], PET-SORTEO [Reilhac et al., 2005]. We chose egs_pet as the basis to develop our own system matrix simulation tool because the others were not applicable (i.e. not efficicent enough) or not ready or needed a special license to use at the time we started resolution modeling. EGSnrc stands for "electron gamma shower" (by) national research council, which is maintained by NRC, Canada. The EGSnrc system is a general purpose Monte Carlo simulation package inherited from the EGS4 code developed at the Stanford linear accelerator center (SLAC) (http://www.slac.stanford.edu/) but with many improvements. The energy range of applicability is from 1 KeV to 10 GeV. This Monte Carlo code system has been widely used in radiotherapy and is usually regarded as the gold standard in this field.

The egs_pet code is a user code of the EGSnrc system using the newly released C++ interface, the egspp [Kawrakow et al., 2009]. The lower level part of egs_pet is the EGSnrc system, which responses for the coupled electron-photon transport and physical interaction simulation. The egs_pet interacts with the EGSnrc library through three routines: *hownear*,*howfar* and *ausgab*, as illustrated in Fig. 2.11. Routines *hownear* and *howfar* specify the geometry boundaries and the routine *ausgab* is the interface to probe, alter, and score the simulation process. The code first initializes the EGSnrc package with user provided macro files. after initializing EGSnrc package, the code guides the transport of particles in media through the *howfar* and *hownear* routines. The score is usually extracted from the simulation in the routine *ausgab*.

The user code egs_pet supports three types of sources, namely the positron source, the back-to-back gamma source, and the back-to-back gamma source with acolinearity. The code egs_pet provides a set of signal processing chain modules for PET, called the pulse processors in egs_pet, which are equivalent to the corresponding modules in GATE. These modules include an adder module, a readout module, an energy window module, an energy blurring module, a coincidences sorting module and a root output module. The root module supports singles, coincidences and annihilation information.

The egs_pet code system provides both accurate low energy cross section tables and highly efficient coupled electron (positron) photon transport. It has a lightweighted structure with inherent support for various variance reduction techniques. A constraint of this user code is the shortage of much basic functionality (e.g. some primitive geometry components) and is relatively difficult to use.

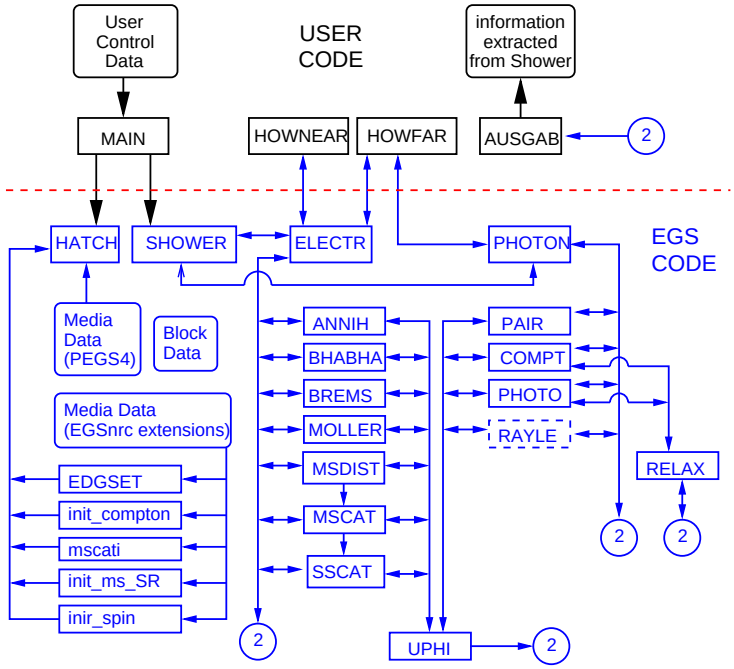

Figure 2.11: The user code - EGSnrc interface. The user code first initializes the EGSnrc package with user provided macro files. After initialization, the user code guides the transport of particles through the howfar *and* hownear *routines. The score is extracted from the simulation in the routine* ausgab*. Courtesy NRC, Canada*

Interested readers may refer to Simulation System for Emission Tomography (SimSET) for an alternative tool in resolution modeling [Lewellen et al., 1998]. This package is optimized for realistic acquisition simulation, but the electron tracking is not included.

2.7 General conclusion

In this chapter, we covered the basic physics, the instrumentation, the basic theory of imaging reconstruction and Monte Carlo simulation for PET imaging. Much of this information is not only relevant to PET but also to SPECT imaging because these two image modalities are closely related. This introduction gave an overview of the principles of PET imaging and prepared the necessary background knowledge about Monte Carlo-based resolution modeling for PET reconstruction, which is the main topic of this dissertation.

In the following chapter, advanced simulation techniques in resolution modeling are introduced. The assumptions and simplifications of system modeling are also introduced. With these techniques, the simulation efficiency can be improved considerably without compromising the accuracy of the simulation.

Chapter 3

Variance Reduction Techniques in Resolution Modeling

In this chapter, all the variance reduction techniques (VRTs) we developed are summarized. Dr. Iwan Kawrakow has equal contribution to this chapter as the author. This study was performed after the our Monte Carlo- and experiment-based resolution modeling (Chapter 4, 5, 6). Thus, not all of the techniques described here were used in these chapters. This work is mainly motivated by the fact that the reconstruction with the proposed Monte Carlo model is very noisy.

3.1 Introduction

Monte Carlo-based resolution modeling can effectively improve the image quality in Positron Emission Tomography (PET). The improvement is usually achieved by compensating for various resolution degradation factors in image acquisition process, namely solid angle effects, the positron range, acolinearity of the annihilation photons, the parallax error, and inter-crystal scattering. Resolution modeling is usually performed through a model called system matrix (SM), which can be employed in an iterative reconstruction algorithm to improve the image quality.

Although the mathematics of the system model is clearly defined, the calculation of the SM has been significantly challenged for modern PET scanners. The first challenge lies in the complexity of deriving a bias-free analytical model for a PET scanner. Such a model is almost not feasible due to the large number of degrees of freedom, which are usually also coupled. Stimulation of the SM can be accelerated by employing light weight Monte Carlo simulators [Rafecas et al., 2004b, Shokouhi et al., 2004] and VRTs.

Geometry equivalence or employing symmetries is the simplest VRT and is also the most frequently used technique to speed-up the simulation of the SM [Johnson et al., 1995, Qi et al., 1998, Rannou and Chatziioannou, 2004, Rafecas et al., 2004b, Shokouhi et al., 2004, Mora and Rafecas, 2006, Vandenberghe et al., 2006, Ansorge, 2007, Leroux et al., 2007a]. Other standard VRTs, such as the importance sampling technique and the forced detection technique, have also been used in resolution modeling of small animal PET scanners [Shokouhi et al., 2004]. Advanced VRTs, such as pre-computation techniques have been employed to calculate the dose distribution in therapeutic applications. The pre-computation method first derives the probability density functions of certain tallies associated with predefined physical processes and particles through analog simulations. These probability density functions are then used to transport of the particles. This technique has been employed to simulate detector responses in PET [Ortuno et al., 2006] [Ortuno et al., 2010] and SPECT [Descourt et al., 2008]. A more efficient method is to derive analytical formula of the probability density functions directly, for instance, the positron range and the acolinearity in SimSET are simulated in this way [Harrison et al., 1999].

In this chapter, we analyze the unique challenges of SM simulation and propose a set of simple VRTs for the resolution modeling task using EGSnrc-based PET simulator, the egs_pet [Kawrakow et al., 2008c]. For general PET and SPECT simulation techniques, interested readers are encourage to read literature [Haynor et al., 1991] [Lewellen et al., 1998] [Kawrakow et al., 2008b] for more detailed information.

3.2 Materials and Methods

3.2.1 Figures of merit

3.2.1.1 Precision

The precision of tally in a resolution modeling simulation is measured by the error defined as:

$$\epsilon = \frac{\sigma(N_d)}{N_e} \tag{3.1}$$

where $\sigma(N_d)$ is standard deviation of the number of detections (prompts) N_d, and N_e refers to the number of the simulated events in the simulation. In this chapter, we proposed some VRTs that introduce bias, but the bias is not compensated by a corresponding weight. These VRTs are polar angle biasing and positron history reuse. When such VRTs are used, N_e has to be adjusted to compensate for the bias. The methods on the compensation will be discussed in section 3.2.3.1 and section 3.2.3.3. The quantity $\sigma(N_d)$ measures the uncertainty in forward projection to ensure that the error in the reconstructed image is insignificant [Qi and

Huesman, 2005]. The uncertainty in the back projection is automatically ensured by the number of events simulated in a voxel (e.g., 50 million decays [Shokouhi et al., 2004]).

3.2.1.2 Efficiency evaluation

The efficiency of a SM simulation was measured by η:

$$\eta = \frac{1}{s^2 T} \tag{3.2}$$

where T is the execution time of the simulation, and s^2 is the variance of the estimated tally. In this work, we use $s = \epsilon$, which is given by Equation 3.1.

3.2.2 SM simulation

The SM was simulated for the Philips Gemini GS PET scanner. This scanner has 28 detector modules. Each module consists of an array of 22x29 crystals with a dimension of 4 mm (tangentially) by 6 mm (axially) by 20 mm (length), which form 29 rings with 616 crystals per ring and a ring pitch of 6.3 mm [Lamare et al., 2006]. The voxel dimension is chosen as 2mm$\times$2mm$\times$3.15mm, which yields two image planes per ring that are symmetric about the central plane of the ring.

We used a uniform source with and without a water phantom in our system matrix simulation. In a whole-body scan using ^{18}F, it is not necessary to include the effects of the positron range. Thus, a water phantom is not necessary. However, for a small animal PET scan or a non-standard isotope, a water phantom is very important because the positron range significantly improves the image quality [Bai et al., 2005]. The water phantom was considerably larger than the source to allow sufficient positron tracking. The EGSnrc-based PET simulator egs_pet was used in this work, which was reported to be 15 - 120 times (depends on a specific configuration) faster than GATE. The coincidences were grouped according to their voxel and LOR indices in the post-processing step. The number of coincidences was recorded as the value of the corresponding SM element because this value is proportional to the absolute value of the corresponding SM element. This approach integrated the point spread function within a uniform voxel, which yields a "voxel spread function".

We assumed that the system model was independent of the acquisition parameters in resolution modeling [Panin et al., 2006a]. In reality, different system sensitivities can occur with different acquisition parameters. For instance, at a higher count rate, a larger fraction of randoms and a lower fraction of true coincidence can be expected. To avoid this problem, we assumed that the activity of the source was so low that the time interval between two events was sufficiently long compared to the coincidence window; this is denoted as the "time independence"

assumption. This assumption yielded a simulation free of randoms and enabled a faster signal processing chain because the interference among events and dead time effects were ignored. In addition, if one of the two back-to-back photons [1] was not traveling towards a detector, the whole event was discarded because a coincidence would not be possible [Rafecas et al., 2004b].

Another assumption in our resolution modeling was the exclusion of object-dependent factors. Although recent approaches implemented patient-specific resolution modeling, the feasibility of generating a patient-specific system model that met clinical requirements is still under-investigation [Buvat and Lazaro, 2006] [Panin et al., 2006a] [Rehfeld and Alber, 2007] [Rehfeld et al., 2010]. Object-dependent factors include namely, the positron range and acolinearity, photon attenuation, and scattering within the object. To exclude these factors, we used a water phantom, but disabled photon-matter interactions within the phantom in the SM simulation. Thus, in our study, positron range and acolinearity values in water were used to reduce their object dependency as recommended by [Shokouhi et al., 2004]. The acolinearity is not modeled in the current release of EGSnrc [Kawrakow and Rogers, 2007], so we modeled this effect in water as recommended by Harrison et al. [Harrison et al., 1999].

3.2.3 Implemented variance reduction techniques

3.2.3.1 Polar angle biasing

Generally, a PET scanner has a limited axial extent due to engineering constraints and for the purposes of patient comfort. The effective solid angle is limited across the FOV of the scanner. Thus, the polar angle of the annihilation photon must be within a certain range to hit the scanner ring. The range of the polar angle is both location- and azimuthal-angle-dependent. The maximum range of the polar angle is used as the effective range of the polar angle across the whole FOV, which cancels the dependence on the location and the azimuthal angle. The effective range can be exploited to improve the simulation efficiency by avoiding the generation and transport of photons that cannot produce valid coincidences. It can be proven that the maximum effective range is found at the edge of the FOV in the central plane and the minimum effective range is found at the center of the FOV if the acolinearity is not considered, as illustrated in Fig. 3.1. The $\theta_{\max}$ and $\theta_{\min}$ correspond to the maximum range and the minimum range of the effective polar angle in the FOV. θ_{off} is half of the effective range at an off-center location within the same plane.

In practice, the annihilation photons are not strictly collinear. The angular deviation from a straight line follows a Gaussian distribution with a FWHM of about

[1] photons that are emitted in opposite direction

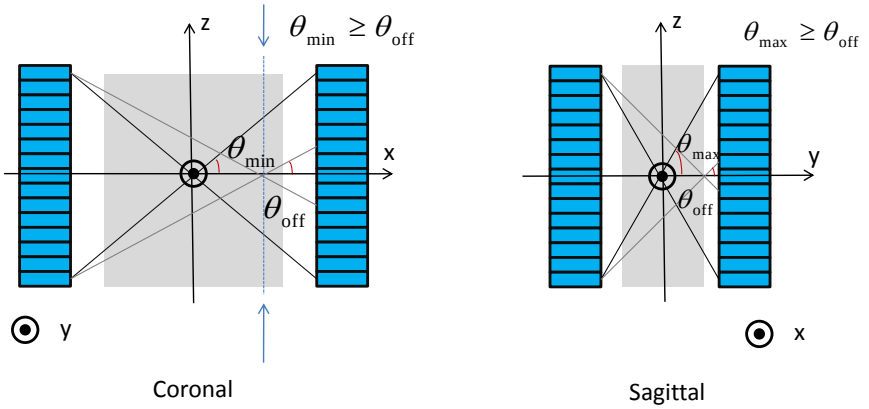

Figure 3.1: The effective range of the polar angle is location-dependent. The maximum effective range of the polar angle is found at the edge of the FOV; the minimum effective range of the polar angle is found at the center of the FOV.

0.25 degree for ^{18}F [Cherry et al., 2003]. In a simulation, the polar angle can be biased to be the effective range plus (or minus) 2 FWHM (approximately 5σ) of the acolinearity distribution. This technique introduces bias in the system sensitivity. We did not assign a weight to correct for the biasing because all photon pairs have the same importance and the absolute sensitivity is not of interest for resolution modeling simulation. In addition, a floating point weight is also incompatible with the system matrix storage schema in Chapter 4.

This importance can be estimated by launching two simulations of the source of the target simulation. Both simulations have the same activity. The first simulation is with polar angle biasing active, and the second one without polar angle biasing. The ratio of the number of detections of the second simulation to the first one can be used to compensate the sensitivity bias.

3.2.3.2 Hit-testing

Hit-testing evaluates whether a photon can reach the detector or not by checking if the ray intersects with the scanner cylinder. This test was performed after the positron-electron annihilation. If either photon in a pair failed to hit the detector, the whole event was discarded. This technique required the time-independent assumption and object-independent assumption because one detected photon may contribute to randoms and object scattering may deflect the photon to hit the detector without those assumptions. This technique could be used to avoid the transport of certain photons together with the polar angle biasing technique.

3.2.3.3 Positron history reuse

The positron history reuse technique reuses the transport histories of electrons by producing more than one pair of annihilation photons when a positron annihilates with an electron. These photon pairs will share the same positron track, but the directions of these photon pairs are randomly sampled. These photon pairs are then tracked and the obtained detections are sorted into coincidences independently, which is valid when the time independence assumption holds [2].

Correlations are introduced when pairs share the same antecedent positron. However, the correlations can be insignificant when the chances of these annihilation photon pairs contributing to the same LOR are very small. For instance, if a positron history is reused 20 times, less than one coincidence is produced on average for the Philips Gemini GS PET scanner with a point source at the center of the FOV. This technique performs particle splitting for the annihilation photons and a weight of the inverse of the number of splitting can be used to correct for this bias. In this work, we did not correct the bias for the same reason described in section 3.2.3.1.

3.2.3.4 Forced the energy window passing

Traditionally, a photon is forced to reach the detector [Haynor et al., 1991] [Harrison et al., 2002]. We forced a readout signal to pass the energy window. For instance, a readout signal may fail to pass the energy window due to the energy blur of the detector even though its energy was within the window. To avoid such losses, a forced detection was enforced and a weight was calculated from the probability of passing the energy threshold. The energy blurring was modeled as a Gaussian with a mean at the deposited energy E and a standard deviation σ, which was calculated by Equation 3.3:

$$\sigma = \frac{1}{2.35} ER \tag{3.3}$$

where R is the energy resolution of the scanner at this energy, which can be obtained given the energy of reference E_0 and the energy resolution of reference R_0 (FWHM):

$$R = R_0 \sqrt{\frac{E_0}{E}} \tag{3.4}$$

The overlapping area between the energy window and the Gaussian distribution is proportional to the probability of passing the energy window. The weight is calculated using the overlapping area and the new weight of the surviving single is $w \times w_{old}$, as illustrated in Fig. 3.2. Mathematically, the weight is the difference

[2] Otherwise, it would be difficult to assign realistic time for those annihilation photo pairs

between the cumulative density function of the Gaussian distribution at the upper and lower threshold of the energy window:

$$w = cdf(E_{upper}) - cdf(E_{lower}) \tag{3.5}$$

where cdf is expressed as:

$$cdf = \frac{1}{2}\left[1 + \text{erf}(\frac{x - E}{\sqrt{2\sigma^2}})\right] \tag{3.6}$$

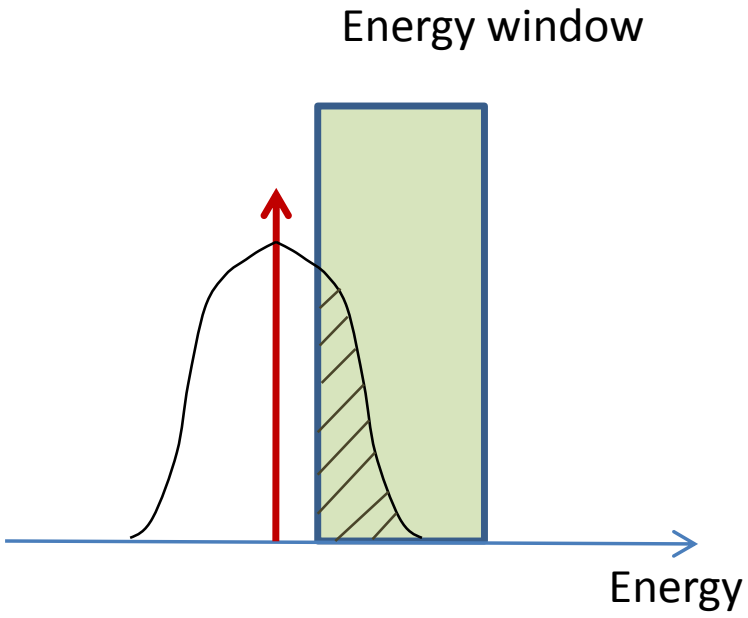

Figure 3.2: Illustration of the concept of forced passing the energy threshold.

3.2.3.5 Fictitious transport in the crystal array

Fictitious interaction tracking, also called Woodcock tracking or delta scattering, is frequently used in accelerating photon tracking in matters with relatively little variation in cross section at the photon energy of interest [Woodcock et al., 1965] [Cramer, 1977]. The human body is an appropriate candidate for this technique,

which allows a relatively longer free mean path compared to voxel dimension in simulation. The computational load caused by boundary crossing is avoided as the whole volume is regarded as isotropic media. The tracking uses a maximum cross section to sample the distance to travel but uses the ratio of maximum to local cross section to determine the occurrence and type of an interaction. This technique has been applied in photon tracking in collimator and crystal detectors [Tenney et al., 2004]. We applied this technique for photon transport in the crystal arrays because the crystal pitch is generally smaller than the free mean path in common scintillator for 511 keV photons (e.g. the free mean path is about 1 cm in BGO). The cross section of the crystal was used in transport. The interaction was determined by the local cross section at a fictitious interaction site.

3.2.3.6 Transport parameters

The transport parameters are often adjusted to get a better simulation efficiency given a required precision. In emission tomography, it is justifiable to switch off the transport of the secondary electrons in crystals [Wernick and Aarsvold, 2004]. This technique has become the standard configuration in emission tomography Monte Carlo simulators and the efficiency has been improved considerably. In PET resolution modeling, range rejection of positron can be applied with the same rationale to avoid this computational overload. However, this technique is not appropriate for small animal PET scanners or some non-standard isotopes where positron range matters [Bai et al., 2005] [Rahmim et al., 2008]. We did not apply this technique in our simulations because the positron history reuse technique relaxed this computational challenge.

Other parameters that can be adjusted are photon range rejection (*pcut* in EGSnrc), Rayleigh scattering and bounded Compton scattering. These parameters may not improve the simulation efficiency and have limited contributions to the simulation accuracy. However, their effects on the accuracy of resolution modeling remain uninvestigated. Thus, we evaluated these effects in this work.

3.2.4 Validation and efficiency evaluation

We evaluated our implemented VRTs by several voxels at representative locations because the simulation of a full system matrix was computational expensive and was not the main purpose of this work. The results were compared with a baseline analog calculation (hereafter referred as the baseline), where the primary positron was fully tracked until annihilation (either at rest or in flight). The photon range rejection or *pcut* in EGSnrc was applied for photons with energy below 10 keV and the secondary electrons were not simulated [Wernick and Aarsvold, 2004]. The Rayleigh scattering and bounded Compton scattering were both active. The baseline simulation contained 50 million decays. To evaluate the precision and

the efficiency of the proposed VRTs, the baseline simulation was compared with calculations progressively incorporating different VRTs.

To validate the proposed VRTs, PSFs of a voxel source at the center and the edge (25 cm off-center) of the FOV were simulated. The simulation with all VRTs active (hereafter referred as the VRT simulation) was compared to the PSFs derived from the baseline. The number of decays in the VRT simulation was 2.5 million in the central voxel and 250 million in the off-center voxel, respectively. Each positron history was reused 20 times in both simulations, which equal to 50 million and 5 billion decays, respectively. The polar angle was biased to 75° - 105°. The *pcut* was 50 keV; Rayleigh scattering and bounded Compton scattering were both inactive. To compensate for the bias caused by polar angle biasing in the VRT simulation, the number of decays in the baseline was adjusted to 193 million and 20.5 billion. For the voxel at the center of the FOV, the PSF was obtained by summing over all azimuthal angle and slices to increase the effective count by employing inherent symmetries of the scanner. For the voxel at 25 cm off-center, the PSF is obtained from azimuthal angle 154 in a slice with ring combination (15,15). All simulations were launched on a quad-core Xeon platform of 2.50 GHz.

3.3 Results

3.3.1 Validation results

Fig. 3.3 shows the PSFs obtained from the VRT simulation and the baseline simulation for a voxel at the center of the FOV. The VRT simulation slightly underestimates the peak of the PSF compared to the baseline. The FWHMs are 3.64 mm (the VRT simulation) and 3.51 mm (the baseline), respectively; the full width at tenth maximum are 9.05 mm (the VRT simulation) and 8.62 mm (the baseline), respectively. Both differences are less than 5%.

Fig. 3.4 shows the PSFs obtained from the VRT simulation and the baseline for a voxel at the center of the FOV. The FWHMs are 7.37 mm (the VRT simulation) and 7.28 mm (the baseline), respectively; the full width at tenth maximum are 14.9 mm (the VRT simulation) and 14.8 mm (the baseline), respectively. Both differences are less than 1.2%.

3.3.2 Precision and efficiency evaluation

The baseline simulation took 1,241 s and yielded 2,442,797 coincidences. The simulation efficiency is 8.25E5 and precision is 3.13E-5. A summary of the results from employing different VRTs is listed in table 3.1. Detailed results for each VRT will be given item by item.

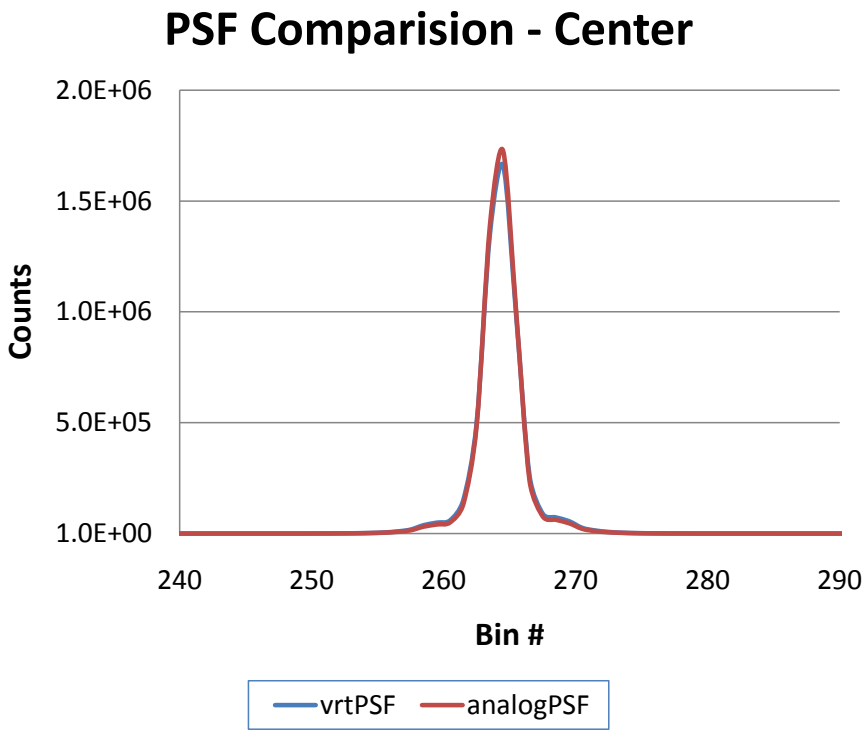

Figure 3.3: Point spread functions of the VRT simulation and the baseline simulation for a voxel source at the center of the FOV.

Techniques	Improvement
Polar angle biasing (75 – 105 °)	2.92
Positron history reuse (25)	4.4
Hit-testing, fictitious transport and forced detection	1.22
Transport para (bounded Compton off)	1.0
Transport para (Rayleigh off)	1.0
Overall (w/o geometry equivalence)	15.3

Table 3.1: Efficiency improvement of different VRTs.

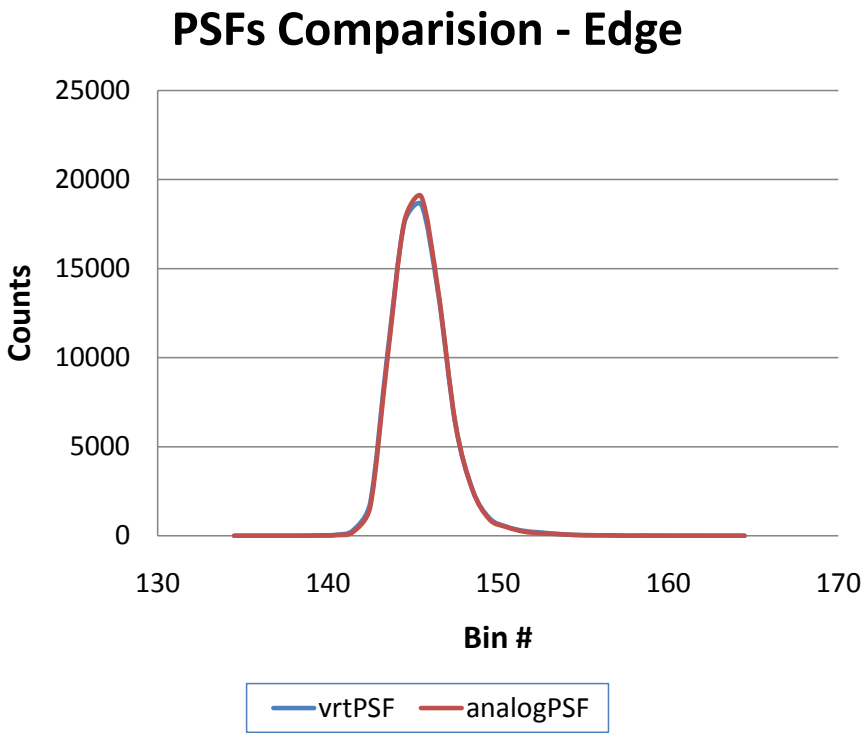

Figure 3.4: Point spread functions of the VRT simulation and the baseline simulation for a voxel source at 25 cm off-center.

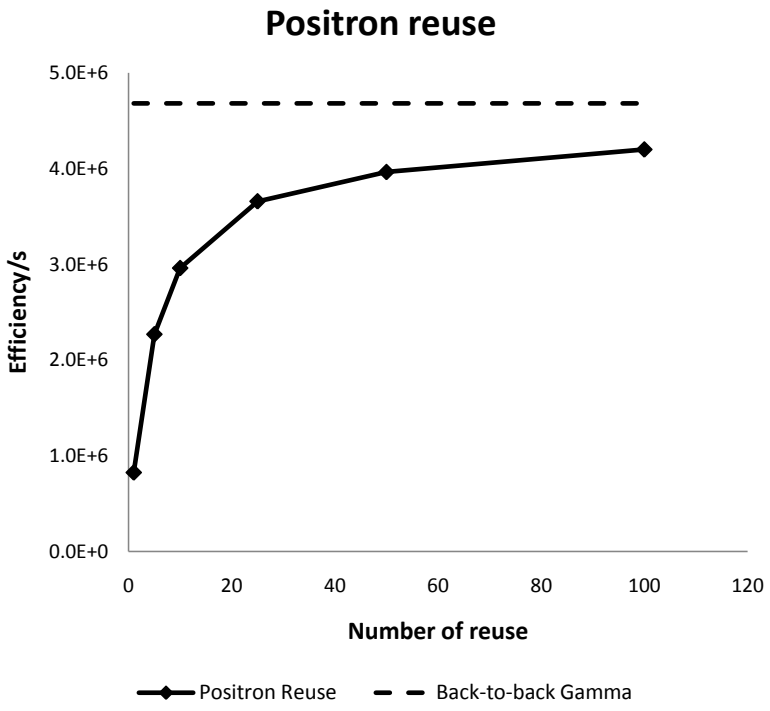

(a)

Figure 3.5: The efficiency was plotted as a function of the number of reuse. The efficiency of a simulation using back-to-back gamma source was also plotted.

Polar angle biasing The simulation using polar angle biasing took 1,600s and produced 9,457,023 coincidences. The simulation efficiency is 2.39E+06, which is improved by a factor of 2.92 compared to the baseline. The precision of simulation with polar angle biasing is 1.59E-05. The precision is improved by a factor of 1.97 compared to the baseline simulation for the same number of simulated events.

Positron history reuse The efficiencies for reusing a positron history for 1 time (the baseline simulation), 5 times, 10 times, 25 times, 50 times, 100 times are plotted as a function of the number of reused in Fig. 3.5. The efficiency of a simulation with back-to-back gamma source and the same configuration is also plotted in this figure. The precision is 3.12E-5 for simulations with positron sources, and is 3.44E-5 for the simulation with a gamma source.

Hit-testing, fictitious transport and forced passing These three techniques were evaluated together. The simulation employing these VRTs took 1,070.7s and produced 2,453,060 $\pm$ 1,513.7 coincidences. The efficiency is 1.01E+06,

which is improved by a factor of 1.22 compared to the baseline simulation. The precision is 3.0e-5, which is improved 4% compared to the baseline simulation for the same number of events simulated.

Transport parameters The execution time of the simulation with *pcut* set to 50 keV was 1,235s and the number of coincidences was 2,440,595. The efficiency is 8.33E5 and the precision is 3.12E-5. When Rayleigh scattering was turned off, the execution lasted for 1,235s and yielded 2,434,774 coincidences. The efficiency is 8.35E5 and the precision is 3.12E-5. When the bounded Compton was turned off, the simulation took 1,236s and produced 2,452,881 coincidences. The efficiency is 8.27E5 and the precision is 3.13E-5. Both the efficiency improvements and precision improvements are negligible.

Overall efficiency improvement The VRT simulation lasted for 374.5s, and yielded 9.45768e+06 $\pm$ 2807.5 coincidences. The efficiency is 1.27E7, which is improved by a factor of 15.2 compared to the baseline. The precision is 1.45E-5, which is improved by a factor of 2.16 compared to the baseline for the same number of simulated events.

3.4 Discussion and future work

The simulation of the system matrix is different from a realistic data acquisition simulation in PET. One such differences is the assumption "time independence". This assumption enables event-based signal processing and coincidence determination logic because randoms are not included to cancel acquisition parameter dependences. In addition, this assumption also enables the positron history reuse technique for the same reason. The assumption of object independence enables the separation of the scattering system matrix and the detector response component. But this simulation setup requires data to be pre-corrected for both photon attenuation and scattering inside the object. This assumption also makes hit-testing and polar angle biasing possible because photon attenuation and photon scattering are not allowed inside the object. The efficiency improvements of different VRTs are correlated, such as the polar angle biasing technique and the hit-testing technique.

The effects of discarding the secondary electrons in the crystals were not evaluated because it has been well-justified [Wernick and Aarsvold, 2004]. Our studies indicated that the 50 keV *pcut*, bounded Compton, and Rayleigh effects are relatively insignificant for both precision and efficiency in resolution modeling.

We used a uniform positron source in a sufficiently large water phantom in our system matrix simulation. The system response obtained by this simulation setup is consistent with the continuous-discrete reconstruction problem [Lewitt and Samuel, 2003]. However, the system response estimated by this method is

equal to the system response of a voxel source in air due to the object independence. This may lead to an under-estimated system response kernel because the system response kernel varies with respect to different activity in the warm background in a physical scanner. In addition, with a "voxel spread function", the partial volume effect cannot be completely compensated. The advantage of this approach lies in its simplicity, which is obtained at the cost of flexibility: once a system model is determined, the voxel size is also determined.

The polar angle biasing and hit-testing techniques improve simulation efficiency by avoiding the transport of photons that are known to miss the detector. Forced detection in SPECT simulation employed the same principle. Implementation of forced detection is more complex because the location- and azimuthal-angle-dependent polar angle complicates the calculation of the solid angle, which may cancel out the gain in simulation efficiency by employing forced detection.

Positron history reuse improves the simulation efficiency because a large fraction of the positrons are tracked but produce no coincidences. Correlations among those detections are introduced in positron history reuse, but these correlations are insignificant because the chances of annihilation photon pairs from the same positron contributing to the same LOR are very small. For example, if 25 annihilation photon pairs share the same positron history, approximately one coincidence is produced on average for the Philips Gemini GS PET scanner with a point source at the center of the FOV. With polar angle biasing, the number of photon pairs for the same positron history can be reduced to avoid such correlation.

The gain from employing the fictitious transport technique is limited in our study. For multilayer detectors such as the jPET-4D scanner [Nishikido et al., 2008], positive gains could be achieved [Tenney et al., 2004]. In the future, more advanced techniques, such as pre-computation of positron distribution [Harrison et al., 1999] and detector responses [Ortuno et al., 2006] [Ortuno et al., 2010] will be investigated.

Accurate photon attenuation and scattering have been investigated for 2-D and 3-D PET reconstruction [Rehfeld and Alber, 2007] [Rehfeld et al., 2010]. However, these methods are constrained by the computational power. Our methods could be candidates to produce an accurate patient-specific system model that meets clinical requirement; the scatter-free SM can be pre-computed by Monte Carlo simulations and the scattering component can be estimated by an SSS or a multiple scattering simulation. However, one limitation is the attenuation correction, which is based on a narrow beam model and is not accurate for PET as its beams are blurry and wide. An accurate modeling of the wide beam effect could improve the image quality. These hypotheses will be investigated in the future. The simulation with all VRTs active show slight under-estimation in the PSF derived from voxel source located at the center and 25 cm off center in the FOV. This under-estimation is acceptable for reconstruction tasks, although the reason is not

clear yet. This will be investigated in the future.

3.5 Conclusion and original contribution

We developed a set of VRTs to use in the SM simulation of PET with egs_pet. For the modeled PET scanner (Philips Gemini GS), the simulation efficiency for a voxel located at the center of the FOV was improved by a factor of 14 for a voxel located at the center of the FOV compared to the analog simulation. Our method indicates that positron transport can be included in an SM simulation with acceptable simulation efficiency loss (30%). These techniques considerably reduced the cost of SM simulation. These techniques could be used in resolution compensation for small animal PET scanners or non-standard isotopes in whole-body human PET scanners.

As the major original contribution, we proposed following VRTs to the field of SM simulation: polar angle biasing, positron history reuse, fictitious transport in crystals, and transport parameter analysis for a PET scanner. These simple VRTs improved the simulation efficiency considerably. This work will be submitted to an A1 journal [Zhang et al., 2010b].

Chapter 4

Resolution Modeling using Cubic Voxels

In this chapter, we will discuss the simulation and reconstruction techniques we developed to meet the computational requirements in Monte Carlo-based resolution modeling using voxels as the basis functions.

4.1 Introduction

As mentioned in Chapter 2, Monte Carlo-based resolution modeling has been demonstrated as an effective method in image quality improvement when used in an iterative reconstruction algorithm in PET reconstruction [Johnson et al., 1995, Shokouhi et al., 2004, Qi et al., 1998, Rannou and Chatziioannou, 2004, Rafecas et al., 2004b, Herraiz et al., 2006, Mora and Rafecas, 2006, Ansorge, 2007, Leroux et al., 2007a]. However, the computational load to calculate the SM and the memory capacity to store the SM (hereafter referred to as the two problems) have limited the use of these methods for state-of-the-art whole-body PET scanners [Buvat and Lazaro, 2006, Panin et al., 2006a]. To address these problems, many methods have been proposed with voxels as the basis functions [Johnson et al., 1995, Rafecas et al., 2004b]. Alternative basis functions have also been used to utilize the inherent symmetries of a PET scanner [Mora and Rafecas, 2006, Ansorge, 2007, Leroux et al., 2007a, Vandenberghe et al., 2006].

In this chapter, we focus on a framework of methods that uses voxels as the basis functions. Symmetries have been utilized to reduce the redundancy in the SM and the simulation cost [Johnson et al., 1995, Rafecas et al., 2004b]. One limitation of these approaches is the limited in-plane symmetries, whose maximum is four-fold. This number is much less than the available in-plane symmetries in a typical PET scanner. For this reason, non-exact approaches, i.e.,

"quasi-symmetry" [Herraiz et al., 2006] and approximate rotational symmetry or azimuthal independence [Qi et al., 1998] [Panin et al., 2006a], have also been proposed for voxel-based image parameterization. A more efficient and accurate method uses a factored matrix to reduce memory requirements and simulation costs in Monte Carlo-based resolution modeling [Qi et al., 1998, Rahmim et al., 2008], but this method is usually slow as accessing an SM element involves on-the-fly calculation in addition to symmetry handling.

We propose a rotator-based approach to solve both the problems simultaneously. This method enables the simulation of a fast, realistic and physically accurate SM for cylindrical whole-body PET scanners. This obtained matrix can be stored in the main memory of a personal computer. Fast reconstruction can be obtained with multi-CPU desktop systems. The first component is the fast SM simulation module, which is based on egs_pet [Kawrakow et al., 2008c] and optimized for SM simulation. This PET simulator provides the same simulation accuracy for this application as Geant4 Application for Emission Tomography (GATE) [Jan et al., 2004] but is, 15–130 times faster [Kawrakow et al., 2008c]. The second constituent is the transformation of the Monte Carlo simulation output into an SM with redundancies reduced by exploiting symmetries of the scanner. This matrix is stored in a highly efficient sparse matrix storage format. The final component is a rotator-based ordered subset expectation maximization (OS-EM) algorithm [Shepp and Vardi, 1982, Hudson and Larkin, 1994]. This algorithm uses as input the line of response (LOR) histogram [Kadrmas, 2004, Moehrs et al., 2008a]. The rotator retains voxels as the object model, which is simple and consistent with the continuous-discrete model of the computed image reconstruction problem. In addition, this basis facilitates a measured system model using a scanning point source.

In addition to utilizing symmetries (referred as "geometry equivalence" in Monte Carlo simulations), the SM simulation can be further accelerated by a light-weight, dedicated, fast and yet realistic Monte Carlo simulators [Shokouhi et al., 2004] with different variance reduction techniques e.g., importance sampling, forced detection [Rafecas et al., 2004b, Shokouhi et al., 2004]. More details about variance reduction techniques in resolution modeling can be found in Chapter 3.

4.2 Materials and Methods

4.2.1 Imaging geometry

The SM was simulated for the Philips Gemini GS PET scanner. The scanner is equipped with GSO crystals of 4.0 mm $\times$ 6.0 mm $\times$ 20 mm in the tangential, axial and radial directions, respectively. These crystals are arranged into 22 $\times$ 29

Transverse FOV	576×576 mm^2
Axial FOV	183 mm
Detectors/ring	616
Number of blocks	28
Number of rings	29
Maximum ring difference	28

Table 4.1: Philips Gemini GS PET/CT Characteristics

LORs per angle	527
Number of angles	308
Number of ring combinations	841
LOR histogram dimension	841×308×527
Voxel size, mm^3	2×2×3.15
Object size, voxels	288×288×58
SM dimension	6.567×10^{14}
Storage SM (Tb)	2,389

Table 4.2: Image volume and LOR histogram configuration

arrays (tangential and axial directions) in 28 flat panels, which form 29 rings with 616 crystals per ring [Lamare et al., 2006, Surti and Karp, 2004]. The whole-body field of view (FOV) is 576×576 mm^2 trans-axially by 183 mm axially [Surti and Karp, 2004]. Table 4.1 lists the characteristics of this scanner. The object volume and LOR histogram settings of the target system are shown in Table 4.2. The dimension of the SM is 6.6×10^{14} and the storage requirement of the whole matrix is estimated to be 2,389 Tb if each SM element were represented by a single precision floating point data type (Table 4.2).

4.2.2 System matrix simulation

4.2.2.1 Simulation setup

The SM calculation used EGSnrc-based code egs_pet, which was reported to be 15 to 130 times faster than GATE [Kawrakow et al., 2008c]. The same principle as described in Chapter 3 such as time independence and object independence, was used to calculate the SM. A uniform cylindrical source (30 cm radius and 20 cm height) of ^{18}F was used to simulate the SM. The source was placed in the center of a water phantom, which had a cylindrical shape, but which was 3 cm larger in radius and 6 cm larger in height. This arrangement allowed a sufficient

positron range. No VRTs (including those described in Chapter 3) were employed in this study because the system matrix quality index in section 4.2.2.3 requires justification.

4.2.2.2 Symmetry handling

Considering the cylindrical shape of the target system, the geometrical symmetries can be exploited for variance reduction [Bielajew and Rogers, 2010]. Two types of equivalent geometries exist in the scanner: axial symmetries and in-plane symmetries. Axial symmetries, i.e., the reflection symmetry (reduction factor 2) and the parallel chord translational symmetry for LORs with a common ring difference (reduction factor: $N_{\mathrm{R}} - R_{\mathrm{d}}$, N_{R} number of rings, R_{d} ring difference), can be utilized assuming identical detector rings and choosing the voxel size in the axial direction to be an integer fraction of the ring pitch [Johnson et al., 1995], i.e., 2 in this chapter. In reality, less translational symmetry could be employed due to border effects of a detector block. Under the reflection symmetry, the z index of a voxel is mirrored to $2(R_1 + R_2) - z + 1$, where R_1 and R_2 are the two rings (top in Fig. 4.1a). With respect to the translational symmetry, the z index of a voxel is shifted by $2\Delta R$ if the two LORs are separated by ΔR rings (bottom in Fig. 4.1a).

In-plane symmetries include the rotational symmetry and in-plane mirror symmetry. Because the scanner consists of 28 blocks, equally spaced on a ring, rotational symmetry is achieved by rotating the image grids to these positions, as illustrated in Fig. 4.1b. A voxel in the rotated grid (in black) has the same contribution to a rotated LOR as the corresponding voxel in the original grid (in grey) to the original (non-rotated) LOR. We chose to rotate the image over π, leading to a reduction factor of 14. In addition, there exists 2-fold in-plane mirror symmetry when the block edge effects were modeled, as illustrated in Fig.4.2b. LORs of the two view angles are equivalent under a mirror operation. We did not exploit this symmetry in present study. In contrast, traditional methods use 4-fold in-plane symmetry for the same configuration.

To use the translational symmetry, correct sensitivity must be maintained because this symmetry is ring difference-dependent. The maximum ring difference was chosen to be 14, leading to 15 translational symmetries for all selected LORs. We reduced the number of translational symmetries to 11 to exclude LORs with a ring difference greater than 14 (e.g. ring 0 and ring 28), which have different system responses than LORs in the center (detector border effects).

4.2.2.3 System matrix quality index

Because there exists a trade-off between simulation time and image quality, different indices have been proposed to evaluate the precision of a calculated SM. Basic empirical indices consider only the voxel size or the sensitivity of a LOR.

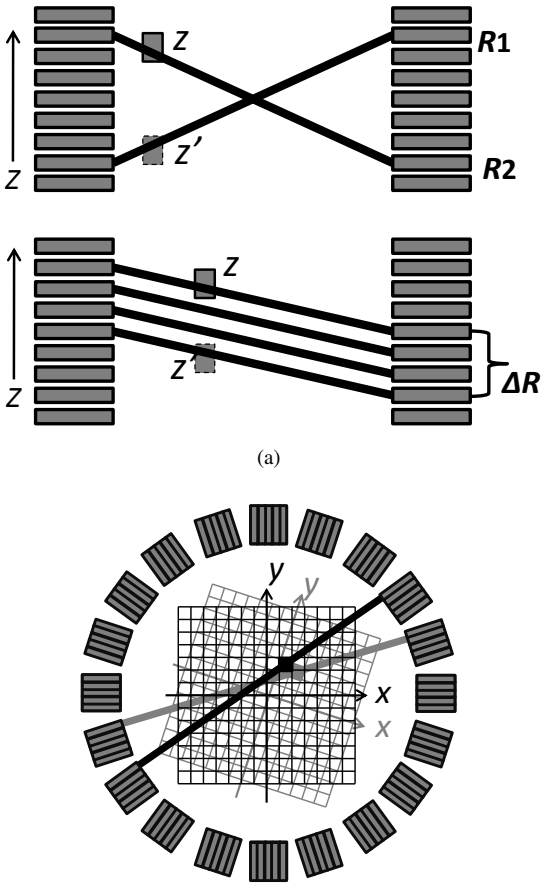

Figure 4.1: (NOT TO SCALE) Symmetries. (a) Axial symmetry. SM elements associated with crossed LORs are interchangeable under a mirror operation. SM elements associated with LORs in parallel are identical. (b) Rotational symmetry. The two SM elements are identical given detector blocks are identical.

The number of events in one voxel and detections of a LOR are used as the figures of merit (e.g. 50 million events per voxel [Shokouhi et al., 2004], 10 detections per LOR [Leroux et al., 2007b]). More advanced indices include the effects of both the voxel size and the LOR sensitivity and use statistical properties of the SM as an index, such as mean and "mean relative error" [Rafecas et al., 2004b]. A theoretical approach characterizes the effect of the variance/error in the SM on the accuracy in reconstructed images and concludes that the artifacts caused by the noisy SM should be insignificant compared to these of data [Qi and Huesman, 2005]. This

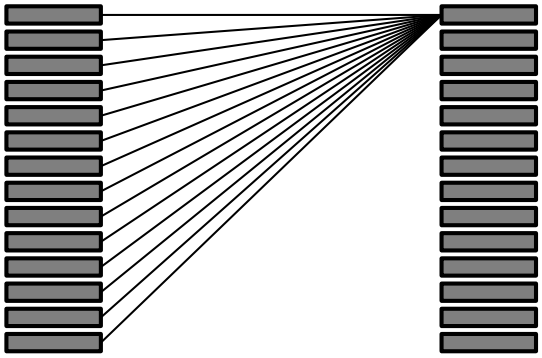

(a)

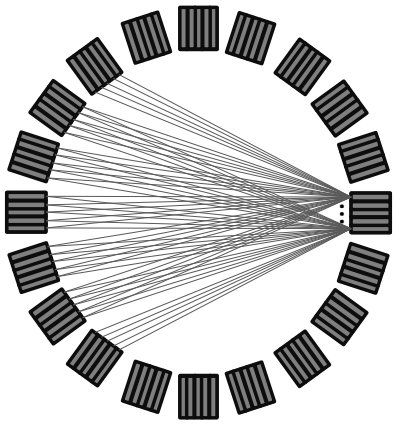

(b)

Figure 4.2: (NOT TO SCALE) The base-symmetry LORs. (a) Axial base-symmetry LORs. (b) In plane base-symmetry LORs (Only two views were drawn for clarity).

introduces study-dependent factors into the evaluation of a SM, which reveal the fact that the precision of a SM also depends on the involved study. However, none of the above indices cover all aspects of the problem. Therefore, we propose the following index:

$$N_{sim} \geq \frac{1}{\alpha} M_{mea}, \tag{4.1}$$

where N_{sim} is the total number of events required to simulate the SM, M_{mea} is the total number of emissions in the data and α is a constant to balance the simulation cost and the image quality to ensure that the error caused by the SM in

the reconstructed image is α times the error caused by the data [Qi and Huesman, 2005]. A reference α value of 0.01 was suggested. This index is "image quality aware" because it quantifies the image error caused by the statistical quality of the SM.

Equation 4.1 can be used in a more practical way:

$$k = \frac{N_{sim} \cdot \max(\mathbf{A})}{\max(\mathbf{y})}, \tag{4.2}$$

where $max(\cdot)$ represents the maximum operator (only non-zero elements are considered), $\mathbf{y}$ refers to the measured data vector, k is a constant to balance the simulation time and image quality, $\mathbf{A}$ is the noisy SM (in absolute probability).

4.2.3 System matrix storage

The SM is very sparse (a large portion of elements are zero) and redundant (a large portion of elements are identical) [Rafecas et al., 2004b]. Thus, a sparse matrix storage format was used to reduce the storage requirement. The LOR index was reused by all SM elements associated with it, and the voxel index was encoded with the SM element value in a four-byte word, resulting in a highly compact and direct access scheme. Time-consuming techniques, such as automated indexing [Qi et al., 1998], were avoided. Redundancy in the obtained SM was reduced by using LOR symmetries. Only a subset of SM elements was stored and the rest could be obtained by either in-plane symmetry or axial symmetry. This subset, called the base-symmetry SM, contained elements associated with the base-symmetry LORs. The base-symmetry LORs contained 29 ring combinations (one for each ring difference), each with 22 view angles of 527 LORs, as illustrated in Fig. 4.2. The maximum ring difference was chosen to be 14, resulting in an extra reduction factor of 1.93 ($\frac{29}{15}$) in SM storage at the cost of about 25% sensitivity loss. The base-symmetry SM was stored in the aforementioned sparse matrix storage format. Elements in the base-symmetry SM whose values are less than 0.5% of the maximum were removed from the SM [Rafecas et al., 2004a,Leroux et al., 2007b].

4.2.4 The rotator-based OS-EM

The rotator-based maximum likelihood expectation maximization (ML-EM) was first used in Single Photon Emission Computed Tomography (SPECT) reconstruction [Frey et al., 1993, Zeng et al., 1994b]. This method has been introduced into PET to exploit redundancy in the SM [Kadrmas, 2004, Moehrs et al., 2008b]. In this article, a Gaussian rotator with a 1 pixel full-width-at-half-maximum (FWHM) and a 3×3-pixel kernel [Wallis and Miller, 1997] was used in an OS-EM algorithm. A sub-iteration of the rotator-based OS-EM can be expressed as:

$$f_j^{K,S+1} = \frac{f_j^{K,S}}{Sen_j^S} \sum_r R_r^T \left(\sum_{i \in S} \tilde{a}_{l,j} \frac{g_i}{\sum_j \tilde{a}_{l,j} \left[R_r \left(f^{K,S} \right) \right]_j} \right) \tag{4.3}$$

where f is the image volume, K is the iteration number, S refers to a subset, $\tilde{a}_{l,j}$ is the base-symmetry SM, i is the LOR number, which organized as $i = r \times N_{sm} + l$, N_{sm} is the LOR dimension of the base-symmetry SM, r is the rotational symmetry number, which can be calculated as $r = i/N_{sm}$, $l = i \, mod \, N_{sm}$ is the LOR index of the base-symmetry SM, g is the measurement, R and R^T are the rotation operators, and Sen is the sensitivity term, which can be expressed as:

$$Sen_j^S = \sum_r R_r^T \left(\sum_{l \in S} \tilde{a}_{l,j} \right)_j \tag{4.4}$$

In this chapter, the ordered-subset level was chosen to be 22, which corresponds to the number of angles of a ring combination in the base-symmetry SM. Consequently, a subset contains 14 angles, corresponding to the number of rotational symmetry.

4.2.5 Image quality evaluation

The contrast recovery coefficient (CRC) and noise level calculated on regions of interest were used as figures of merit. Regions of interest were defined for cold lesions, hot lesions and the background. The CRC of a hot lesion is expressed as:

$$CRC(\%) = \frac{1}{CZ} \sum_{z=1}^{Z} \frac{\bar{\mu}_{h,z}}{\bar{\mu}_{b,z}} \times 100 \tag{4.5}$$

where z is the realization number and Z the total number of realizations. $\bar{\mu}_{h,z}$ is the mean of the reconstructed activity in a hot lesion h of a realization z, $\bar{\mu}_{b,z}$ refers to that in the background of a realization z and C is the true hot-to-background contrast.

The CRC of a cold lesion is defined as:

$$CRC(\%) = \frac{1}{Z} \sum_{z=1}^{Z} \frac{\bar{\mu}_{b,z} - \bar{\mu}_{l,z}}{\bar{\mu}_{b,z}} \times 100 \tag{4.6}$$

where $\bar{\mu}_{l,z}$ is the mean of the reconstructed activity in a cold lesion l of a realization z.

The noise level σ_{n} is denoted as:

$$\sigma_{\mathrm{n}}(\%) = \frac{1}{B\bar{\mu}_b} \sum_{b=1}^{B} \bar{\sigma}_b \times 100 \tag{4.7}$$

where B is the total number of pixels in the background, $\bar{\mu}_b$ is the mean of the reconstructed activity in the background of different realizations, σ_b is the standard deviation of the reconstructed activities within a pixel b of different realizations. For a single realization, i.e., the measurement study, the noise was calculated as the relative standard deviation in the background.

4.2.6 Simulation study

A customized image quality phantom filled with ^{18}F-FDG in water was simulated to characterize the contrast noise trade-offs. It consisted of four hot spheres (9.89, 12.43, 15.43, 19.79 mm diameter) with a contrast to background ratio of 4:1, and two cold spheres (25.4, 31.8 mm diameter) located at the central plane. The background was a cylinder of 204 mm in diameter and 150 mm in height. The cylinder was filled with water as annihilation medium, but photon attenuation and scattering were disabled in the simulations within this cylinder. A total of 50 realizations were simulated, with 5,500 million disintegrations each. Scatters and randoms were directly rejected during simulation, resulting in a collection of 200 million true coincidences per realization.

The simulated data were reconstructed using the LOR-based OS-EM and the simulated SM. Contrast and noise properties were evaluated with the figures of merit described in Section 6.3.3. The results were compared to those of a standard OS-EM using a multi-ray Siddon projector [Verhaeghe et al., 2008]. The crystals were assumed to be a 2-D pixelized black body. We tracked five rays on-the-fly per LOR, each end point location was randomized within the crystal.

4.2.7 Measurement study

A Deluxe Jaszczak Phantom (Data Spectrum Corporation, Hillsborough, NC, USA) filled with 1 mCi ^{18}F-FDG in water was imaged on the Gemini GS PET/CT scanner. The phantom consisted of six spheres and an ultra deluxe cold rod insert. The spheres included four hot spheres (9.89, 12.43, 15.43, 19.79 mm diameter) and two cold spheres (25.4 and 31.8 mm diameter). The cold insert consisted of six wedges of cold rods (3.2, 4.8, 6.4, 7.9, 9.5 and 11.1 mm diameter). The hot-to-background ratio was 4:1.

The phantom was scanned for 40 minutes in fully 3-D mode. About 250 million coincidences (after subtracting randoms) were collected and binned into an LOR histogram [Kadrmas, 2004]. Normalization was applied onto the LOR histogram using an iterative model-based method [Ferreira et al., 2000]. The attenuation map was obtained from the CT scan. Scatter correction was applied by a single scatter correction technique [Watson et al., 1997]. Finally, the preprocessed data were reconstructed using the MCSM method. The same data set was also reconstructed on 2 mm $\times$ 2 mm $\times$ 2 mm grids by the blob-based Row-Action Maximum

Indices	MCSM	Reference
Events/voxel	54.9 million	50 million or 100 million [Shokouhi et al., 2004]
Detections/LOR	$4.7 \cdot 10^4$	10 [Leroux et al., 2007b]
Theoretical analysis (simulation)	$4.5 \cdot 10^4$	100 [Qi and Huesman, 2005]
Theoretical analysis (measurement)	10^4	100 [Qi and Huesman, 2005]
SM mean	14.1	3.06 [Rafecas et al., 2004b]

Table 4.3: Relationship with other indices

Likelihood Algorithm (RAMLA) equipped on the scanner using routine parameter settings in brain mode, where neither span nor mashing was applied [Surti and Karp, 2004]. This algorithm calculates on-the-fly the length of intersection with blobs as the system model [Lewitt, 1992]. All corrections were applied using the standard tools equipped on the scanner prior to reconstruction.

4.3 Results

4.3.1 System matrix quality index

The SM was built from $2.1 \cdot 10^{10}$ coincidences. The statistics of the obtained SM are equivalent to those of an SM derived from a simulation with $6.4 \cdot 10^{12}$ detections without exploiting symmetries. This simulation contained $2.5 \cdot 10^{14}$ events as the simulated sensitivity was about 2.6% by using the aforementioned simulation setup (section 4.2.2). The average number of detections per LOR was $4.7 \cdot 10^4$. The number of events per voxel was 54.9 million. The average of all non-zero elements in the obtained base-symmetry SM was 14.1 after applying the threshold defined in section 4.2.3.

The data were simulated from $5.5 \cdot 10^9$ events, resulting in a $1/\alpha$ of $4.5 \cdot 10^4$. This quantity of the measurement study was assumed to be of the same order of magnitude (10^4) as the simulation study. The exact number was unknown however [1]. These figures are summarized and compared to the other indices (table 4.3).

[1] In terms of system modeling, we were only interested in events that contributed to the detector response.

egs_pet	15.8 [2]
Efficiency improvement techniques	1.2
Rotational symmetry	14
Translational symmetry (axial)	11
Reflection symmetry (axial)	2
Total	5,839.7

Table 4.4: Simulation efficiency improvement

Max ring diff 14	1.93 ($\frac{29}{15}$)
Rotational symmetry	14
Translational and reflection symmetry	29
Total	791.7

Table 4.5: Storage reduction factors

4.3.2 Calculation time

The SM simulation took approximately five days on a cluster with 50 Intel Xeon 2.66Ghz cores. The factors that contributed to the simulation efficiency improvement are listed in table 4.4. Egs_pet was 15.8 times more efficient than GATE for this particular application without the use of variance reduction techniques. The efficiency was further improved by 23% with the fast signal processing chain and code optimization. The total acceleration factor was 5,840.

This SM was then integrated within the rotator-based OS-EM algorithm. The reconstruction of the measurement data in section 4.2.7 took 2,450 seconds per iteration on a single CPU core of an Intel Core 2 Duo 2.53 GHz. This code was not yet fully optimized for speed. Many optimization strategies, i.e., parallelism, smart symmetry handling and access order optimization, could be used to further reduce reconstruction time. The reconstruction of the same data with the multi-ray Siddon projector algorithm, also using 22 subsets, lasted 1,550 seconds per iteration on the same CPU core.

4.3.3 Storage of the system matrix

The number of non-zero SM elements was $5.4 \cdot 10^8$, resulting in an SM sparsity of 99.94%. The size of the SM was therefore approximately 2.01 GB. Table 4.5 summarizes the results of the different storage reduction techniques. The total memory requirement was reduced by a factor of approximately 790.

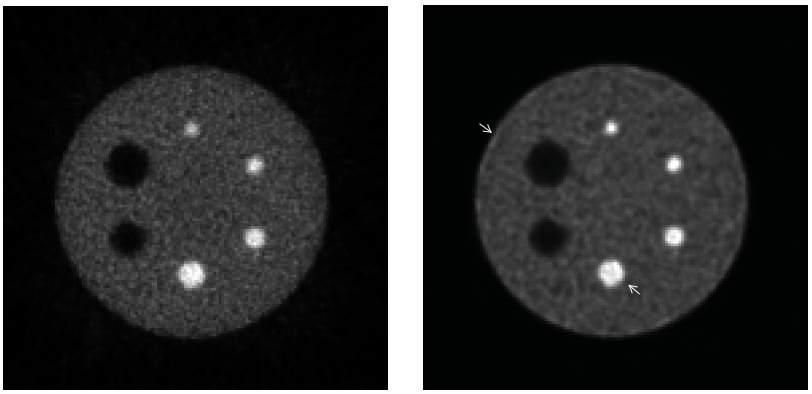

(a) (b)

Figure 4.3: Reconstruction examples. (a) Multi-ray Siddon projector method (iter 4, 22 subsets). (b) MCSM method (iter 4, 22 subsets). Ringing artifacts indicated by white arrows.

4.3.4 Image quality evaluation

4.3.4.1 Simulation study

Slices of the Jaszczak phantom reconstructed with the Siddon OS-EM and the MCSM method algorithm are shown in Fig. 4.3a and Fig. 4.3b respectively. Both slices are illustrated at iteration 4 of OS-EM with 22 subsets and at 50% FOV. Visual inspection revealed that our method led to smoother and sharper images. However, noticeable ringing artifacts were detected along the edge of the background and of the largest hot lesion, indicated by white arrows.

The contrast recovery versus noise curves are plotted both for our method and for the Siddon OS-EM algorithm in Fig. 4.4. Error bars are derived from 50 different realizations.

4.3.4.2 Measurement study

Reconstructed slices of the Deluxe Jaszczak phantom are shown in Fig. 4.5a (spheres) and Fig. 4.5b (cold rods) for the blob-based RAMLA. The same slices reconstructed with the MCSM method are illustrated in Fig. 4.5c (spheres) and Fig. 4.5d (cold rods). The ringing artifacts are undetectable in Fig. 4.5c and the cold rods in Fig. 4.5d are visually sharper. This was confirmed by the profile through one row of the 11.1- and 7.9-mm diameter rods, depicted in Fig. 4.6. In Fig. 4.7a the CRC versus noise of the hot lesions is plotted for both reconstruction methods and in Fig. 4.7b for the cold lesions.

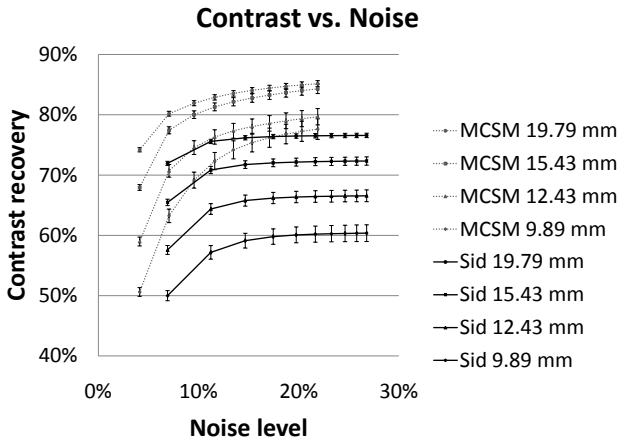

(a)

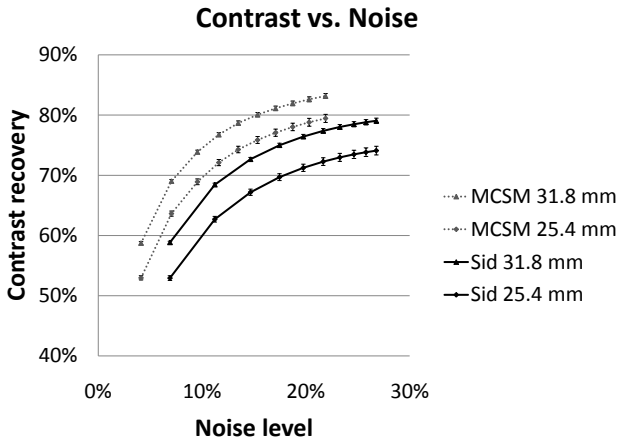

(b)

Figure 4.4: Contrast versus noise curves of the simulation study, each point represents one OS-EM iteration with 22 subsets. (a) Contrast-noise curve for hot lesions (b) Contrast-noise curve for cold lesions.

4.4 Discussion

The variance of an SM element estimation decreases as $1/N$, which is consistent with the theoretical analysis [Qi and Huesman, 2005]. Thus, the achieved efficiency improvement can be estimated by the factor of increased number of events simulated for the same computational power. Exploiting symmetries of the PET scanner attributes to the largest fraction in both the storage reduction (factor 406 = 29x14) and simulation efficiency improvement (factor 308 = 11x2x14). The

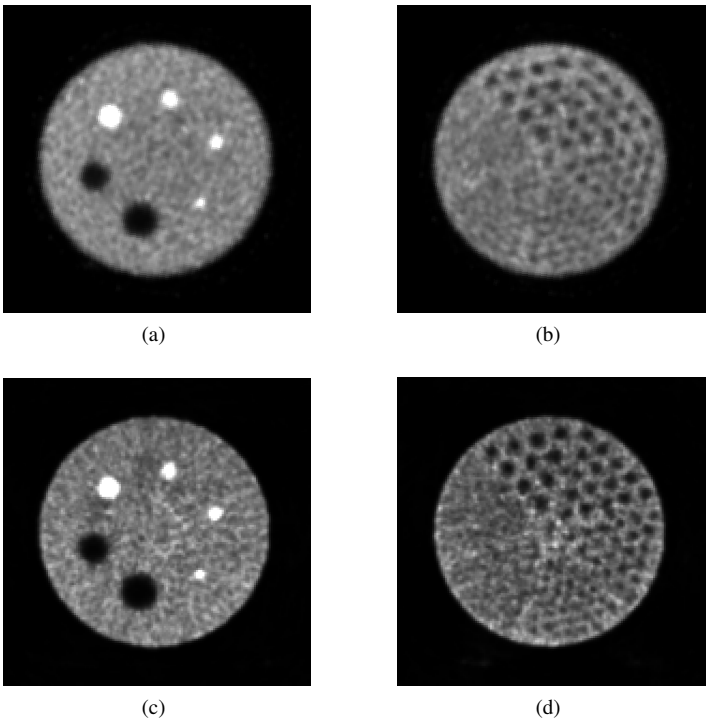

Figure 4.5: Reconstruction examples. (a) The spheres of the clinical software. (b) Cold rods of the clinical software. (c) The spheres of the MCSM method. (b) Cold rods of the MCSM method.

rotator-based algorithm provides a maximum in-plane symmetry of 28 (14 rotational symmetry and two mirror symmetry) for both simulation and SM storage with the same axial symmetries on a cuboid voxel discretization [3]. The conventional methods provide at most four in-plane symmetries for the same configuration. More rotational symmetries may be exploited for a PET system with an ideal cylindrical shape in our method. The light-weight simulator egs_pet contributes an additional factor of 16 in efficiency improvement. The timing independent simulation provides an extra 20% speed-up.

The acolinearity of the annihilation photon was not modeled because this effect is not included in EGSnrc [Kawrakow and Rogers, 2007]. However, this effect has little impact on simulation efficiency and the storage requirement of the SM [Harrison et al., 1999]. We also investigated SM simulation and reconstruction using a back-to-back gamma source for ^{18}F studies. The simulation time was reduced by a factor of four compared to a positron source simulation. The reconstruction re-

[3] the two-fold in-plane mirror symmetry was not employed.

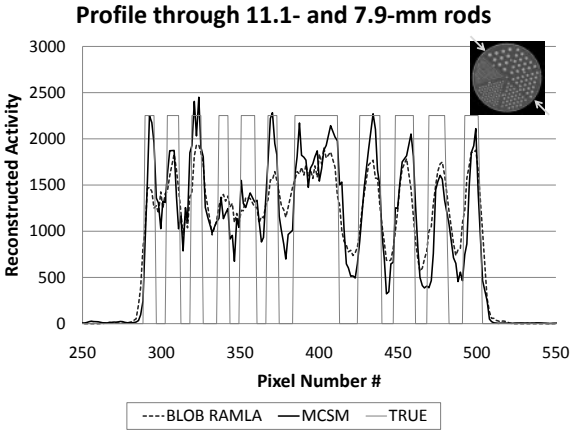

Figure 4.6: Profile extracted through 11.1- and 7.9-mm cold rods.

sults indicated that positron range could be skipped without compromising image quality for the target system and proposed algorithm. The same conclusion could be expected when the acolinearity is included in the system modeling. However, system modeling without positron range may not be appropriate for small animal PET scanners, where the positron range matters.

The working SM comfortably meets the suggested lower limit criteria reported in the literature [Shokouhi et al., 2004, Rafecas et al., 2004b, Qi and Huesman, 2005, Leroux et al., 2007b], as summarized in the right column of Table 4.3. The error caused by the SM in the reconstructed image could be ignored by using the theoretical analysis by Qi *et al.* [Qi and Huesman, 2005]. Ring artifacts due to exploiting symmetries were avoided by simulating more than ten detections per LOR [Leroux et al., 2007b]. However, significant contrast loss had been detected when the same data were reconstructed by a low statistics SM, which contains half of the detection as the working SM. This indicates that more detections are needed to build a more accurate SM.

Quantitative accuracy, in terms of contrast recovery (bias), was significantly improved compared to the multi-ray Siddon projector algorithm and the blob-based RAMLA algorithm. The improvement in cold spheres contrast was more pronounced with respect to the blob-based RAMLA. The blob-based RAMLA showed better noise properties because a blob radius of 2.5 pixels was used in clinical settings [Surti and Karp, 2004], which regularized the image to be smooth. Studies have shown that the blob object model was equivalent to an after-backprojection-filter using the same blob function [Zhang and Zeng, 2006].

Ringing artifacts were detected in the simulated phantom studies. We investigated the origin of ringing artifacts using an "ideal" rotator based on polar-pixels,

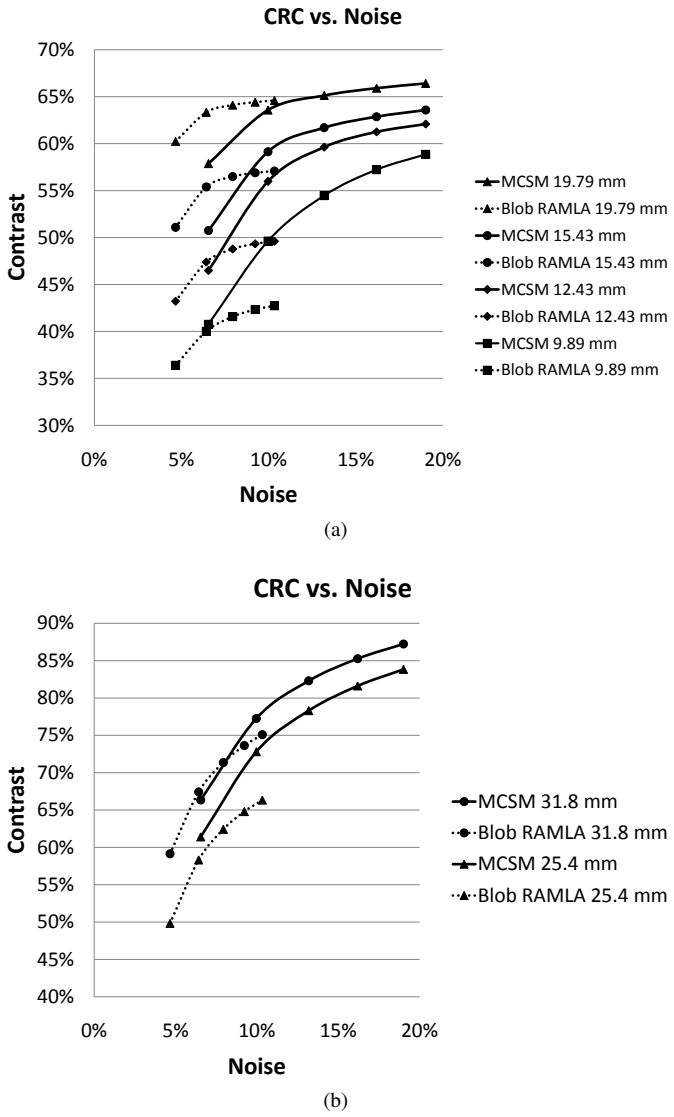

Figure 4.7: Contrast noise trade-offs of the measured data, each point represents a single iteration. (a) Hot lesions. (b) Cold lesions.

which provides perfectly rotated image without any blurring or distortion in chapter 6. The study indicates that the artifacts could be mainly attributed to the rotator because it causes blurring in image space [Wallis and Miller, 1997], which further blurs the system response kernel (Fig. 4.8). Similar results were reported in the reconstruction using an over-blurred system response kernel (i.e. wider kernel) in

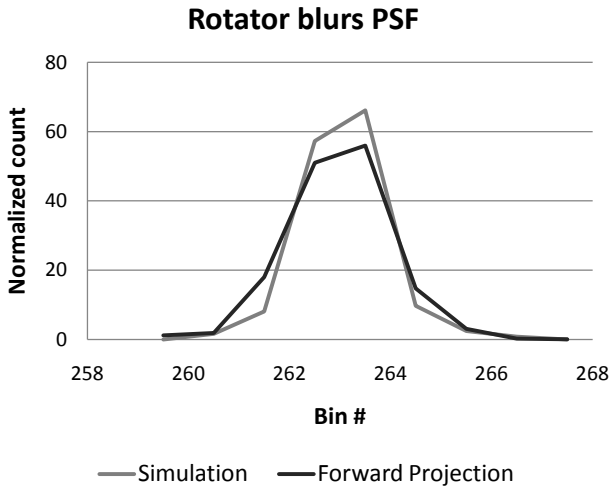

(a)

Figure 4.8: The Gaussian rotator blurs the PSF obtained by simulation.

image space [Reader et al., 2003, Sureau et al., 2008].

However, ringing artifacts were barely detected in the measurement studies, indicating an absence of over-blurred system responses. The absence of the acolinearity of annihilation photons in egs_pet contributes to this under-estimation of the width of the PSF [Kawrakow and Rogers, 2007]. Factors that are not included in the scanner model, i.e., optical photon transportation and detector electronics, may also contribute to this effect [Lamare et al., 2006]. Our SM simulation is equivalent to a simulation with a voxel source in air because no photon-matter interactions were simulated in the water phantom. This method yields sharper system response function compared to the voxel in a warm background. In addition, non-perfect correction techniques (randoms, scatters and normalization) might contribute to the artifact reduction as the residual errors might introduce bias, boost noise or expand the blurring of system responses (i.e., randoms and scatters).

In contrast to a radial symmetry object model, we used a rotator to exploit the rotational symmetry of the LORs. This method retains the cuboid voxel discretization, which is simple and conforms to the discrete-to-discrete model of image reconstruction [Lewitt and Samuel, 2003]. In addition, retaining cuboid voxels facilitates a measured system model using a scanning point source. However, the use of a rotator compromises the accuracy of the system response function as an ideal rotator does not exist for the voxel discretization [Wallis and Miller, 1997]. The exact effects of this compromise and how it relates to the blurring effects of the positron range require further investigation.

4.5 Conclusions and original contribution

We developed a framework of SM simulation and reconstruction techniques, including a fast, realistic SM simulation module and a rotator-based OS-EM algorithm. This framework allowed exploitation of the rotational symmetry of a cylindrical PET scanner and retention of voxels as the object model. The SM could be efficiently calculated and stored in the main memory of a standard PC. The image quality improved considerably in terms of contrast-noise trade-offs. Image quality was also compared to clinical software using routine parameter settings. The quantitative accuracy of smaller spheres and cold spheres was significantly improved. Our novel method may be used in other cylindrical whole-body and preclinical PET scanners.

The work described in this chapter yields to several conference publications [Kawrakow et al., 2008a] [Zhang et al., 2008] [Zhang, 2008] and one A1 journal publications [Zhang et al., 2010c].

Chapter 5

Experiment-based Resolution Modeling

In this chapter, the initial implementation of a rotator-based method using experiment-based point spread function (PSF) modeling is presented to investigate the potential of the rotator-based reconstruction algorithm.

5.1 Introduction

Employing measurement-derived PSFs in PET reconstruction has been generally regarded as the most accurate approach in resolution compensation [Tohme and Qi, 2009] [Wiant et al., 2010]. One reason lies in its ability to measure effects that are difficult or unfeasible to model in other methods, such as the crystal identification algorithm in an Anger logic detector and optical photon transport [1]. A limitation of this approach is the necessity for intensive scanning, which often takes several minutes per position. Thus, measurement on a complete image grid is unfeasible [Panin et al., 2006b]. This constraint can be addressed with a parameterization technique and a sparse measurement grid. This technique was first applied in SPECT for resolution compensation [Rowe et al., 1993] [Chen et al., 2005] [van der Have et al., 2008]. The unmeasured detector response functions can be estimated from the parameters obtained from the measured points [Panin et al., 2006b] [Wiant et al., 2010] [Tohme and Qi, 2009] [Alessio et al., 2010]. Another constraint of this method is the requirement of storing the obtained system model. Because the measured system matrix is denser than other approaches (such as a Monte Carlo-based approach), storing the pre-computed system matrix in the memory is challenging. Symmetries can reduce the redundancy in the

[1] Although optical photon tracking is possible in GATE, including it in system matrix simulation is highly prohibitive

LORs per angle	589
Number of angles	322
Number of ring combinations	841
LOR histogram dimension	841×322×589
Voxel size, mm^3	2×2×2.1
Object size, voxels	288×288×87

Table 5.1: image volume and LOR histogram configuration

system matrix.

However, for a voxel-based approach, the available symmetries are limited for cylindrical scanners. As we argued in the previous chapter (Chapter 4), a rotator-based approach may reduce the storage cost. Because voxels are used as basis functions, the existing resolution modeling techniques [Panin et al., 2006b, Wiant et al., 2010, Tohme and Qi, 2009, Alessio et al., 2010] using measured data can be directly employed in the rotator-based method because all these techniques used voxels.

In this chapter, we present the initial implementation of the rotator-based method using a factorized matrix approach and PSF modeling, which include both radial and axial blurring effects. We also investigate the contribution of the radial and axial blurring effects to image quality.

5.2 Materials and Methods

5.2.1 The scanner

We used the Philips Gemini GS PET/CT scanner. The technique specification of this scanner can be found in section 4.2.1 of Chapter 4. The scanner was assumed to be a perfect cylinder with a continuous crystal. Thus, the gaps were treated as virtual crystals with no output. In this work, we used different image volume and LOR histogram settings, which are listed in Table 5.1.

5.2.2 PSF measurement

An uncollimated ^{22}Na point source in Lucite was used. Monte Carlo simulation has demonstrated that the positron range of such a configuration is approximately the same as that of ^{18}F in water [Alessio et al., 2010]. The activity of the point source was 40 μCi and the radius was 225 μm. The robot was the Owis LTM80 precision linear stage. It has maximum ranges of 290 mm in the x-, y- and z-direction. We used 260 mm of this range. The positioning error is less than 25

μm per 100 mm of movement. The robot was mounted on an optical table, which had four legs with wheels. Because of the rails at the end of the PET scanner were about 70 cm, we used a long arm to cover half of the axial FOV. The robot and the arm are illustrated in Fig. 5.1.

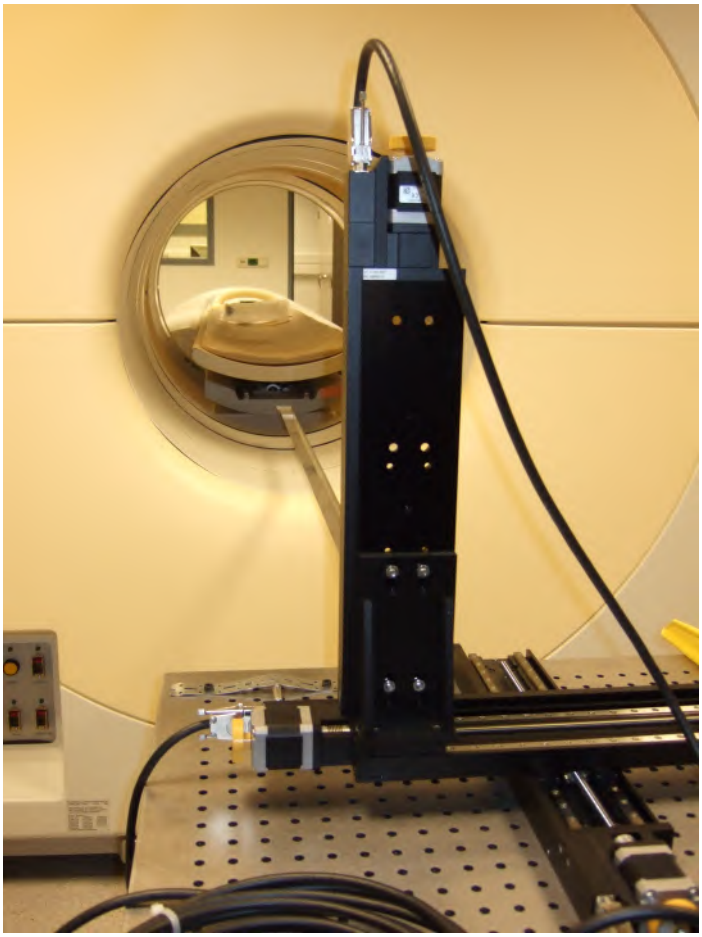

Figure 5.1: The robot

The scanner coordinate system was aligned with the coordinate system of the robot by adjusting the position and height of the legs of the optical table. After each adjustment, the point source centering test utility on the scanner was used to test whether the point source was approximately centered. When the point source passed the centering test program, the point source was scanned at three positions (0 cm,0 cm), (27 cm, 0 cm) and (0 cm, 20 cm) in the central plane to ensure that the frame of the robot was well-aligned with that of the scanner by analyzing the

sinogram.

After the two coordinate frames were well-aligned, the sinogram intensities of the three point sources should have been approximately identical across several direct planes. The positioning precision of this technique was believed to be less than 0.5 mm in the axial direction [Wiant et al., 2010]. To determine the center, we used two criteria: 1) where the count rate is the highest and 2) where the ratios of the sum of the count rate in the central plane to its two neighboring planes were approximately the same. In addition, the sinogram of a point source is a vertical line in the direct central plane if the point source is centered.

Because the measurement is very time-consuming, measuring the entire image grid is not practical [Panin et al., 2006b]. We chose to measure the PSFs on a sparse grid in a small portion of the entire FOV (see Fig. 5.2 and Fig. 5.3). This portion was carefully chosen such that the entire FOV could be covered by using the inherent symmetries of the scanner. The sampling points that share the same z-coordinate was referred as a sampling plane. The spacing between rows and columns in a sampling plane was 10 mm, which was sufficient for robust parameterization [Wiant et al., 2010]. The spacing between two sampling planes was 3.15 mm, which was half of the crystal ring pitch of the scanner. The axial location of each plane was chosen to be symmetric about the center of the associated ring (Fig. 5.3).

The system response kernels were measured at 29 sampling planes, which contained 2,175 locations in the FOV. The point source was scanned for 3 minutes at each location, yielding approximately 15 million coincidences. Because of the long half-life of the isotope ($\approx$2.6 year), its activity was assumed to be constant during the point source acquisition (within one month). The data were acquired in raw list mode and the data volume was about 200 GB.

5.2.3 PSF modeling

The system model should be independent of the specific scanner of the same model [Panin et al., 2006b]. Thus, the data were first normalized using a component-based iterative approach [Wang et al., 2007] to remove any scanner-specific factors (e.g., geometrical misalignment of the crystals in a detector blocks and variations in the gain of PMTs). We assumed that perfect rotational symmetries can be employed. This similarity is usually achievable in modern PET scanners with a small block detector design [Panin et al., 2006b]. We also assumed that the PSFs along the same LOR were approximately identical at different depths. This assumption is also achievable in a block-detector scanner [Panin et al., 2006b].

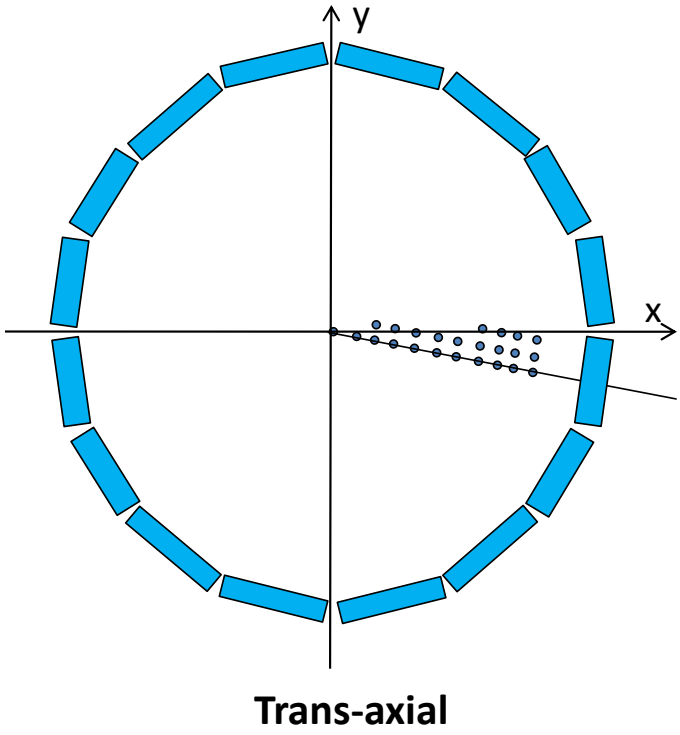

Figure 5.2: The sampling grids in the x-y (transverse) plane. The grid area is slightly larger than the triangle formed by the origin, the middle of the detector block and the middle point of the two adjacent blocks.

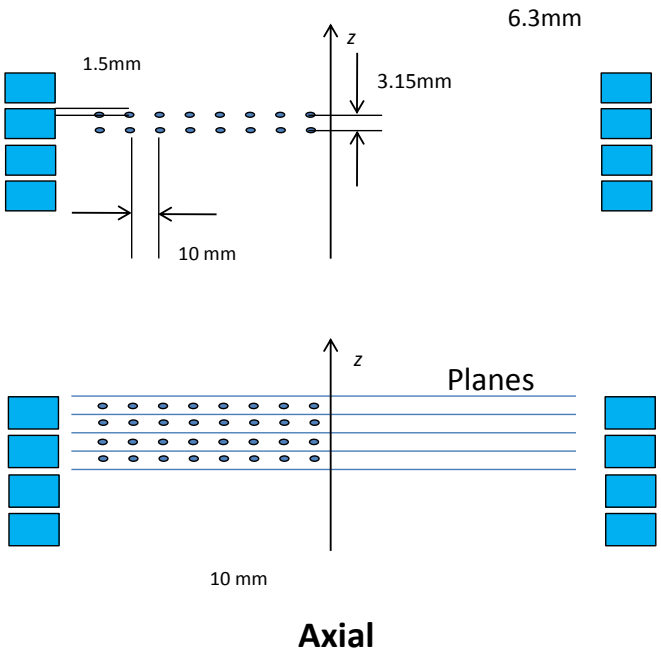

Figure 5.3: Schematic drawing of the sampling grid in the z (axial) direction.

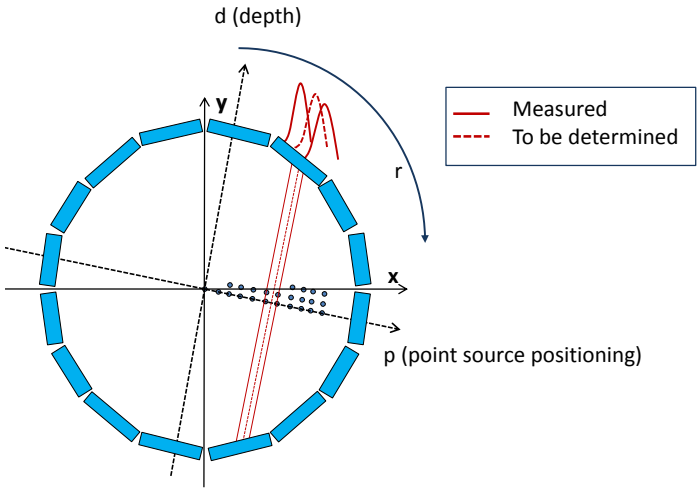

Figure 5.4: The principle of the parameterization-based technique. The unknown PSF (dotted line) is obtained indirectly: the measured PSFs are first parameterized with a proper model. Another model is then fitted to the parameters. The unknown PSFs are finally sampled from the model of the parameters.

5.2.3.1 Radial blurring modeling

Given these assumptions, the measured PSFs at an azimuthal angle (ϕ = 165) were employed to derive the parameters of the radial profiles. A radial PSF profile was modeled as an asymmetric Gaussian function, which is the summation of two Gaussian functions with the same amplitude and peak location. The left and right parts had standard deviations of σ^L and σ^R. The radial profile of a ray is expressed as follows:

$$PSF^{rad}_{slc}(r,p) = A_{slc}(p) \cdot e^{(-\frac{(r - r^0_{slc}(p))^2}{2\sigma^2_{slc}(p)})} \tag{5.1}$$

where slc stands for the index of an LOR histogram slice (LORs that share the same ring pair) and p stands for a point source location, $A_{slc}(p)$ is the amplitude of the asymmetric Gaussian, $r^0_{slc}(p)$ represents the peak location in radial direction, and $\sigma_{slc}(p)$ is the standard deviation, which is $\sigma^L_{slc}(p)$ when $r < r^0_{slc}(p)$ and $\sigma^R_{slc}(p)$ when $r > r^0_{slc}(p)$. The PSF profiles were fitted using the Levenberg-Marquardt algorithm [Levenberg, 1944] [Marquardt, 1963] [Lourakis, 2004].

Because a relatively sparse grid was measured compared to the image grid, the PSFs at unmeasured locations needed to be determined. The parameters of the unknown PSFs were sampled from the models of the parameters. This procedure is illustrated in Fig. 5.4. The azimuthal angle (phi = 165) was chosen to be perpendicular to the p-axis and the depth of this angle is zero.

Because the count level varies dramatically across different slices for a given point source at a measurement location, the accuracy of the fitted radial profile may vary significantly in different slices. Fig. 5.5 provides an example of such fitting for different slices of a point source in measurement plane 0. The parameterization model matched the measured data in the high-statistics slice but not in the low-statistics slice. In addition, the estimated peak locations were slightly different. We ignored these errors because the low statistics slices were less significant than the high statistics in resolution modeling, and the peak positioning error was minimized with a geometric model.

The parameters A, σ^L and σ^R were fitted to parabolic functions of the locations of the point sources. An example of the fitting at a peak slice is displayed in Fig. 5.6. We noticed that radial profiles significantly vary across different slices for the PSF of a ray. An example of the fitting at a non-peak slice is illustrated in Fig. 5.7.

The parameter r^0 was then fitted as a function of the locations of the point sources for all of the slices. The function was [Panin et al., 2006a]:

$$p = (R + DOI \cdot cos(\theta))sin(\theta), \quad \theta = r^0 \frac{\pi}{N} \tag{5.2}$$

where R is the radius of the scanner, DOI is the depth of interaction (which was found to be 1.3 cm through fitting a model using Equation 5.2 and direct slices

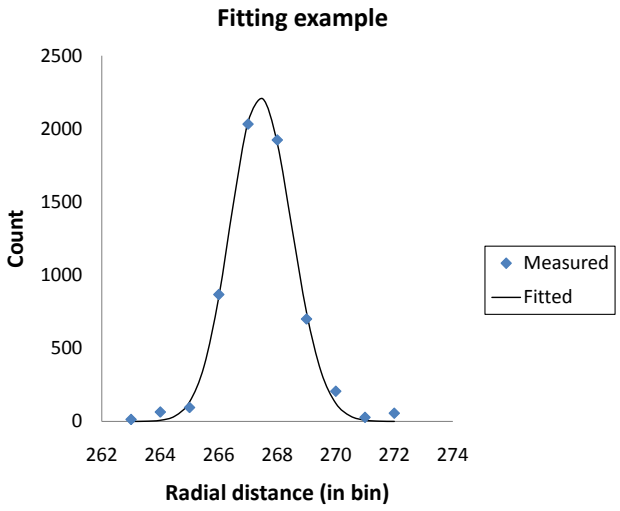

(a)

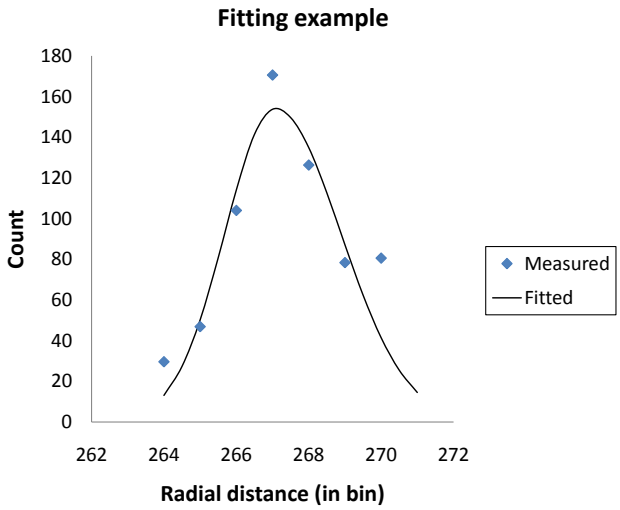

(b)

Figure 5.5: Fitting examples for a point source that is 1 cm off-center in measurement plane 0, (a) slice of ring pair (15,15), (b) slice of ring pair (15, 16).

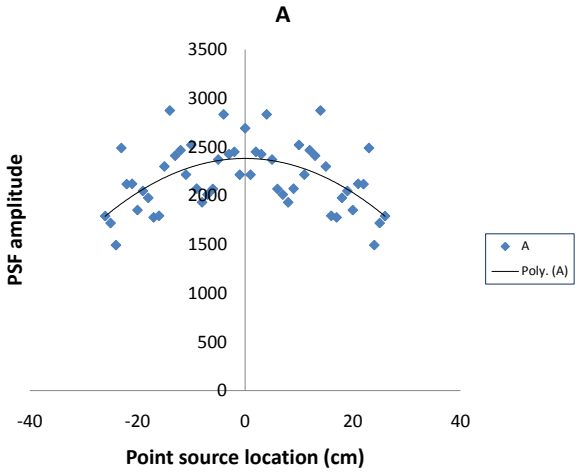

(a)

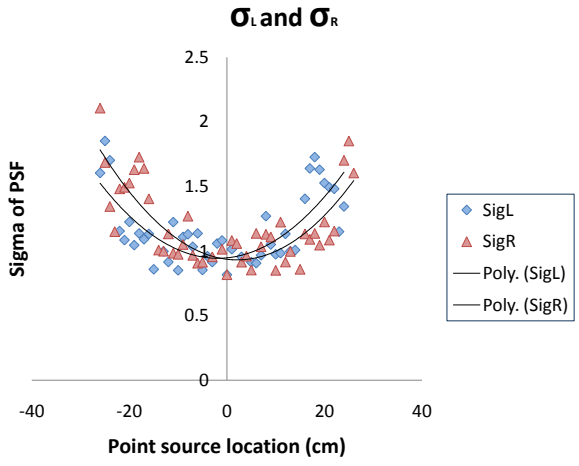

(b)

Figure 5.6: An example of fitting models to the parameters at the slice of ring pair (15, 15) for point sources in the measurement plane 0. (a) (b) The parameter A and σ are fitted to a parabola function of the locations of point sources. (c) The parameter ρ is fitted to Equation 5.2 of the locations of point sources.

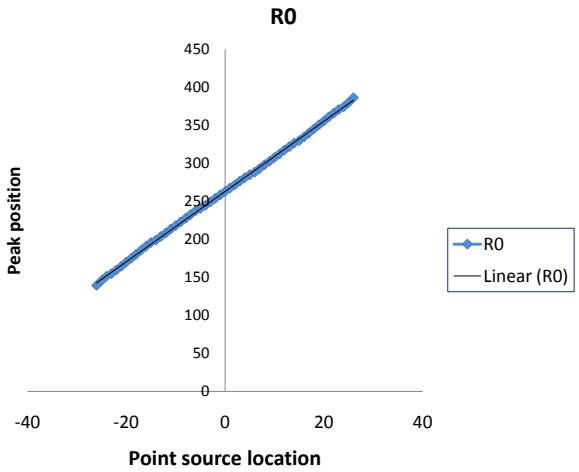

(c)

Figure 5.6: An example of fitting models to the parameters at the slice of ring pair (15, 15) for point sources in the measurement plane 0. (a) (b) The parameter A and σ are fitted to a parabola function of the locations of point sources. (c) The parameter ρ is fitted to Equation 5.2 of the locations of point sources.

of measurement data plane 0 – 8), and N is the number of crystal (including gaps (644)). As an example, fitting models to the parameters is illustrated in Fig 5.6.

5.2.3.2 Axial blurring modeling

The parameter A at peak locations across different slices was virtually linked and modeled by the sum of Gaussian functions that were continuously distributed across the slice space. In this work, we assumed that all these Gaussian functions have the same σ due to the small oblique angle ($< 12.5^\circ$ for the target scanner), despite the fact that the axial profiles could be slightly asymmetric or blurry for oblique LORs. This assumption also implies that the axial peak location is in a middle of a ring. The axial blurring function with amplitude normalized to unity was defined as follows:

$$PSF^{axl}_{slc} = e^{[-\frac{(slc - slc^0)slc)^2}{2\sigma^2}]} \tag{5.3}$$

where PSF^{axl} is the axial blurring function, and slc^0 is the peak location of the axial profile.

The overall PSF of this ray is a collection of the radial profiles weighted by the value of the axial profile function in each slice. Thus, the complete PSF can be

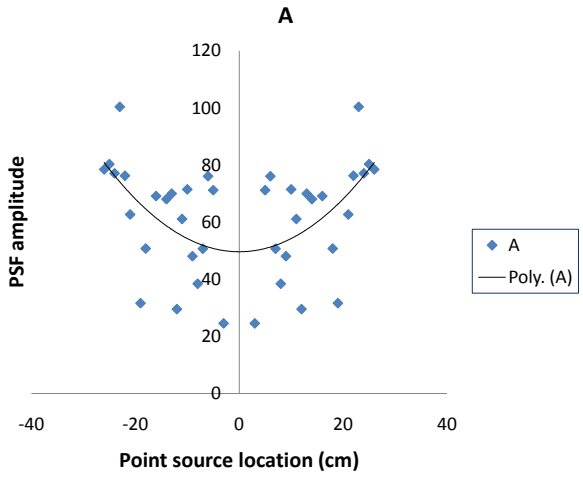

(a)

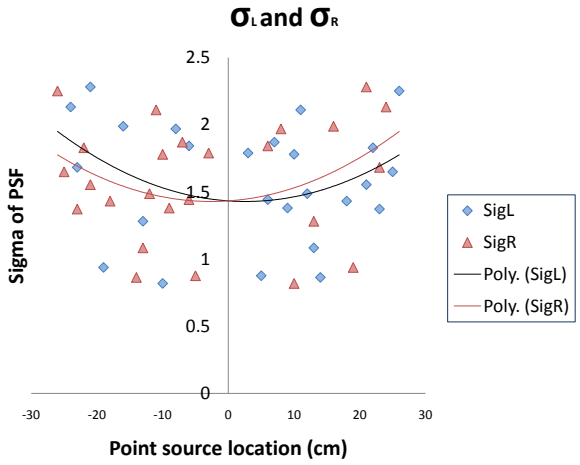

(b)

Figure 5.7: An example of fitting models to the parameters at the slice of ring pair (15, 16) for point sources in the measurement plane 0. (a) (b) The parameter A and σ are fitted to a parabola function of the locations of point sources. (c) The parameter ρ is fitted to Equation 5.2 of the locations of point sources.

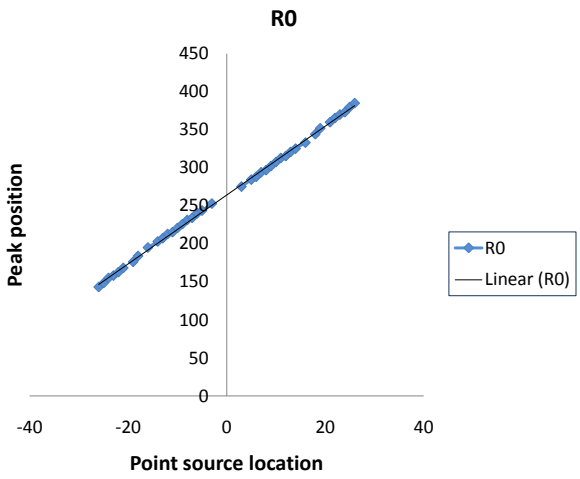

(c)

Figure 5.7: An example of fitting models to the parameters at the slice of ring pair (15, 16) for point sources in the measurement plane 0. (a) (b) The parameter A and σ are fitted to a parabola function of the locations of point sources. (c) The parameter ρ is fitted to Equation 5.2 of the locations of point sources.

expressed as:

$$PSF(r,p) = \sum_{slc} PSF_{slc}^{axl} PSF_{slc}^{rad}(r,p) \tag{5.4}$$

An example of the proposed PSF model is illustrated in Fig. 5.8. The radial and axial profiles of the proposed model are illustrated in Fig. 5.9. It can be seen that the PSF model is naturally a summation of all radial profiles at different slices. The summation model allows different radial profiles in different slices, while existing models do not permit such situations due to the constraints of the separable radial and axial profiles [Panin et al., 2006a]. Our summation PSF model may degrade into an existing model if we assume that all the radial profiles have the same shape across different slices, where the complete PSF model can be approximated as a product of the radial and axial profiles.

5.2.4 System matrix construction

In this work, we used a factorized matrix approach to model the complete system model:

$$\mathbf{A}_{N,I} = \mathbf{P}_{N,N}\mathbf{G}_{N,I} \tag{5.5}$$

where N and I are dimensions of the LOR histogram and image, $\mathbf{A}_{N,I}$ is the complete system matrix, $\mathbf{P}_{N,N}$ is the PSF component that models the blurring in

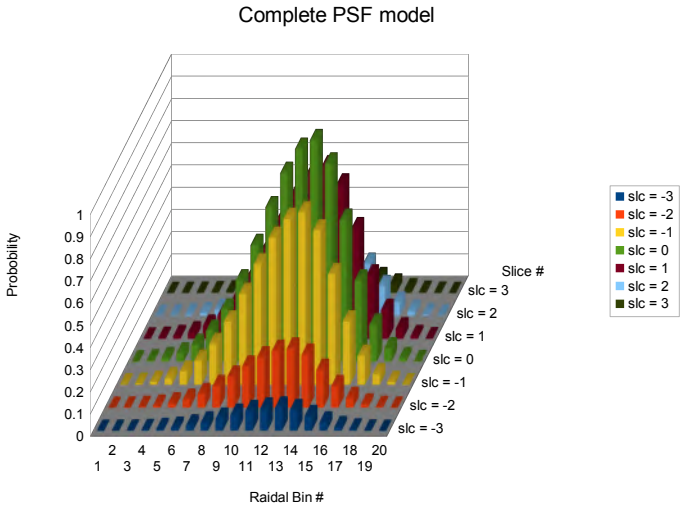

Figure 5.8: An illustration of the proposed PSF model.

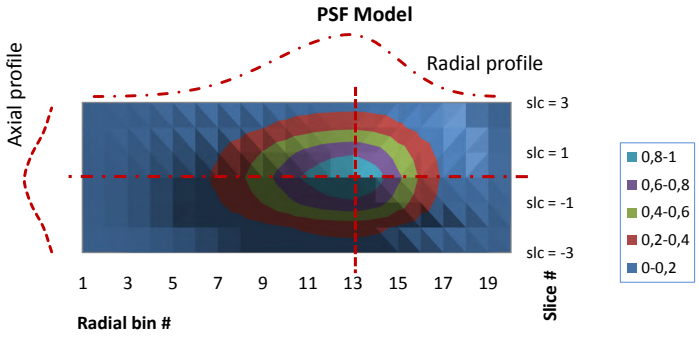

Figure 5.9: The PSF model and the radial and axial profile components. It can be seen that the PSF model is naturally a summation of all radial profiles. A summation model allows different radial profiles in different slices. This PSF model may degrade into a separable model if all the radial profiles have the same shape across different slices.

sinogram space, and $\mathbf{G}_{N,I}$ is the geometric component that models the solid angle effects.

We used a multi-ray Siddon algorithm to approximate these effects by randomly sampling and tracing 5000 rays per LOR. The size of the obtained geometric matrix $\mathbf{G}$ is about 220 Mb.

In order to determine the PSF component, the mapping that links the location of a point source to its axial and radial peak locations must be known. In contrast to radial peak locations, the axial peak locations are a complicated function of radial, depth, and axial positions of the point sources. To the best of our knowledge, no a established analytical model exists. Estimating these locations from measurements is also challenging because too many unknowns may cause the fitting to fail [Panin et al., 2006b]. In this initial implementation, the axial peak locations were assumed to be the center of a ring. And the relationship between the point source location and axial peak location were determined by a ray-tracing algorithm. This technique introduced a maximum positioning error of one axial bin, which has been shown to be negligible [Alessio et al., 2010]. The radial peak location was precisely determined by using equation 5.2 for each ray. We also assumed that the radial blurring of the LOR had the same shape across different slices, which is the shape of the radial blurring at the peak slice. This axial profile is a spatially invariant kernel, which has a FWHM of 0.86 slice bin. This parameter was estimated from the data from measurement plane 0 – 8. The size of the PSF component $\mathbf{P}$ is about 25 Mb.

5.2.5 Reconstruction

The rotator-based ordered subsets expectation maximization (OS-EM) [Hudson and Larkin, 1994] was used for image reconstruction [Zhang et al., 2010c]. The formula can be found in Chapter 4. The rotator was a Gaussian rotator with a one-pixel (2 mm) FWHM and a 3×3-pixel kernel [Wallis and Miller, 1997]. In the forward projection, the volume of intersection system model was first used and the projection was then distributed to its radial and axial neighbor bins. In the backprojection step, the ratio LOR histogram was first deblurred (both radially and axially) and then backprojected by the geometric system matrix. The forward projection and backprojection are illustrated in Fig. 5.10. Two system models were built and used in the reconstruction. In one model, the axial blurring was not included but the axial blurring was included in the other model.

5.2.6 Figures of merit

The contrast recovery coefficient (CRC) and noise calculated for the ROIs were used as figures of merit. The CRC of a hot lesion is expressed as follows:

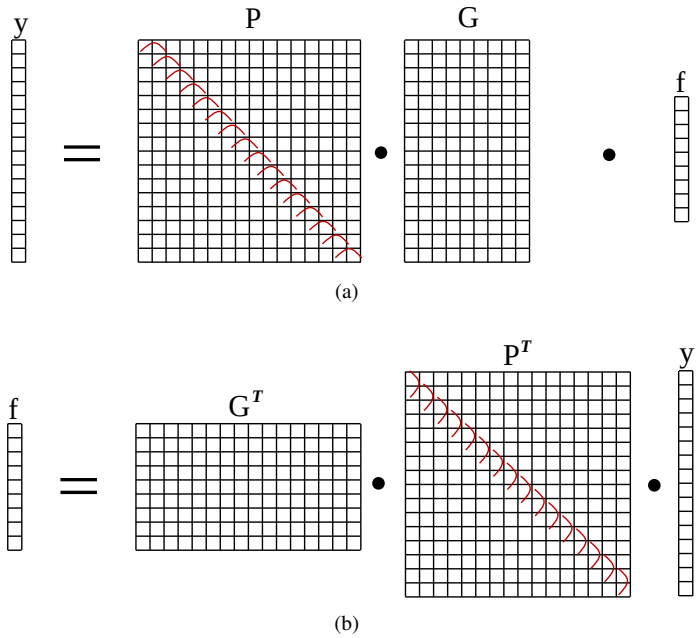

Figure 5.10: The forward- and back-projector. (a) The forward projection operation using the factorized matrix approach. (b) The backprojection operation using the factorized matrix approach.

$$CRC = \frac{1}{C}\frac{\bar{\mu}_h}{\bar{\mu}_b} \times 100\% \tag{5.6}$$

where $\bar{\mu}_h$ is the mean of the reconstructed activity in a hot lesion h, $\bar{\mu}_b$ is the mean of the reconstructed activity in the background, and C is the true hot-to-background contrast.

The CRC of a cold lesion is defined as:

$$CRC = \frac{\bar{\mu}_b - \bar{\mu}_l}{\bar{\mu}_b} \times 100\% \tag{5.7}$$

where $\bar{\mu}_l$ is the mean of the reconstructed activity in a cold lesion l.

The noise σ_n was calculated as the coefficient of variance (CV) in the background, expressed as:

$$\sigma_n = \frac{\sigma_{bgd}}{\mu_{bgd}} \times 100\% \tag{5.8}$$

where σ_{bgd} is the standard deviation in the background and μ_{bgd} the mean in the background.

5.2.7 Resolution properties

Six point sources were placed radially in the central image plane with a spacing of 5 cm, which covered a half-FOV from 0 cm to 25 cm. Each point source was scanned for 1 minute and the approximately 5 million prompts were collected. These point sources were then reconstructed using the proposed method with or without axial blurring modeled. The radial, tangential and axial resolutions were measured by fitting a Gaussian function through the peak using the fifth iteration of the reconstructed image. These point sources were not reconstructed by the scanner software because the clinical routine uses 4x4x4 mm^3 voxels. Thus, the resolution of the proposed method was compared to that of an OS-EM using a multi-ray Siddon (5 rays) projector, where the finite crystal size was modeled. The end-points of each ray were randomized to avoid artifacts. We also compared the resolution properties to the Monte Carlo-based reconstruction. The Monte Carlo system matrix was created by egs_pet with some of the VRTs described in Chapter 3. These VRTs are polar angle biasing, positron history reuse, hit-testing and the transport parameters were optimized. The details about these VRTs can be found in Chapter 3.

The volumetric resolution was calculated by the volume contained by the FWHM contour of a reconstructed point. This volume was approximated by the volume of an ellipsoid, whose radii were the FWHMs in different directions.

5.2.8 Phantom study

5.2.8.1 Jazsczak phantom

To evaluate the image quality, we scanned an image quality phantom on the Gemini GS PET/CT. The cylindrical container of the Deluxe Jaszczak phantom from DSC (Hillsborough, NC) was used, which was 18.6 cm in height and 21.6 cm in diameter. The hot/cold lesions used hollow spheres from the Hollow Sphere Sets (6) and Solid Sphere Sets (6) from DSC. The dimensions of the four hot spheres were 9.89 mm, 12.43 mm, 15.43 mm and 19.79 mm in diameter and the two cold spheres were 25.4 mm and 31.8 mm in diameter. The spheres were in a plane about 4.6 cm off-center. The background was filled with 0.98 mCi ^{18}F-FDG in water. The hot-to-background ratio was 4:1. The phantom was scanned for 25 minutes with approximately 200 million coincidences collected in list mode. The data were then pre-corrected for randoms, normalization effects, attenuation and scattering. The attenuation map was obtained from the CT scan. Scatter correction was applied by a single scatter simulation technique [Watson et al., 1997]. Again, the phantom was reconstructed using the proposed method with or without axial blurring.

The new approach was compared to the commercial algorithm equipped on the scanner and an algorithm employing the same rotator and a Monte Carlo-derived SM with fully simulated positron range effects. Both the new approach and the Monte Carlo-based algorithm used the raw LOR histogram [Kadrmas, 2004] as an input, which was pre-corrected for randoms, attenuation and scattering effects. The subset level was chosen to be 23 in both approaches.

The scanner software used an interpolated sinogram with seven tilts. The image was reconstructed on 2x2x2 mm^3 grid with a blob-based RAMLA algorithm. Clinical routine settings were used during the reconstruction and iterated at the 10th iteration [Surti and Karp, 2004].

5.2.8.2 Hoffman phantom

We also scanned a Hoffman phantom (from DSC) to evaluate the overall performance of the reconstruction algorithm on the Gemini GS PET/CT. The phantom was filled with 1.0 mCi ^{18}F in water, and scanned for about 20 minutes. The collected coincidences were about 110 million. All corrections were applied to the data before reconstruction.

The data were reconstructed using our method with the full PSF model (including both axial and radial blurring) and the commercial software on the scanner, which used clinical routine settings and iterated up to 10 iterations [Surti and Karp, 2004]. The subset level was chosen to be 23 in our reconstruction method.

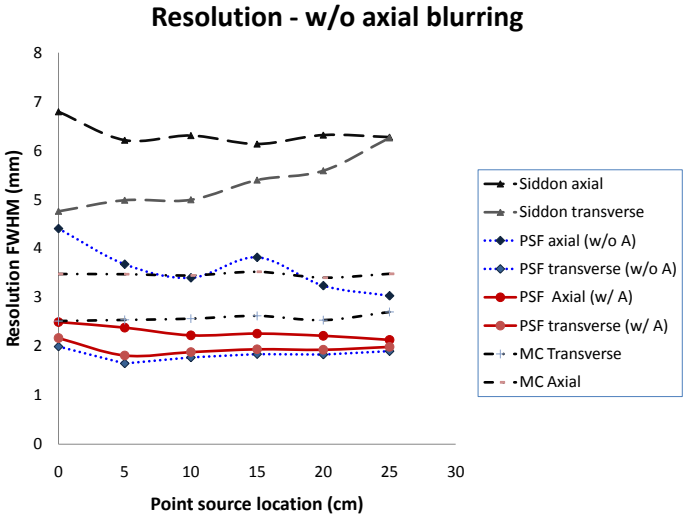

Figure 5.11: Volumetric resolution of the PSF modeling (with or without axial blurring), the Monte Carlo-based method and the OSEM Siddon approach. The volumetric resolutions were measured at the fifth iteration with 23 subsets.

5.3 Results

5.3.1 Resolution properties

The resolution of the proposed method with or without axial blurring is compared to a standard OS-EM algorithm using the multi-ray Siddon projector and to the Monte Carlo-based approach described in Chapter 4. The radial, tangential and axial FWHMs of the reconstructed point sources are displayed in Fig. 5.11. The manufacturer's data are listed in Table 5.2. These data were measured using the 3D-FRP algorithm with a narrow filter [Surti and Karp, 2004].

Locations (cm)	Resolution transverse (mm)	Resolution axial (mm)
1	3.77	5.31
10	5.46	6.44
15	6.78	15.74
20	7.62	15.48

Table 5.2: The resolution properties from the manufacturer. Reproduced from [Surti and Karp, 2004].

The volumetric resolution as a function of point source locations is also plotted in Fig. 5.12 for the Monte Carlo-based approach, the standard OS-EM using

Siddon projector and the proposed method with or without axial blurring. The volumetric resolutions were measured at the fifth iteration with 23 subsets. The mean volumetric resolution as a function of iteration number is plotted in Fig. 5.13with increasing iteration number for the point source at the center of the FOV and a point source 10 cm off-center.

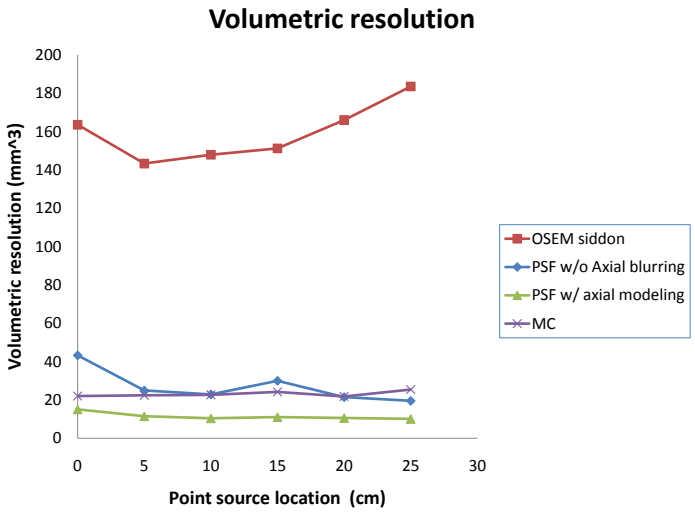

Figure 5.12: The volumetric resolution as a function of point source locations at the 5th iteration of the standard OS-EM using Siddon projector and the proposed method with and without axial blurring.

5.3.2 Image quality evaluation

5.3.2.1 Jazsczak phantom

The reconstructed slices of the phantom with or without axial blurring are shown in Fig. 5.14 (transverse view in Fig. 5.14a and 5.14b, coronal view in Fig. 5.14d and 5.14e and sagittal view in Fig. 5.14g and 5.14h) for the proposed method. The reconstruction of the manufacture's method is listed in the rightmost column for reference. Ringing artifacts can be detected along the edge of the background in the transverse view for both system models (see Fig. 5.14a, 5.14b).

In Fig. 5.15 the CRC vs. noise is plotted for the proposed method with axial blurring, the Monte Carlo-based method and the manufacture's method (Philips). Fig. 5.15a and 5.15b contain the curves for hot and cold lesions, respectively.

To evaluate the effects of axial blurring, the CRC vs. noise is plotted for the proposed method with or without axial blurring in Fig. 5.16.

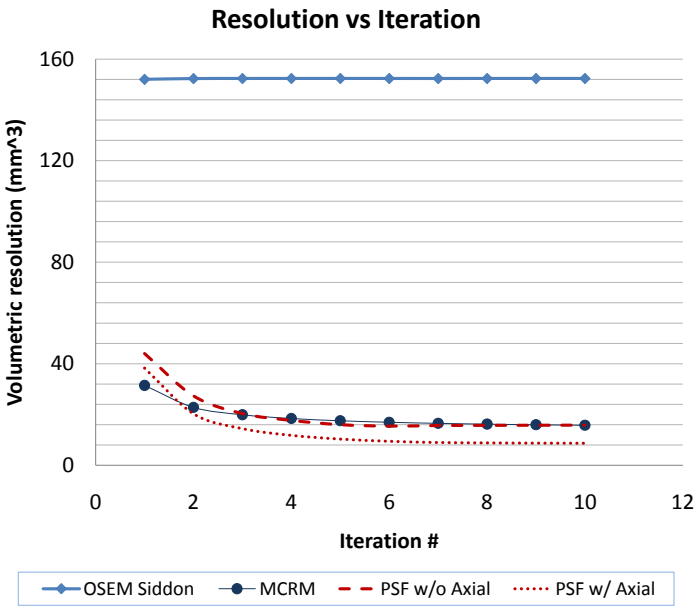

Figure 5.13: The mean volumetric resolution as a function of iteration number for a point source at the center of the FOV and a point source 10 cm off-center.

5.3.2.2 Hoffman phantom

Images of the proposed method, Monte Carlo-based resolution modeling and the clinical software are displayed in Fig. 5.17. The tenth-iteration images were obtained for the proposed method, the Monte Carlo method and the clinical software.

5.4 Discussion

The proposed method directly parameterized the profiles in each slice of a PSF. Our approach is different from existing measurement-based techniques, where the PSF is modeled as separable radial and axial components to downsize the size of the system matrix [Panin et al., 2006a]. In our approach, the PSF is modeled as the weighted sum of the radial profiles and the weights are the axial component. This small change allows fitting different radial profiles in different slices to accurately reconstruct a measured PSF.

The amplitudes of the radial profiles were then fitted to a Gaussian function to further smooth the PSF model. This Gaussian function can be regarded as the axial profile in existing approaches [Panin et al., 2006a]. Despite we assumed a fixed location in this initial work, the peak location of this axial profile modeling can be determined by a new model to include the DOI effects in axial direction.

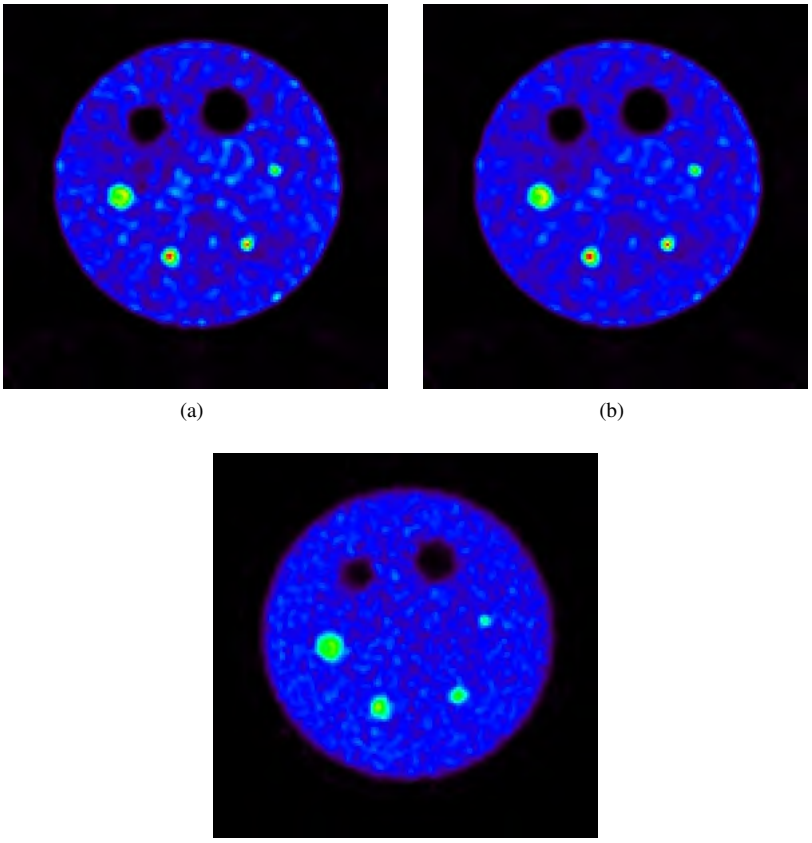

(a) (b)

(c)

Figure 5.14: Reconstruction examples for the proposed method without axial blurring. (a), (d) and (g) show the transverse, coronal and sagittal views, respectively, of the model without axial blurring. (b), (e) and (h) show the transverse, coronal and sagittal views, respectively, of the model with axial blurring. (c), (f) and (i) are the transverse, coronal and sagittal views, respectively, of manufacture's method.

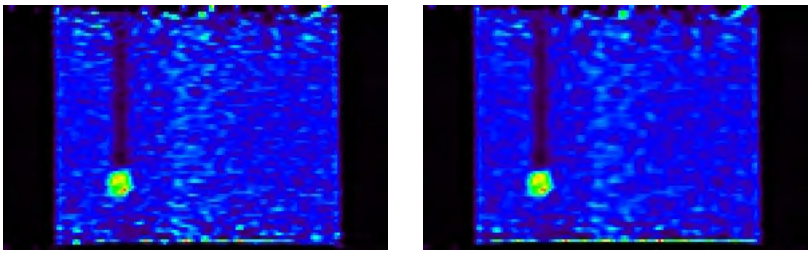

(d) (e)

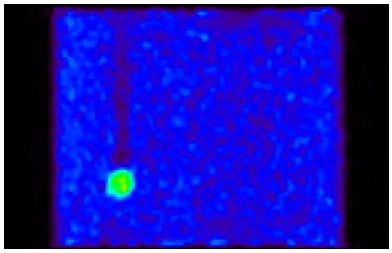

(f)

Figure 5.14: Reconstruction examples for the proposed method without axial blurring. (a), (d) and (g) show the transverse, coronal and sagittal views, respectively, of the model without axial blurring. (b), (e) and (h) show the transverse, coronal and sagittal views, respectively, of the model with axial blurring. (c), (f) and (i) are the transverse, coronal and sagittal views, respectively, of manufacture's method.

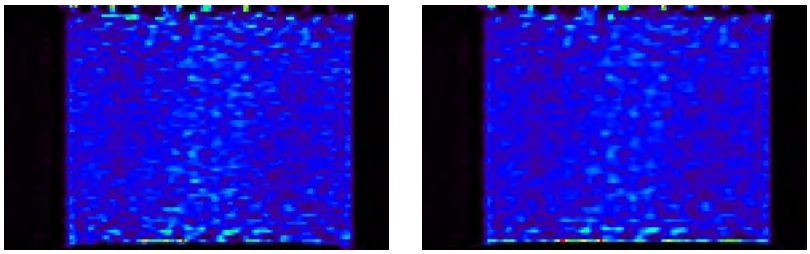

(g) (h)

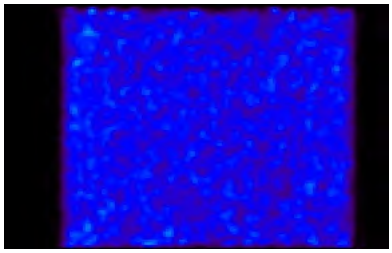

(i)

Figure 5.14: Reconstruction examples for the proposed method without axial blurring. (a), (d) and (g) show the transverse, coronal and sagittal views, respectively, of the model without axial blurring. (b), (e) and (h) show the transverse, coronal and sagittal views, respectively, of the model with axial blurring. (c), (f) and (i) are the transverse, coronal and sagittal views, respectively, of manufacture's method.

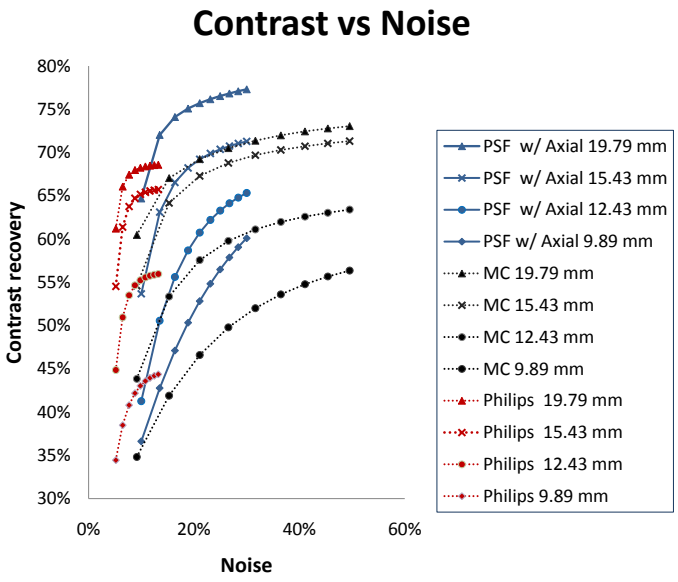

(a)

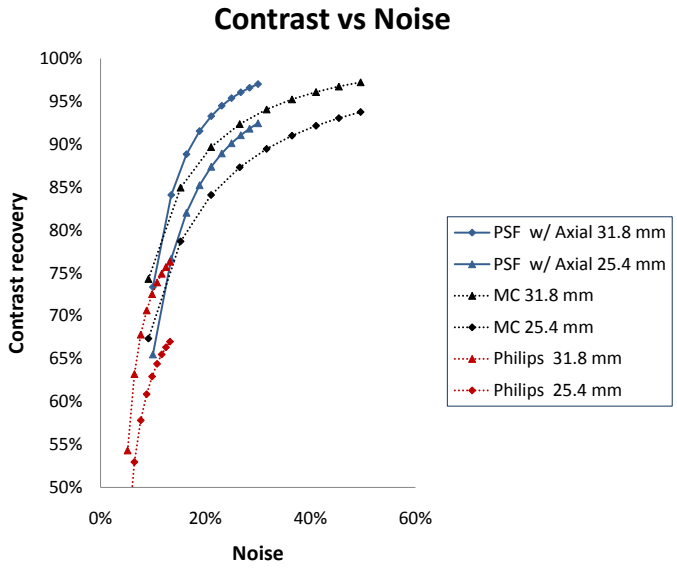

(b)

Figure 5.15: Contrast noise trade-offs of the image quality phantom. Each point represents a single iteration of the proposed method (PSF modeling with axial blurring), the Monte Carlo-based method and the manufacture's method (Philips). (a) Hot lesions. (b) Cold lesions.

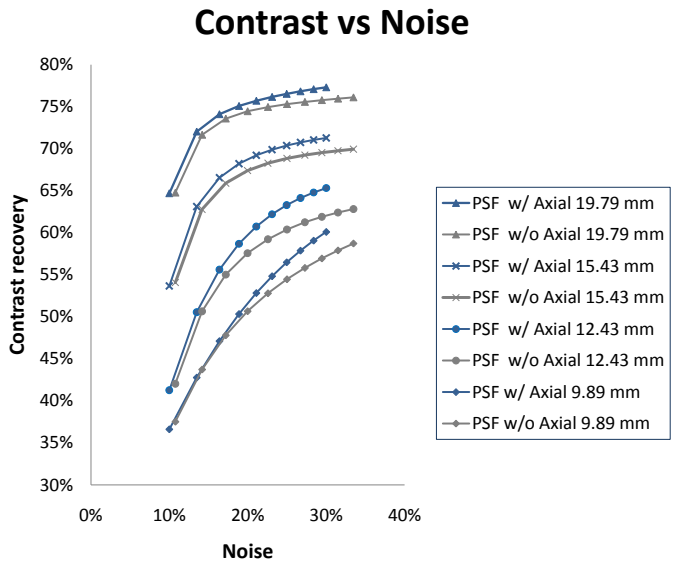

(a)

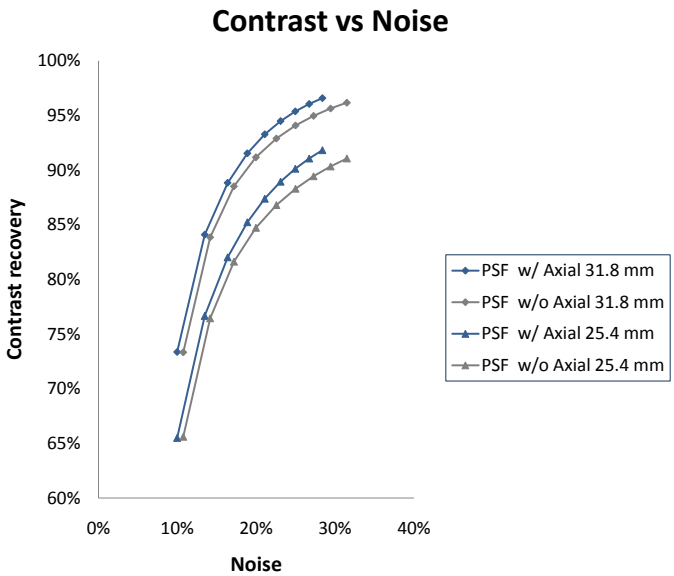

(b)

Figure 5.16: Contrast noise trade-offs of the image quality phantom. Each point represents a single iteration of the proposed method with or without axial blurring in the system model. (a) Hot lesions. (b) Cold lesions.

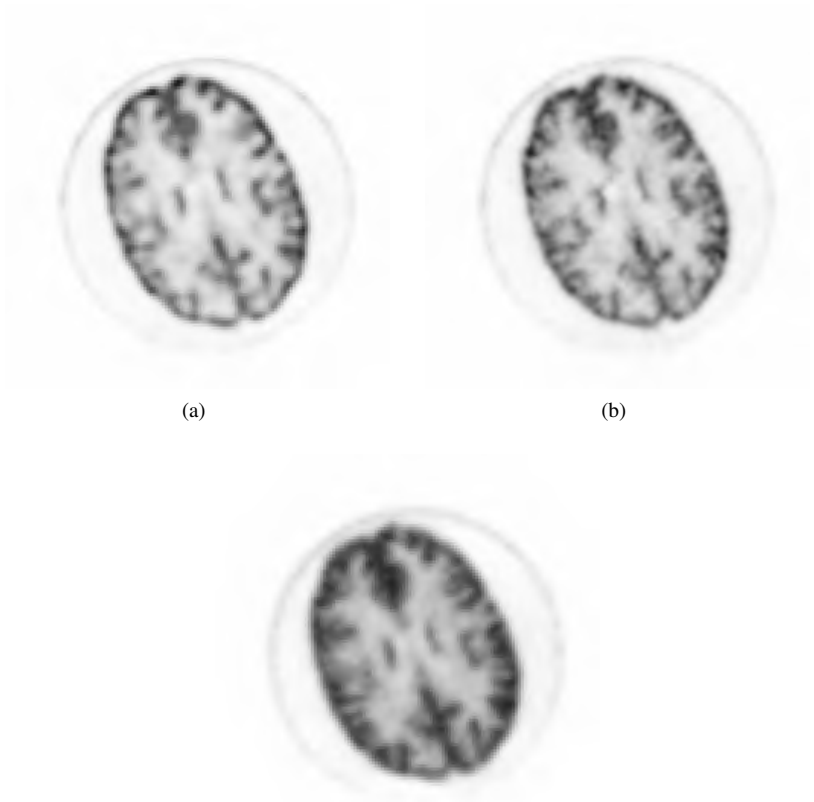

(a) (b)

(c)

Figure 5.17: Hoffman phantom at the 10th iteration. (a) (c) (e) The transverse, coronal, and sagittal view of the image reconstructed by the PSF method. (b) (d) (f) The transverse, coronal, and sagittal views of the image reconstructed by the clinical software.

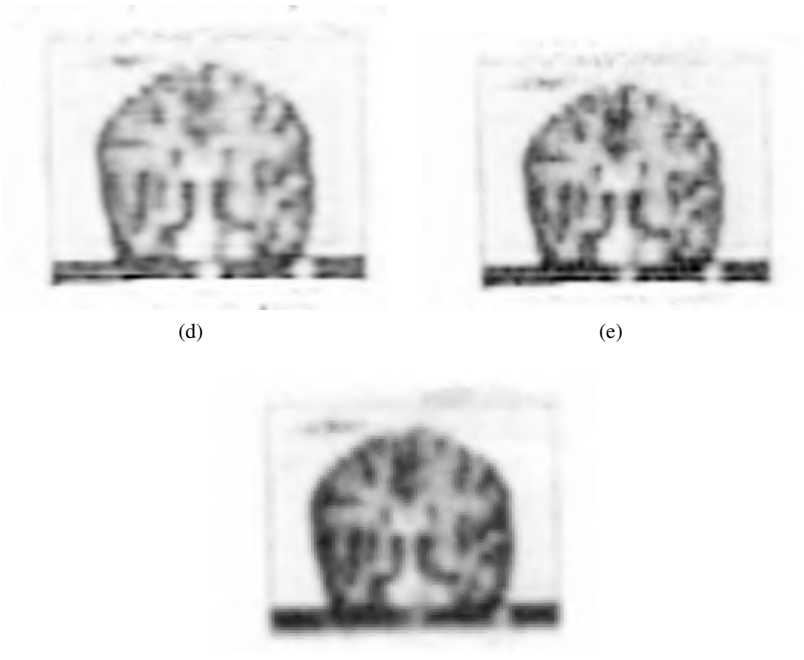

(d) (e)

(f)

Figure 5.17: Hoffman phantom at the 10th iteration. (a) (c) (e) The transverse, coronal, and sagittal view of the image reconstructed by the PSF method. (b) (d) (f) The transverse, coronal, and sagittal views of the image reconstructed by the clinical software.

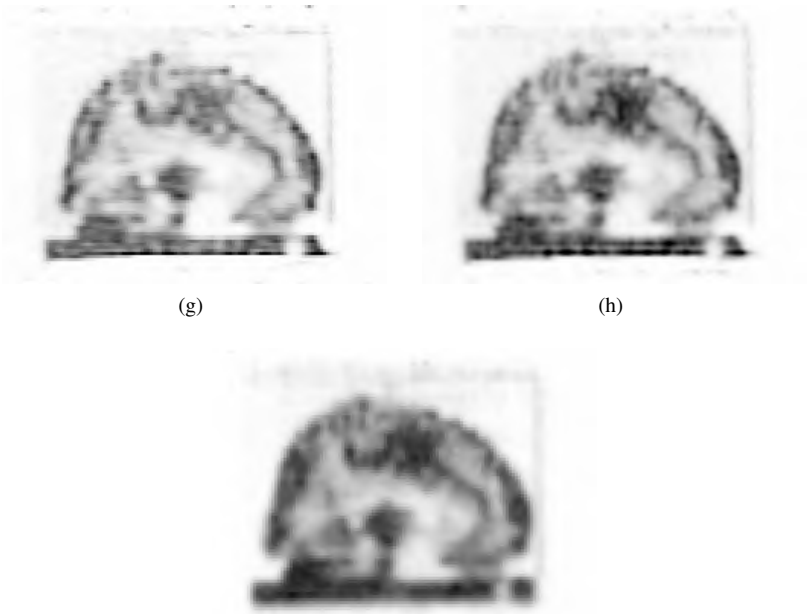

(g) (h)

(i)

Figure 5.17: Hoffman phantom at the 10th iteration. (a) (d) (g) The transverse, coronal, and sagittal view of the image reconstructed by the PSF method. (b) (e) (h) The transverse, coronal, and sagittal view of the image reconstructed by the Monte Carlo method. (c) (f) (i) The transverse, coronal, and sagittal views of the image reconstructed by the clinical software.

This method will be investigated in the future.

In this initial implementation, we approximated this model by assuming that the radial profiles of the PSF of a ray are the same. It can be proved that the proposed PSF model degraded into a separable model under this approximation. A full implementation of the proposed model yields a more accurate PSF model, but the memory required to store the PSF blurring matrix substantially increases. An optimal configuration of the proposed system model could be achieved by balancing the complexity of the system model and the image quality. This hypothesis will be investigated in the future.

The contrast recovery was improved compared to that of the Monte Carlo-based approach because the accuracy of the model was better than the Monte Carlo-based approach. Due to the smoothness of the parameterized model, the image was significantly less noisy than the Monte Carlo-based method. The commercial algorithm yielded the best noise performance because the radius of the blobs was 2.5 pixels, which regularized the images to be smooth [Wang et al., 2004] [Vanhove et al., 2007].

Axial blurring was found to be an important factor in the axial resolution. However, the improvement in contrast noise trade-offs from including axial blurring effects is limited, which is consistent with the finding of peer researchers [Alessio et al., 2010]. We also noticed that the contrast recovery of the smaller hot lesions was increased more than the larger hot lesions. This improvement makes the modeling of axial blurring attractive because improved contrast recovery of small hot lesions is clinically important [Kim et al., 2005]. This finding also suggests that the modeling of axial blurring is important in small animal PET imaging, where the lesion sizes are smaller.

Ringing artifacts were detected along the edge of the background in the image reconstructed using the proposed method. However, ringing was not detected in the Monte Carlo-based approach in the experimental data study in chapter4. These phenomena indicate that the system responses obtained in this work are blurrier than those obtained by Monte Carlo simulations.

The scanner had large detector panel, which may damage the assumption of azimuthal independence. Our study showed that the azimuthal independence assumption was appropriate. In the current implementation, only part of the data was used to build the model because we ignored the difference between the blurring of the oblique LORs and the direct LORs due to the small oblique angle. This assumption is frequently used in PSF modeling, where the axial profile is estimated from data of one line or plane of point sources [Tohme and Qi, 2009] [Alessio et al., 2010].

In addition to the Gaussian rotator-based approach, an ideal rotator could also reduce the storage requirements. A measured system matrix with polar-pixel discretization requires integral of the PSFs within the polar voxel elements. This

approach will be investigated in the future.

5.5 Conclusions and original contributions

The results show that our technique is promising in terms of its resolution properties and contrast noise trade-offs. Our method allows a very compact system model ($<$ 250Mb) with complete system responses modeled. Our studies indicate that the axial blurring remains an interesting component because including this effect considerably improved the axial resolution and contrast recovery for small hot lesions.

In this work, we presented a factorized system model in PET image reconstruction. A blurring component that directly parameterized the profiles of the PSFs was obtained from point source data. This technique has several advantages over existing techniques, such as increased accuracy and readiness for fully 3-D reconstruction. The downsides are the increased complexity and increased storage requirement for the full PSF model.

Chapter 6

Ringing Artifacts in Resolution Modeling

In this chapter, we investigated the origin and characterized the behavior of the ringing artifacts detected in the approach using a blurring Gaussian rotator (see Chapter 4 for details). An ideal rotator was proposed to provide a baseline for these investigations.

6.1 Introduction

As mentioned in Chapter 4, the rotator-based method solves some of the issues in applying Monte Carlo resolution modeling into state-of-the-art whole body PET scanners, such as the memory requirement for storing the SM and the expensive computational cost for calculating the SM. However, pronounced ringing artifacts in reconstructed images were detected when applying the rotator with an accurate system model. Ringing artifacts have been reported (or can be detected) in many recent works employing an accurate system model, particularly, a measurement-derived system model [Qi et al., 1998, Reader et al., 2003, Panin et al., 2006a, Sureau et al., 2008, Tohme and Qi, 2009, Alessio et al., 2010, Wiant et al., 2010].

Here, we propose an ideal rotator, which yields perfectly rotated images, to investigate the origin and behaviors of these aforementioned artifacts. The ideal rotator method was used as a baseline to analyze the artifact behavior of the Gaussian rotator method. A full system model and a partial system model without positron range and acolinearity modeled for ^{18}F studies were used during this evaluation. The full system model was used for the artifact investigation and the partial system model was used to investigate the feasibility of employing the blurring of the rotator to compensate for certain resolution loss effects. Noiseless data, Monte Carlo simulation data and acquired data were employed to quantitatively characterize the

behavior of artifacts in the Gaussian rotator-based method. The angle-independent and predictable blurring of the Gaussian rotator [Wallis and Miller, 1997] provides valuable information about how much over-compensation is tolerable for PET reconstruction in practice.

6.2 Theory

6.2.1 The Ideal Rotator

Polar pixels have been intensively used in small animal PET systems for resolution compensation [Scheins et al., 2006, Mora and Rafecas, 2006, Ansorge, 2007, Leroux et al., 2007a]. We used a "square" like polar-pixels discretization [Mora and Rafecas, 2006], as illustrated in Fig. 6.1. Our ideal rotator is based on this image discretization. This discretization shows a radial symmetry in a cylindrical PET, as illustrated in Fig. 6.1. It is perfect or "ideal" for rotating the image to reach a radial symmetry position since no interpolation is required (Fig. 6.1b). The inherent radial symmetry can be fully utilized when the number of segments of polar-pixel discretization equals to the number of detector blocks.

The polar-pixel representation is converted to Cartesian discretization to display the image or perform Regions of Interest (ROI) analysis. This transformation maps the polar pixels to voxels by calculating the 2-D area-of-overlapping using a convex-hull algorithm [Brown, 1979].

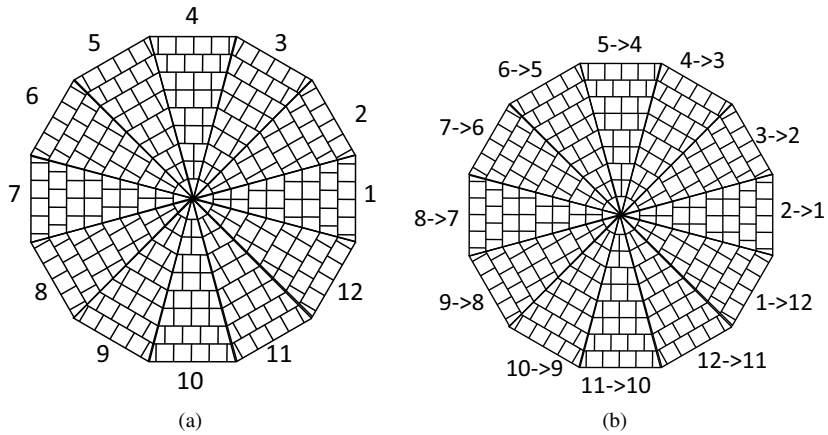

Figure 6.1: (NOT TO SCALE) Illustration of polar-pixel topology and image rotation. (a) Polar-pixel discretization. (b) Image rotation is "ideal" for radial symmetry positions.

6.2.2 Analytical modeling of positron range and acolinearity

Positron range has been intensively studied in PET applications, such as experimental measurements [Derenzo, 1986], Monte Carlo simulations [Levin and Hoffman, 1999] and empirical modeling [Harrison et al., 1999]. In early days of PET, the positron range was compensated by deconvolution methods [Derenzo, 1986, Hebert et al., 1990]. However, the noise was significantly amplified. Recently, this effect has been modeled in the SM of an iterative scheme, and improvements were reported in ^{82}Rb studies [Rahmim et al., 2008, Alessio and MacDonald, 2008].

The distribution of the positron range can be fitted to the sum of two exponential functions, expressed as [Levin and Hoffman, 1999]:

$$P(r) = De^{-k_1 r} + (1 - D)e^{-k_2 r} \qquad r \geq 0 \tag{6.1}$$

The acolinearity of the annihilation photon is modeled as a Gaussian distribution with a mean $m = 0$ and a full-width-at-half-maximum (FWHM) $FWHM = 2.35\sigma = 0.0026L$ (in mm), where L is the separation of the detector pair in a cylindrical scanner [Rahmim et al., 2008, Jan et al., 2004]:

$$A(r) = Ee^{-\frac{r^2}{2\sigma^2}} \tag{6.2}$$

where E is a normalization factor.

The overall blurring of these two factors is the convolution of the two components: $P(r) \otimes A(r)$. For ^{18}F, D is 0.516, k_1 is 0.379 (mm^{-1}) and k_2 is 0.031 (mm^{-1}) [Levin and Hoffman, 1999]. This model yields a Gaussian shape blurring kernel (Fig. 6.2). The FWHM of the total blurring is plotted as a function of the off-center distance for a cylindrical PET scanner, as shown in Fig. 6.2c.

6.3 Materials and Methods

6.3.1 The PET scanner

We used the Philips Gemini GS PET/CT scanner. The technique specification of this scanner can be found in section 4.2.1 of Chapter 4. The characteristics of the image volume and sinogram settings are the same as in Table 4.2 of Chapter 4.

6.3.2 System Matrix Simulation

In the SM calculation, we used the EGSnrc based code egs_pet, which has been reported to be 15 to 130 times faster than GATE [Jan et al., 2004, Kawrakow et al., 2008c]. Uniform sources were used in the simulation of the SMs and

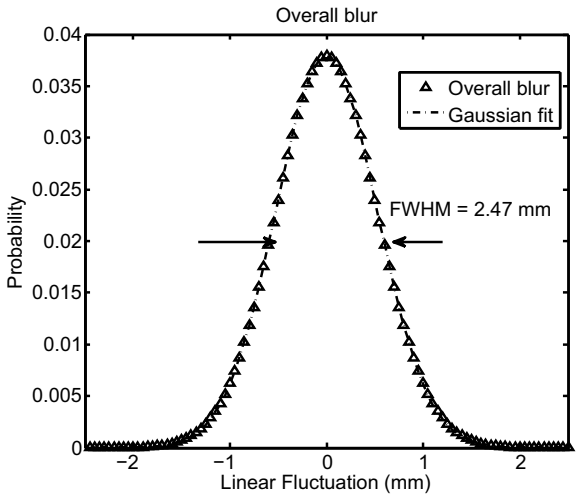

(a)

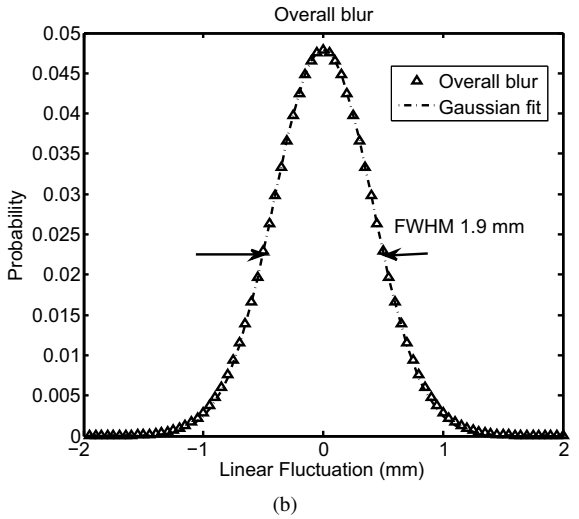

(b)

Figure 6.2: Overall blurring of positron range and acolinearity (a) at the center and (b) at the edge (288 mm off-center) of the FOV. (c) FWHM as a function of the off-center distance

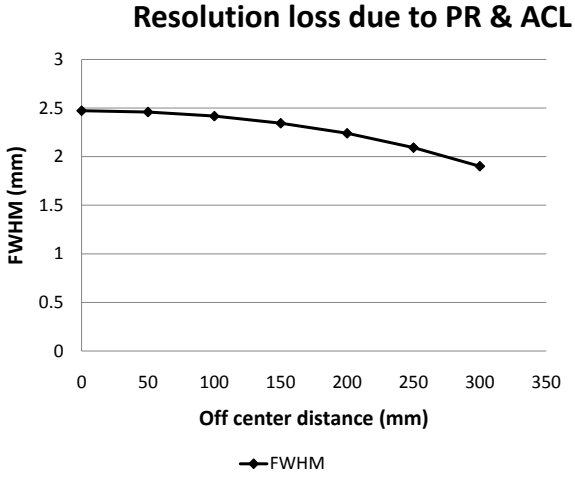

(c)

Figure 6.2: Overall blurring of positron range and acolinearity (a) at the center and (b) at the edge (288 mm off-center) of the FOV. (c) FWHM as a function of the off-center distance

then discretized into polar pixels or voxels during post-processing. The SM element was calculated by counting detected events for the associated LOR-voxel pair. A water phantom was used to allow the positron transport and annihilation. But photon-matter interactions within this phantom were disabled. This setting excluded the object dependent factors such as attenuation and scattering of the object. The time-independent simulation was applied, which not only excludes acquisition parameter-dependant factors but also provides possibilities for implementing simulation efficiency improvement techniques [Zhang et al., 2010c]. Geometrical symmetries such as in-plane rotational symmetry and axial translational and reflection symmetries were exploited to improve the statistics of the SM at no additional cost on simulation.

Two SM simulations were performed. The first simulation used a positron source, simulating the complete positron range and acolinearity; the second simulation employed a back-to-back gamma source, without simulating positron range and acolinearity. System matrices were derived for both the voxel discretization and the polar-pixel discretization. Using the same number of decays, three base-symmetry system matrices were generated from these simulations: $A^{p,pol}$ (positron source simulation, polar pixels discretization), $A^{p,v}$ (positron source simulation, voxels discretization) and $A^{g,v}$ (gamma source simulation, voxels discretization). The characteristics of these system matrices are listed in Table 6.1. System matrices $A^{p,v}$ and $A^{p,pol}$ are the full system models using different object parameterizations and the SM $A^{g,v}$ is the partial one.

SM statistics	**SM** $A^{p,v}$	**SM** $A^{g,v}$	**SM** $A^{p,pol}$
SM mean	15.1	15.5	14.9
SM max	260	287	185
SM storage (Gb)	2.31	2.26	2.20

Table 6.1: System matrix characteristics

6.3.3 Figures of merit

6.3.3.1 Contrast recovery

The contrast recovery coefficient (CRC) and noise calculated on ROIs were used as figures of merit. ROIs for lesions were defined in Fig. 6.3a. The CRC of a hot lesion is expressed as:

$$CRC = \frac{1}{CZ} \sum_{z=1}^{Z} \frac{\bar{\mu}_{h,z}}{\bar{\mu}_{b,z}} \times 100\% \tag{6.3}$$

where z is the realization number and Z the total number of realizations. $\bar{\mu}_{h,z}$ is the mean of the reconstructed activity in a hot lesion h of a realization z, $\bar{\mu}_{b,z}$ is the mean of the reconstructed activity in the background of a realization z and C is the true hot-to-background contrast.

The CRC of a cold lesion is defined as:

$$CRC = \frac{1}{Z} \sum_{z=1}^{Z} \frac{\bar{\mu}_{b,z} - \bar{\mu}_{l,z}}{\bar{\mu}_{b,z}} \times 100\% \tag{6.4}$$

where $\bar{\mu}_{l,z}$ is the mean of the reconstructed activity in a cold lesion l of a realization z.

The noise σ_{n} is denoted as:

$$\sigma_n = \frac{1}{B\bar{\mu}_b} \sum_{b=1}^{B} \sigma_b \times 100\% \tag{6.5}$$

where B is the total number of pixels in the background, $\bar{\mu}_b$ is the mean of the reconstructed activity in the background of different realizations and σ_{b} is the standard deviation of the reconstructed activities within a pixel b within the background ROI over different realizations. For a single realization, i.e. the measurement study, the noise was calculated as the coefficient of variance (CV) in the background, expressed as:

$$\sigma_n = \frac{\sigma_{bgd}}{\mu_{bgd}} \times 100\% \tag{6.6}$$

where σ_{bgd} is the standard deviation in the background and μ_{bgd} the mean in the background.

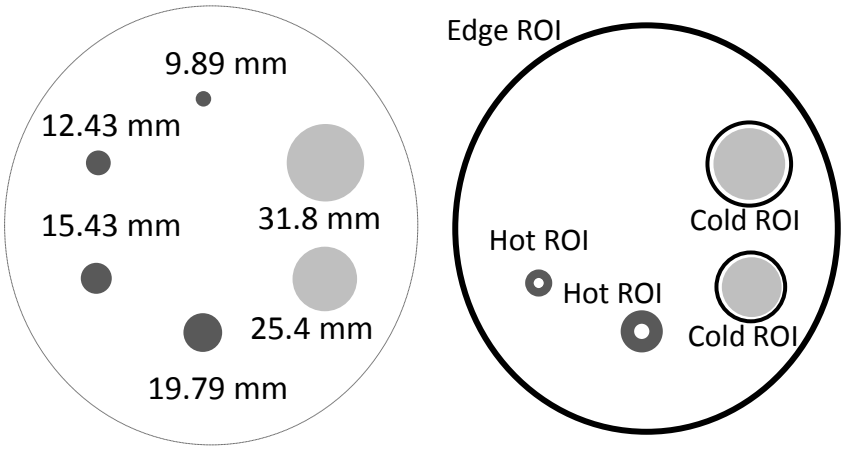

(a) (b)

Figure 6.3: ROI definitions. (a) ROI for lesions. (b) ROI for artifact evaluation: dark annular ROIs are for cold lesions and the edge of the background; white circular ROIs within hot lesions are for hot lesions.

6.3.3.2 Artifacts Evaluation

To quantify the ringing artifacts, ringing indices were calculated on ROIs at different places. In Fig. 6.3b, three annular ROIs were used to characterize ringing at the edge of the background and cold lesions and two small circular ROIs were used to quantify the ringing of the associated hot lesions.

For hot lesions, the ringing index was defined as the ratio of the mean in an artifact ROI to the mean value of the associated lesion; for cold lesions and the edge, the ringing index was defined as the ratio of the mean in an artifact ROI to the mean in the background. In the noiseless study, the minimum of an artifact ROI was used to evaluate the ringing in hot lesions, and the maximum in an artifact ROI was used to quantify the ringing at cold lesions. For multi-realizations, i.e. in the Monte Carlo study, the ring indices were the average of ringing indices from different realizations. The ringing index of a hot lesion equals to one for true images and is less than one for images with ringing artifacts (Fig. 6.4). For a normal reconstruction, the reconstructed image has a taper profile and the ringing index is greater than one. We call this error the taper artifact, which is induced by the partial volume effect (Fig. 6.4).

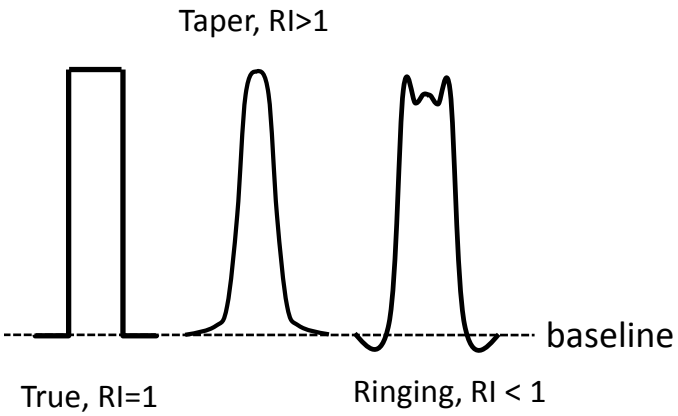

Figure 6.4: The Ring Index (RI) for hot lesions. Left: artifact-free image, RI equals to 1; Middle: taper artifacts, RI $>$ 1; Right: ringing artifacts, RI $<$ 1.

6.3.4 Image reconstruction

In this article, our rotator-based algorithm was used for image reconstruction [Zhang et al., 2010c]. The Gaussian rotator with a 1-pixel (2 mm) FWHM and a 3×3-pixel kernel [Wallis and Miller, 1997] was used in an ordered subsets expectation maximization (OS-EM) [Hudson and Larkin, 1994] algorithm. For Gaussian rotator-based reconstruction, the SM $A^{p,v}$ and $A^{g,v}$ were used.

The baseline algorithm used the polar-pixel discretization. The polar-pixel discretization has 58 image planes and each plane was divided into 28 segments with 2,450 polar pixels per segment. The SM $A^{p,pol}$ was used in the ideal rotator approach. The raw LOR histogram [Kadrmas, 2004] was used as input in both the Gaussian rotator approach and the baseline method. The OS level was chosen to be 22 in both approaches.

6.3.5 Noiseless Data Studies

To characterize the artifacts caused by the blurring rotator, reconstructions of the noiseless data were performed. The noiseless projection was obtained by forward projecting a numerical phantom by the ideal rotator method using $A^{p,pol}$. The numerical phantom consists of 4 hot spheres (9.89, 12.43, 15.43 and 19.79 mm in diameter) with a ratio of 4:1 to background and 2 cold spheres (25.4 and 31.8 mm in diameter) located at the central plane. The background was a cylinder of 204 mm in diameter and 150 mm in height. The noiseless data were reconstructed using the Gaussian rotator method with SM $A^{p,v}$ and SM $A^{g,v}$ and were compared

with that of the baseline method using SM $A^{p,pol}$.

6.3.6 Simulation Studies

Realistic data were simulated using egs_pet to investigate the effects of noise on artifacts in the Gaussian rotator method. An customized image quality phantom was used in this study, which consists of 4 hot spheres (9.89, 12.43, 15.43 and 19.79 mm in diameter) with a ratio of 4:1 to background and 2 cold spheres (25.4 and 31.8 mm in diameter) located at the central plane. The background was a cylinder of 204 mm in diameter and 150 mm in height, which was filled with ^{18}F-FDG in water. The water was used as the annihilation medium, but photon attenuation was not simulated within it. Acolinearity of the annihilation photon was modeled for annihilation at rest. Realistic photon-detector interactions were fully modeled. The detector outputs were digitized using the signal processing chains of egs_pet, which provide the same output as GATE given the same detector signals [Kawrakow et al., 2008c].

In total 50 realizations were simulated. Randoms and scatters were simulated but not stored in the list mode output, yielding true coincidences only. Simulation data sets at different noise level were simulated: 150 million and 50 million true coincidences respectively. The simulated data were reconstructed using the Gaussian rotator method with SM $A^{p,v}$ and SM $A^{g,v}$. The reconstruction results were compared with the baseline method and a standard OS-EM using a multi-ray Siddon projector [Verhaeghe et al., 2008].

6.3.7 Experimental Studies

A customized image quality phantom was imaged on the Gemini GS PET/CT. The phantom had a cylindrical shape with 18.6 cm in height and 21.6 cm in diameter. It contained six spheres: four hot (diameters: 9.89 mm, 12.43 mm, 15.43 mm and 19.79 mm) and two cold (diameters: 25.4 mm and 31.8 mm). The spheres were located in a plane about 4.6 cm off-center. The background was filled with 1 mCi ^{18}F-FDG in water. The hot-to-background ratio was 4:1.

The phantom was scanned for 25 minutes with approximately 200 million coincidences collected in list mode with about 16.4 million randoms. The scan data were then binned into the LOR histogram with the randoms subtracted from the dual windows measurement. Normalization was applied onto the raw histogram using an iterative model-based method [Ferreira et al., 2000]. The attenuation map was obtained from the CT scan. Scatter correction was applied by single scatter correction technique [Watson et al., 1997] and the estimated scatter fraction is about 41.4%. The pre-corrected data were reconstructed using the Gaussian rotator method with SM $A^{p,v}$ and SM $A^{g,v}$ and compared with the baseline method and the multi-ray Siddon OS-EM.

6.4 Results

6.4.1 Noiseless Data Studies

Slices of reconstruction examples at the 20th iteration (OS-EM, 22 subsets) are displayed in Fig. 6.5 and Fig. 6.6. Images of the Gaussian rotator method with SM $A^{p,v}$ and SM $A^{g,v}$ are shown in Fig. 6.5a and Fig. 6.5b respectively. The image of the ideal rotator method is depicted in Fig. 6.5c. The profiles extracted through the hot lesions were depicted in Fig. 6.6a and 6.6b. Ringing artifacts were observed at various places, namely the edge of the background, the cold spheres and the hot spheres, as indicated by white arrows. The Gaussian rotator method with $A^{p,v}$ demonstrated the most pronounced artifacts.

The results of the artifact analysis are displayed in Fig. 6.7. The ringing indices for hot lesions (Fig. 6.7a), cold lesions (Fig. 6.7b) and the edge of the background (Fig. 6.7c) were plotted as a function of the iteration number. Each point represents one iteration. The ideal rotator method with $A^{p,pol}$ yielded the least pronounced artifacts. All ringing indices of the three methods showed a tendency to converge upon each other, except for the maximum of the edge of the background for the Gaussian rotator method.

The CRC of the 20th iteration are depicted in Fig. 6.7d. The Gaussian rotator method with $A^{p,v}$ yielded the highest CRC.

6.4.2 Simulation Studies

Slices of reconstruction examples at the 20th iteration (OS-EM, 22 subsets) for the high count study and the low count study are illustrated in Fig. 6.8. The top row is of the high count study and the bottom row is of the low count study. The profiles extracted through hot lesions were depicted in Fig. 6.9 for the high count study (the top row) and the low count study (the bottom row). For reconstruction examples of the high count study (Fig. 6.8a, 6.8c and 6.8e), it can be seen that the ringing artifacts at cold spheres became unnoticeable. The rest artifacts remained present but became irregular in shape, as indicated by white arrows (Fig. 6.8a, 6.8c and 6.8e). The profiles indicate that the ringing artifacts at the edge of the background is negligible compared to noise although visible (Fig. 6.9a and 6.9b). From the reconstruction examples of the low count study (Fig. 6.8b, 6.8d and 6.8f), it can be seen that the ringing artifacts become invisible except for the largest hot lesion. The ringing artifacts at the edge remains visible but can be discarded as well for both the high count and the low count study, as indicated by the profiles in Fig. 6.9c and 6.9d.

The results of the artifacts analysis are summarized in Fig. 6.10 for the high count and the low count study. The ringing indices for hot lesions (Fig. 6.10a and 6.10c) and the edge of the background (Fig. 6.10b and 6.10d) were plotted as a

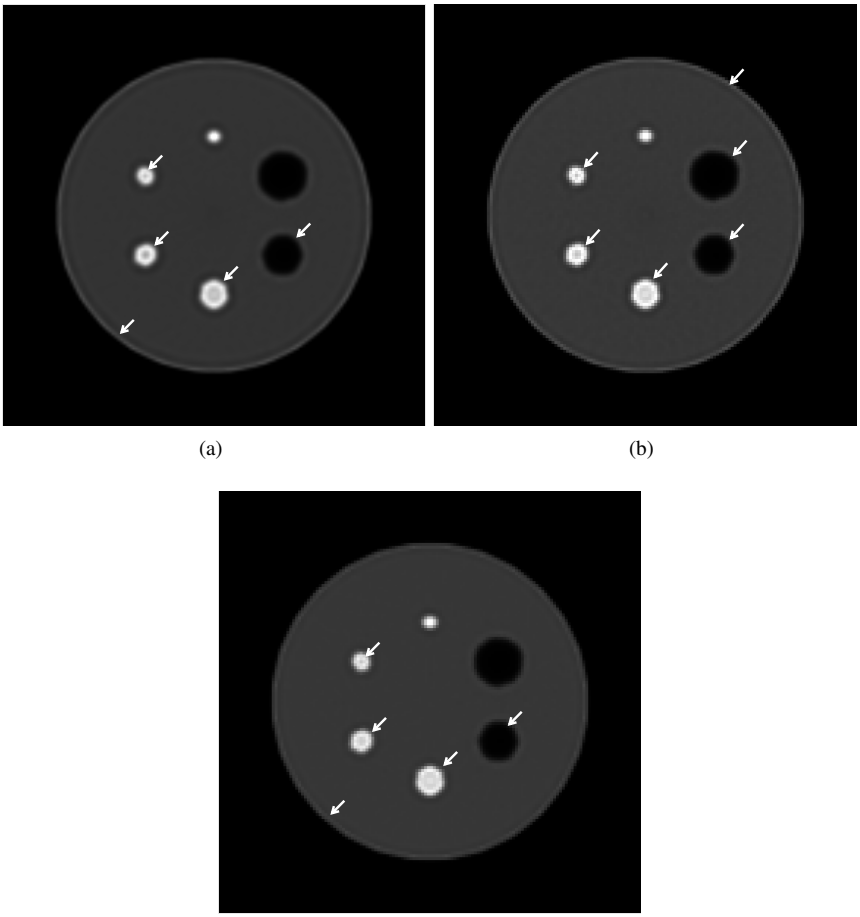

(a) (b)

(c)

Figure 6.5: Artifact illustration with noiseless data (a) Gaussian rotator method with SM $A^{p,v}$. (b) Gaussian rotator method with SM $A^{g,v}$. (c) Ideal rotator method with SM $A^{p,pol}$.

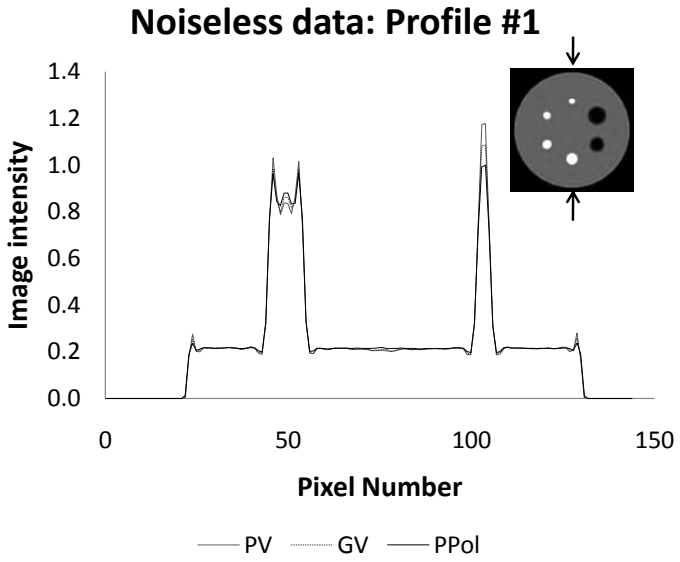

(a)

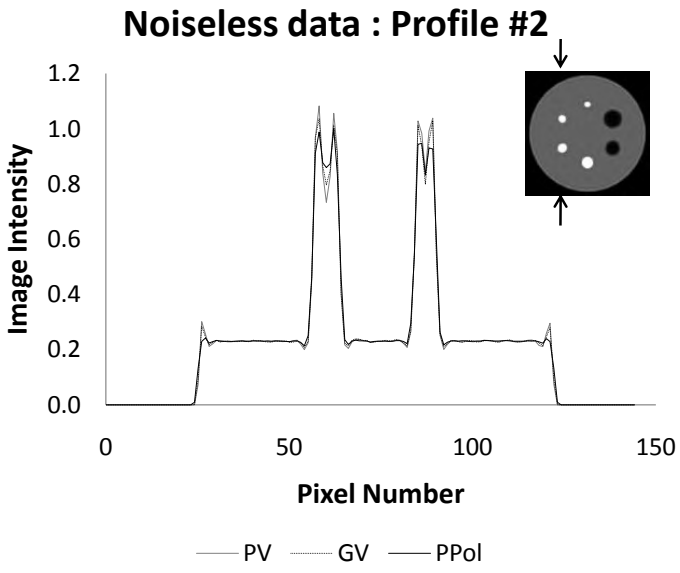

(b)

Figure 6.6: Artifact illustration with noiseless data. (a) and (b) Profiles extracted through hot lesions.

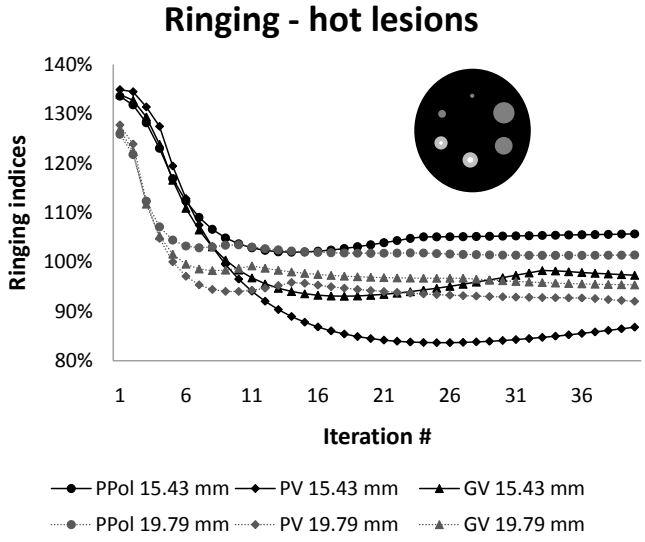

(a)

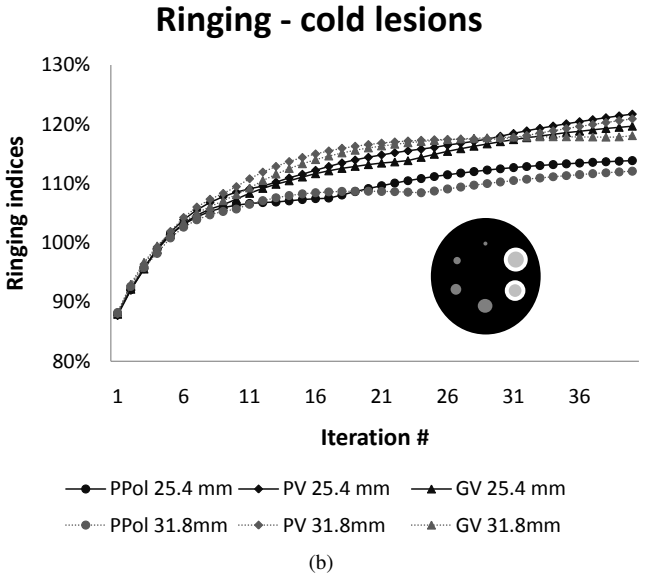

(b)

Figure 6.7: Artifact evaluation indices for different methods, PV: Gaussian rotator method with SM $A^{p,v}$, GV: Gaussian rotator method SM $A^{g,v}$, PPol: ideal rotator method with SM $A^{p,pol}$. (a) Ringing indices for hot lesions. (b) Ringing indices for cold lesions. (c) Ringing indices for the edge of the background. (d) Contrast recovery at 20th iteration.

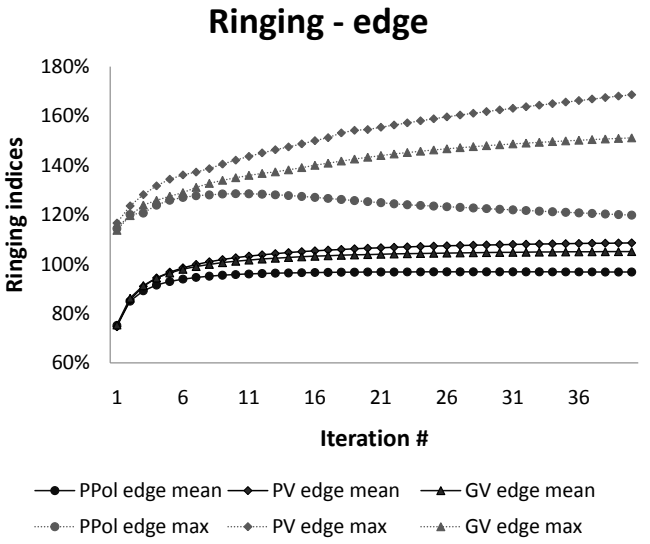

(c)

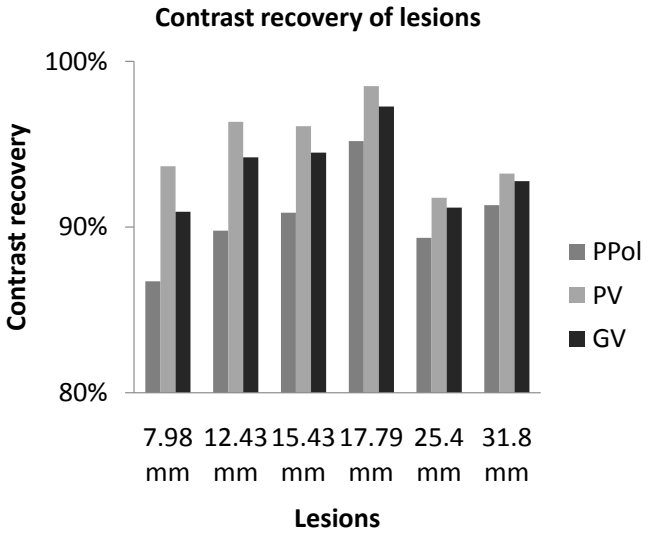

(d)

Figure 6.7: Artifact evaluation indices for different methods, PV: Gaussian rotator method with SM $A^{p,v}$, GV: Gaussian rotator method SM $A^{g,v}$, PPol: ideal rotator method with SM $A^{p,pol}$. (a) Ringing indices for hot lesions. (b) Ringing indices for cold lesions. (c) Ringing indices for the edge of the background. (d) Contrast recovery at 20th iteration.

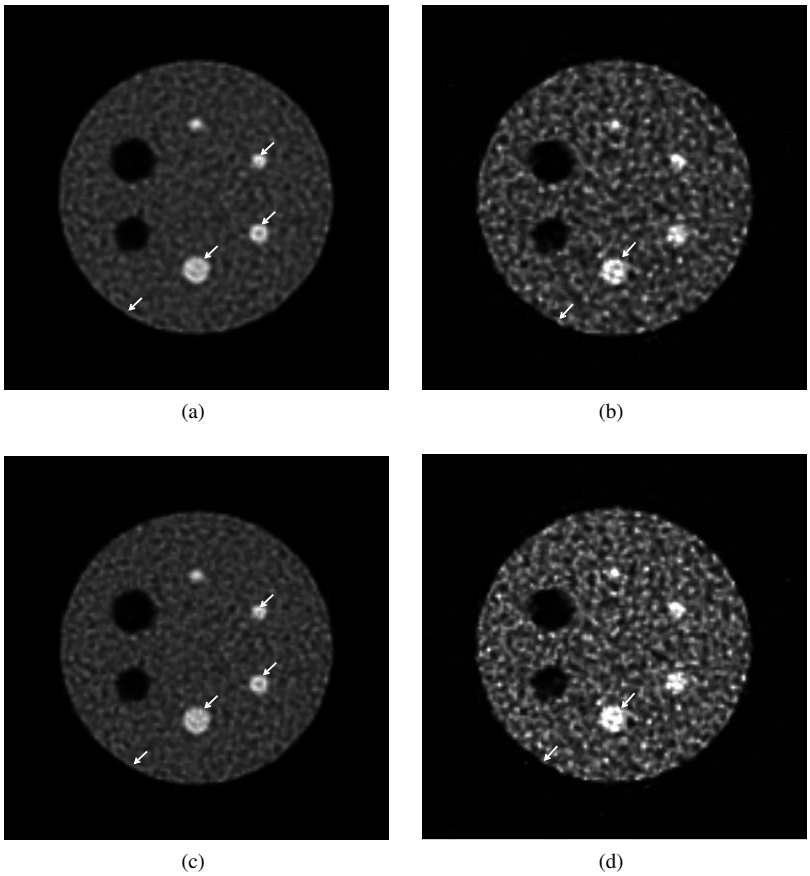

(a) (b)

(c) (d)

Figure 6.8: Artifact depiction in simulation data. Top row is of the high count study and bottom row is of the low count study. (a) Gaussian rotator method with SM $A^{p,v}$ of the high count study. (b) Gaussian rotator method with SM $A^{g,v}$ of the high count study. (c) Ideal rotator method with SM $A^{p,pol}$ of the hight count study. (d) Gaussian rotator method with SM $A^{p,v}$ of the low count study. (e) Gaussian rotator method with SM $A^{g,v}$ of the low count study. (f) Ideal rotator method with SM $A^{p,pol}$ of the low count study.

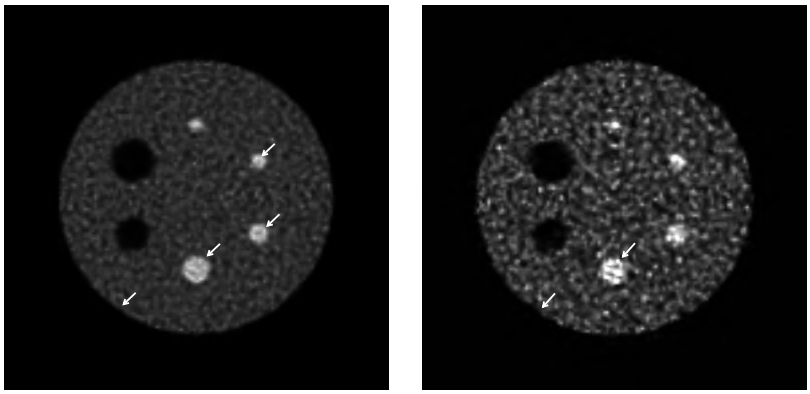

(e) (f)

Figure 6.8: Artifact depiction in simulation data. Top row is of the high count study and bottom row is of the low count study. (a) Gaussian rotator method with SM $A^{p,v}$ of the high count study. (b) Gaussian rotator method with SM $A^{g,v}$ of the high count study. (c) Ideal rotator method with SM $A^{p,pol}$ of the hight count study. (d) Gaussian rotator method with SM $A^{p,v}$ of the low count study. (e) Gaussian rotator method with SM $A^{g,v}$ of the low count study. (f) Ideal rotator method with SM $A^{p,pol}$ of the low count study.

function of the iteration number. Each point represents one iteration. The ringing indices of the high count study and the low count study display similar amplitude. The three methods displayed artifact behaviors with the iteration number.

The CRCs of different methods at the 10th iteration were depicted in Fig. 6.11a for the high count study and Fig. 6.11b for the low count study. The noises of different methods are 19% (Gaussian rotator with $A^{p,v}$), 21% (Gaussian rotator with $A^{g,v}$) and 20% (Ideal rotator with $A^{p,pol}$) and 27% for the multi-ray Siddon method at this iteration in the high count study. The Gaussian rotator method with $A^{p,v}$ showed the highest CRC and the lowest noise. The noises of different methods are 34% (Gaussian rotator with $A^{p,v}$), 38% (Gaussian rotator with $A^{g,v}$) and 35% (Ideal rotator with $A^{p,pol}$) and 46% for the multi-ray Siddon method at this iteration in the high count study. The Gaussian rotator method with $A^{p,v}$ showed the highest CRC and the lowest noise. Monte Carlo-based methods considerably out-performed the standard OS-EM in terms of contrast noise trade-offs in both studies.

6.4.3 Experimental Studies

Slices of reconstruction examples at the 5th iteration (OS-EM, 22 subsets) are displayed in Fig. 6.12. The images of the Gaussian rotator method with SM $A^{p,v}$ and SM $A^{g,v}$ are shown in Fig. 6.12a and Fig. 6.12b. The image of the ideal

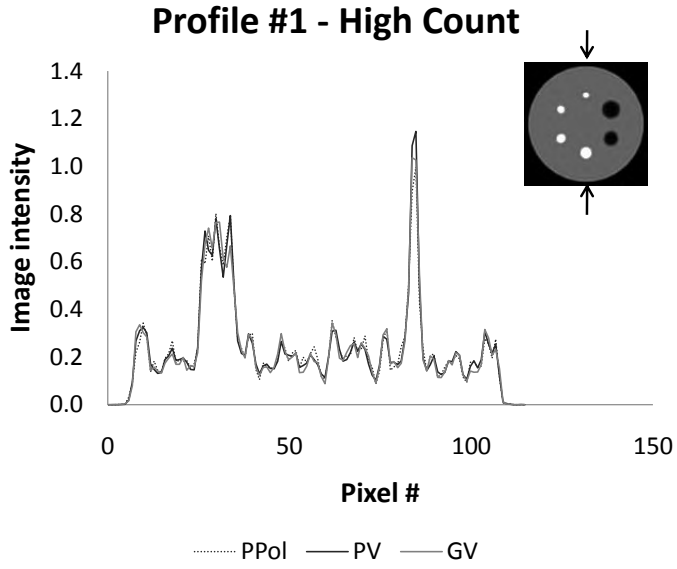

(a)

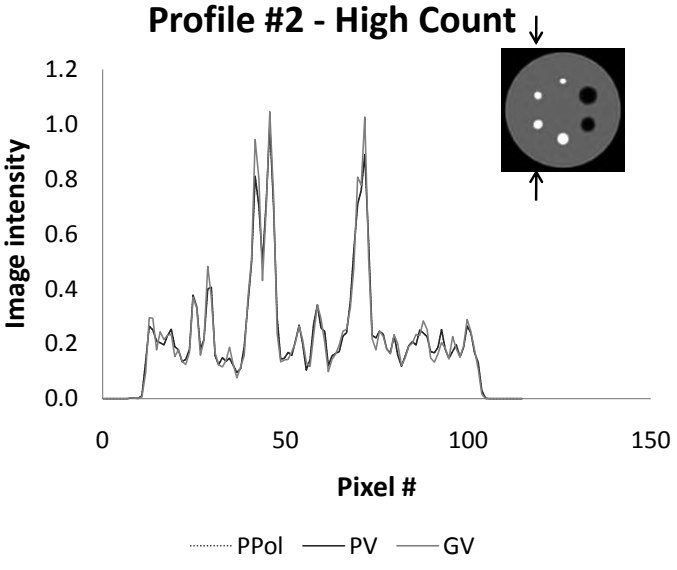

(b)

Figure 6.9: Profile extracted from hot lesions on simulation data. Top row is of high count and bottom row is of low count. (a) and (b) show profiles extracted through hot lesions in the high count study. (c) and (d) depicted profiles extracted through hot lesions in the high count study.

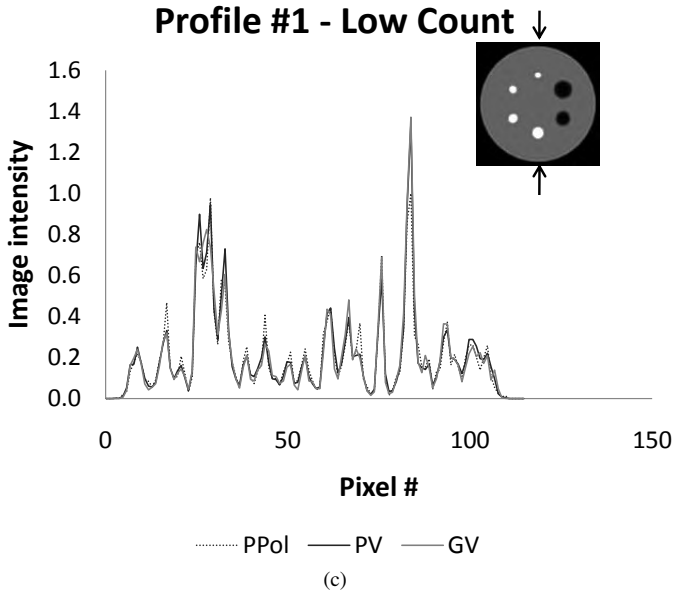

(c)

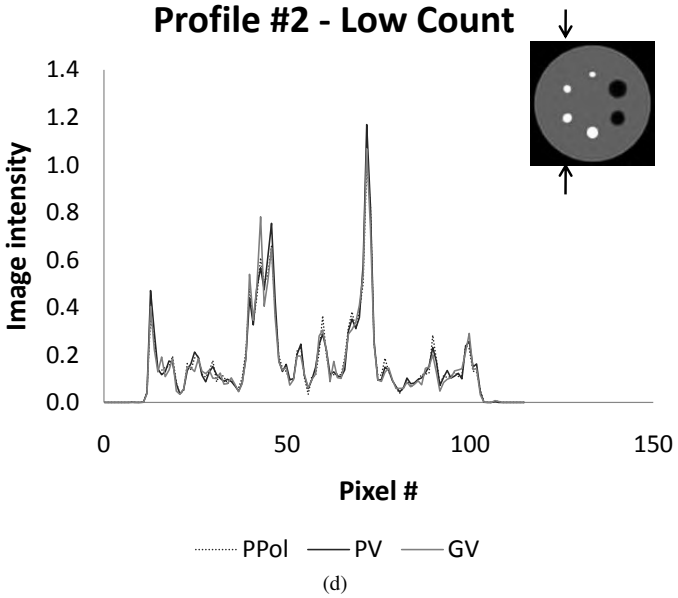

(d)

Figure 6.9: Profile extracted from hot lesions on simulation data. Top row is of high count and bottom row is of low count. (a) and (b) show profiles extracted through hot lesions in the high count study. (c) and (d) depicted profiles extracted through hot lesions in the high count study.

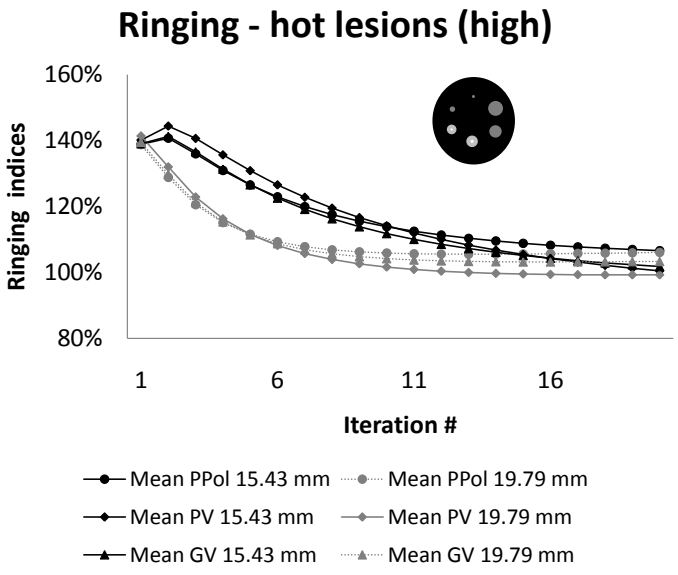

(a)

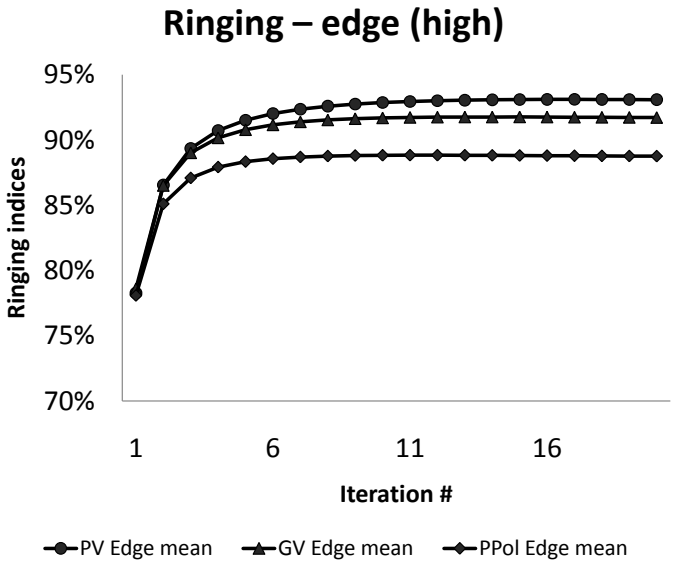

(b)

Figure 6.10: Artifact evaluation indices for different methods (I), PV: Gaussian rotator method with SM $A^{p,v}$, GV: Gaussian rotator method SM $A^{g,v}$, PPol: ideal rotator method with SM $A^{p,pol}$, Sid: the standard OS-EM. Top row is of the high count study. Bottom row is of the low count study. (a) Ringing indices for hot lesions in the high count study. (b) Ringing indices for the edge of the background in the high count study. (c) Ringing indices for hot lesions in the low count study. (d) Ringing indices for the edge of the background in the low count study.

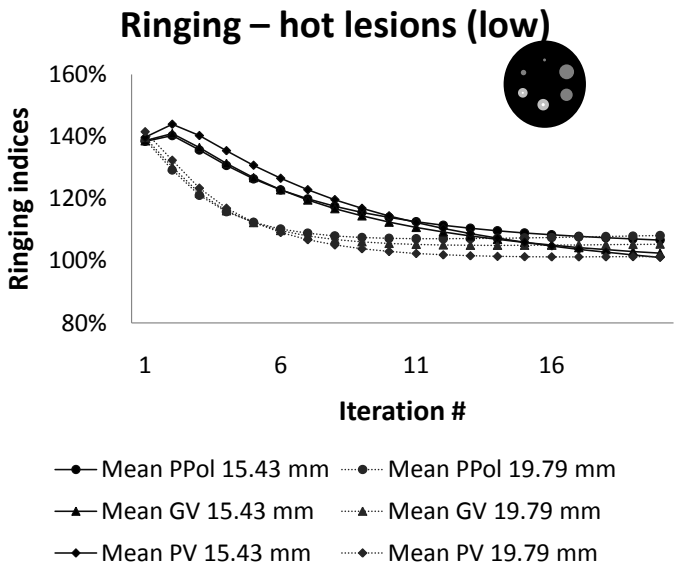

(c)

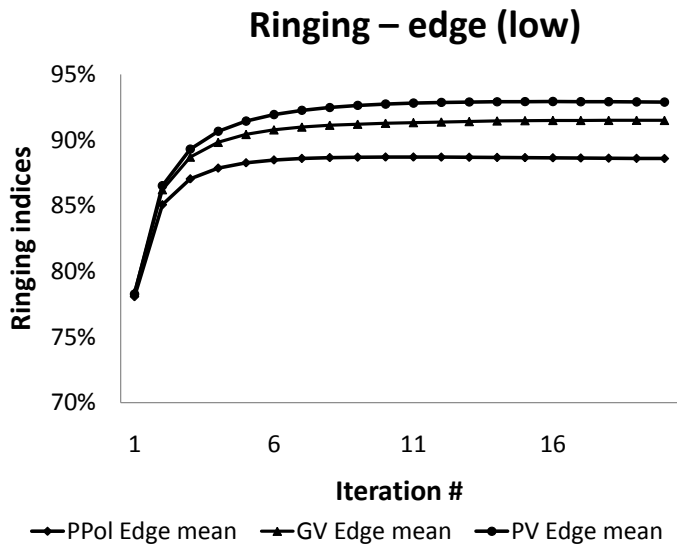

(d)

Figure 6.10: Artifact evaluation indices for different methods (I), PV: Gaussian rotator method with SM $A^{p,v}$, GV: Gaussian rotator method SM $A^{g,v}$, PPol: ideal rotator method with SM $A^{p,pol}$, Sid: the standard OS-EM. Top row is of the high count study. Bottom row is of the low count study. (a) Ringing indices for hot lesions in the high count study. (b) Ringing indices for the edge of the background in the high count study. (c) Ringing indices for hot lesions in the low count study. (d) Ringing indices for the edge of the background in the low count study.

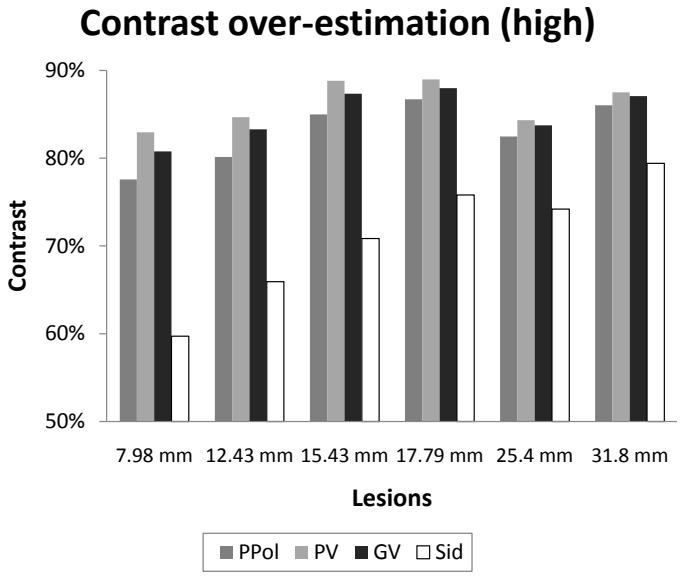

(a)

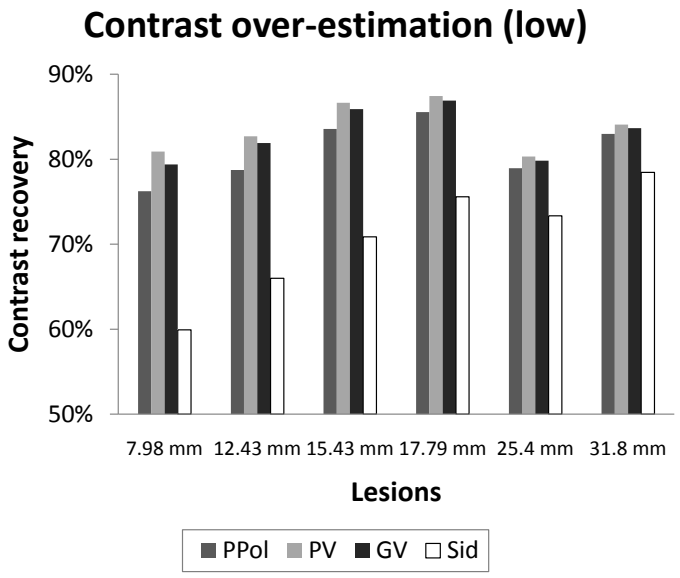

(b)

Figure 6.11: Artifact evaluation indices for different methods (II), PV: Gaussian rotator method with SM $A^{p,v}$, GV: Gaussian rotator method SM $A^{g,v}$, PPol: ideal rotator method with SM $A^{p,pol}$, Sid: the standard OS-EM. Top row is of the high count study. Bottom row is of the low count study. (a) Contrast recovery at the 20th iteration in the high count study. (b) Contrast recovery at the 20th iteration in the low count study.

rotator method is depicted in Fig. 6.12c. The profiles extracted through the largest and smallest hot lesions are depicted in Fig. 6.12d. Only ringing artifacts along the edge and the 19.79 mm hot sphere remain visible. The profiles indicate that the ringing artifacts at the edge of the background are negligible compared to noise.

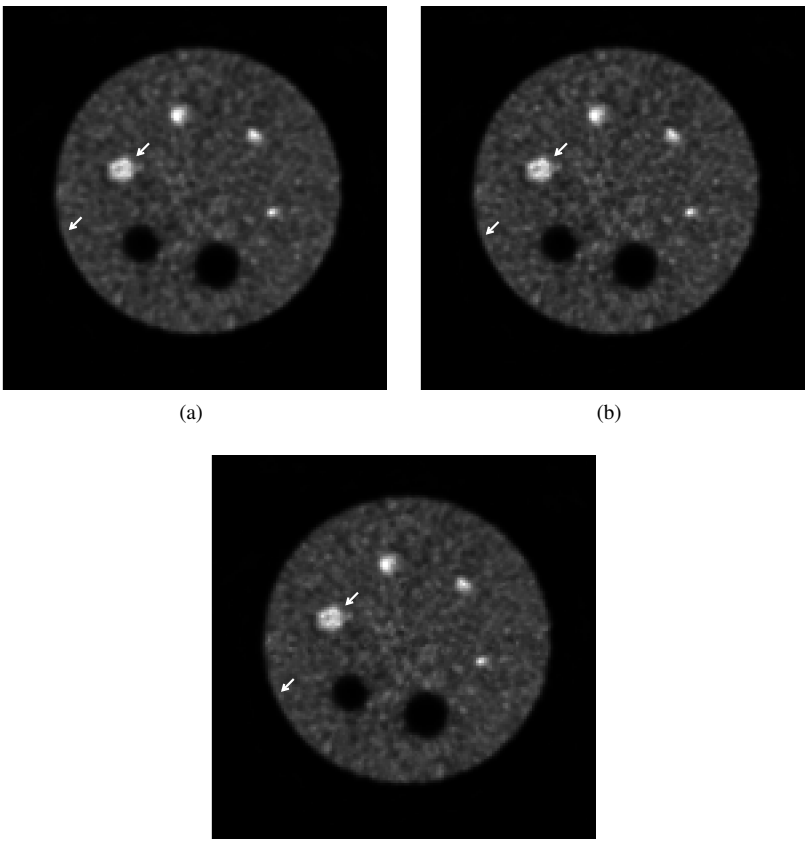

(a) (b)

(c)

Figure 6.12: Artifact depiction in acquired data (a) Gaussian rotator method with SM $A^{p,v}$. (b) Gaussian rotator method SM $A^{g,v}$. (c) Ideal rotator method with SM $A^{p,pol}$. (d) Profiles extracted through the largest and smallest hot lesions..

The results of the artifact analysis are summarized in Fig. 6.13. The ringing indices for hot lesions and the edge of the background were plotted as a function of the iteration number (till the 20th iteration), as shown in Fig. 6.13a and Fig. 6.13b. Each point represents one iteration.

The CRCs of different methods at the 5th iteration are depicted in Fig. 6.13c. The CVs of different methods are 32% (Gaussian rotator with $A^{p,v}$), 35% (Gaus-

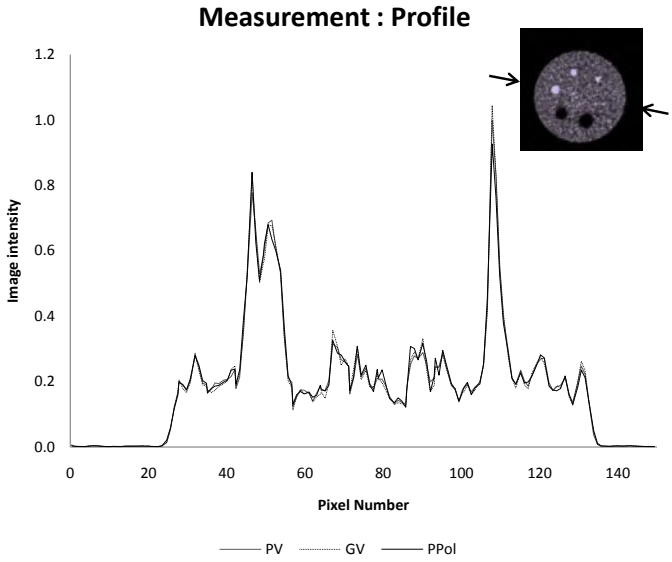

(d)

Figure 6.12: Artifact depiction in acquired data (a) Gaussian rotator method with SM $A^{p,v}$. (b) Gaussian rotator method SM $A^{g,v}$. (c) Ideal rotator method with SM $A^{p,pol}$. (d) Profiles extracted through the largest and smallest hot lesions..

sian rotator with $A^{g,v}$) and 33% (Ideal rotator with $A^{p,pol}$) and 46% for the multi-ray Siddon method. Monte Carlo-based methods considerably outperformed the standard OS-EM in terms of contrast noise trade-offs. The Gaussian rotator method with $A^{p,v}$ showed the highest CRC and the lowest CV.

6.5 Discussion and future work

The polar-pixel images were converted to voxel images in the CRC study. A slight blurring may exist in the Polar-to-Cartesian conversion, leading to a slightly under-estimated contrast recovery in the baseline method. This under-estimation was discarded in this chapter because this error was systematic and marginal.

Ringing artifacts were detected in the baseline method (the ideal rotator method), which is due to the Gibbs phenomenon [Reader et al., 2003] and is inevitable [Snyder et al., 1987, Qi et al., 1998, Reader et al., 2003, Panin et al., 2006a]. For this reason, an under-compensated system model was suggested to avoid artifacts [Reader et al., 2003, Sureau et al., 2008].

The noiseless study revealed that the pronounced bias errors at sharp image intensity transitions are caused by ringing artifacts. In addition, the noiseless data study suggested that other origins of artifacts exist in the Gaussian rotator method. More pronounced ringing artifacts were observed in Gaussian rotator reconstructions as compared with the baseline method. This phenomenon indicated that the ringing artifacts in this method were not only due to Gibbs effects but also due to the blurring rotator that further blurred the system response kernels. Similar results have been reported in image space resolution modeling [Reader et al., 2003, Sureau et al., 2008]. The $A^{p,v}$ reconstructions showed more pronounced artifacts compared to the $A^{g,v}$ ones. This result indicates that blurrier system responses lead to more pronounced artifacts because $A^{p,v}$ is blurrier than $A^{g,v}$ due to the modeling of the positron range and acolinearity.

The effect of noise was investigated by studying the simulation data. In the presence of noise, the artifacts of the Gaussian rotator method become visually less pronounced or even undetectable because the integrity of the ringing is damaged by noise, i.e., the ringing at cold lesions in the high count study and the hot lesions in the low count study (Fig. 6.8). The high count study and low count study show that the nosier the data are, the less pronounced the artifacts appear. This phenomenon was previously reported by Panin et al. [Panin et al., 2006a]. The quantitative study shows that the ringing indices remain the same, but are insignificant for quantitative studies because the means of artifact ROIs are greater than the means of the corresponding lesions. These findings indicate that the noise artifacts are the dominant artifacts in a clinical PET scan.

Correlation between the types of artifacts and the lesions size was observed. For large hot lesions (e.g. the 15.43 mm hot lesion), ringing artifacts were visible,

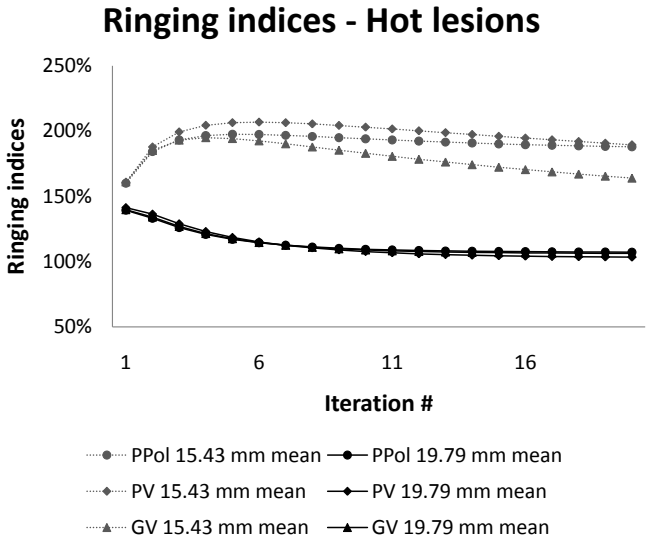

(a)

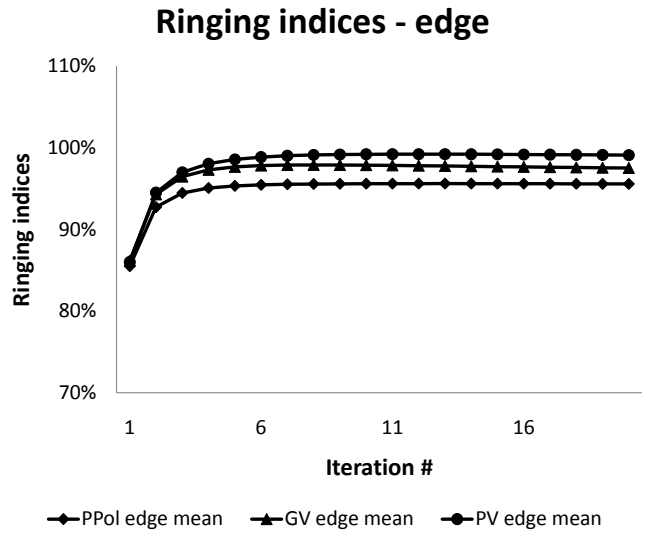

(b)

Figure 6.13: Artifact evaluation indices for different methods, PV: Gaussian rotator method with SM $A^{p,v}$, GV: Gaussian rotator method SM $A^{g,v}$, PPol: ideal rotator method with SM $A^{p,pol}$, Sid: the standard OS-EM. (a) Ringing indices for hot lesions. (b) Ringing indices for the edge of the background. (c) Contrast recovery at the 5th iteration.

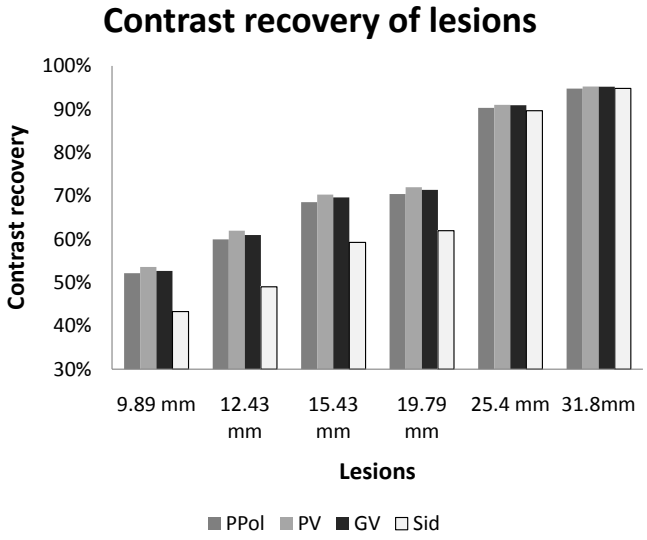

(c)

Figure 6.13: Artifact evaluation indices for different methods, PV: Gaussian rotator method with SM $A^{p,v}$, GV: Gaussian rotator method SM $A^{g,v}$, PPol: ideal rotator method with SM $A^{p,pol}$, Sid: the standard OS-EM. (a) Ringing indices for hot lesions. (b) Ringing indices for the edge of the background. (c) Contrast recovery at the 5th iteration.

but were less pronounced than noise artifacts. Virtually no artifacts other than taper artifacts were detected in small lesions. This finding indicates that the partial volume effects dominate for small lesions, while noise artifacts dominate for large lesions. Cold lesions showed no pronounced artifacts.

The noiseless and Monte Carlo studies showed that "higher" CRC can be achieved by the Gaussian rotator method as compared to the baseline method, particularly for small hot spheres. These improvements are spurious and are caused by the bias error (overshoot and undershoot) induced by the ringing artifacts. However, the CRC cannot reach 100% due to partial volume effects, particularly for small lesions and the limited over-compensation of resolution loss in our study. This phenomenon indicates that the partial volume effects remain important even with resolution compensation. The artifacts are also tolerable due to the predominant presence of noise in PET. This bias error also induces artificially improved resolution when an over-estimated system response kernel is used [Fessler, 2010]. The slightly improved contrast for small spheres may increase detection of small lesions, which is very important in improving the patient survival rate [Kim et al., 2005]. Moderate ringing in large lesions might facilitate tumor volume delineation [Mitchell and Netravali, 1988]; improved contrast recovery yields slightly better quantification. These improvements are beneficial for treatment planning or treatment response monitoring in radiation oncology [Wiant et al., 2010]. However, this improvement might cause problems in absolute quantification, e.g. overestimating the SUV, because the over-estimation of the width of the response kernel is difficult to quantify. This issue becomes more complicated in practice due to simplifications in resolution modeling and the fact that the true detector response kernel is never known.

In the validation using measured data, we observed less pronounced artifacts (especially for ringing at the 15.43 mm hot lesion and along the edge of the background), as compared to the high count Monte Carlo study. Noise contributes to this improvement because the noise equivalent count is about 58 million trues. This explanation is consistent with the low count Monte Carlo study. Non-perfect correction techniques might contribute this improvement because the introduced noise and bias may disguise these artifacts. This improvement could be attributed to the fact that blurring of system responses was under-estimated by the Monte Carlo simulator due to factors that are not included in the scanner model, namely pulse pile-up, optical photon spreading in crystal and light guide and the Anger logic positioning determination. In physical world, the system responses are even blurrier in a warm background than in the air and may vary with different intensities of the background. Our scanner model is not validated against the physical scanner yet, which complicates the analysis. However, the low count study suggested that these factors are minor.

We employed the 2-mm FWHM Gaussian rotator to compensate for the res-

olution loss caused by the positron range and acolinearity in the Gaussian rotator method using SM $A^{g,v}$. The result indicated that the blurring of the Gaussian rotator can be employed to compensate for resolution loss in projection space. Over-compensation of the resolution loss was detected because the method employing $A^{g,v}$ yielded more pronounced ringing artifacts than with the baseline method. This result did not agree with the theoretical analysis described in section 6.2.2, which predicted more blurring than the 2 mm FWHM Gaussian kernel for the size of the imaged phantom (Fig. 6.2c). We investigated this issue by simulating the point spread function (PSF) with only the positron range and acolinearity for the target scanner. The FWHM of the PSF is considerably smaller than 2 mm when OS-EM is used to reconstruct the projection data. This finding explains this discrepancy because the resolution kernel in image space modeling is algorithm-dependent [Cloquet et al., 2009]. Under certain conditions, i.e. lack of computational resources, the Gaussian rotator method with SM $A^{g,v}$ could be a better choice. The SM simulation efficiency was significantly improved because time consuming positron tracking was avoided.

Our method retained the simplicity of using voxels while enjoying the same symmetry handling properties of a cylindrical scanner as a radial symmetry object parameterization, namely, polar pixels. Consequently, measurement-derived system matrix could be directly incorporated in our method because, to the best of our knowledge, all established methods using measured system responses were implemented on the voxel discretization [Alessio et al., 2005, Panin et al., 2006a, Tohme and Qi, 2009]. In addition, the rotator-based method would be preferred when an accurate system response is impractical by either simulation or measurement. For instance, measuring system responses for short-lived isotopes, namely ^{82}Rb and ^{15}O, is not feasible in practice as a long-lived positron emitter with proper positron range does not exist. The "missing" part could be compensated by adjusting the blurring of the Gaussian rotator at no cost on symmetry handling. This hypothesis will be investigated in the future. Otherwise, the resolution loss is over-compensated by the rotator. The consequences of such over-compensation in resolution loss could require more studies with clinical data. In addition, the techniques on improvement of the simulation accuracy will be investigated and the improved scanner model will be validated against the physical scanner in the future.

6.6 Conclusion and original contributions

We found that the ringing artifacts were composed of the Gibbs ringing and the ringing caused by the over-compensation in resolution modeling. Image quality improvements in terms of contrast noise trade-offs were detected by using an over-blurred system response kernel, i.e. a wider kernel. The artifacts were tolerable in

practice with a moderately over-compensated system model. Our study suggested better quantitative results can be achieved with the moderately over-compensated system model, at least when the locations of the lesions are known. This finding is significant for treatment planning or treatment response monitoring in radiation oncology.

In this work, we investigated the origins of the ringing artifacts in the rotator-based algorithm and characterized the artifacts quantitatively. This study revealed that the ringing artifacts can be caused by an over-blurred system response kernel in addition to the Gibbs effects. It also suggested that the bias caused by the ringing artifacts is invisible for emission tomography. Most important of all, the bias of the ringing artifacts enhanced the image contrast, particularly for small hot lesions. This finding is significant for treatment planning or treatment response monitoring in radiation oncology where the locations of the lesions are already known. This study leads to one A1 journal publication [Zhang et al., 2010d] and book chapter in preparation.

Chapter 7

General Conclusion

This chapter contains a summary of the principle contribution of this work. In addition, some interesting topics are listed for future study.

7.1 Main conclusions

This work discusses the resolution modeling of PET, particularly system matrix generated with Monte Carlo or measured point sources. We focused on several aspects of this problem:

- Fast Monte Carlo simulation of PET (various particular VRTs for resolution modeling).
- The choice of basis functions and reconstruction algorithms, e.g. their symmetry properties
- Ringing artifacts occurring at sharp image intensity transitions during reconstruction with an accurate system model
- PSF modeling using measured point source data

These aspects are not mutually exclusive. Rather they are closely linked. Due to the dimensions of the problem, a fast Monte Carlo simulator is necessary. However even dedicated Monte Carlo simulators are still too time-consuming for the resolution model of a state-of-the-art whole-body PET scanner. Usually, this problem is solved by employing the symmetries of the PET scanner to reduce the redundancy of the system model. The number of symmetries that can be used depends on the basis functions and reconstruction algorithms. In a radially symmetric object parameterization, more symmetry can be used compared to a Cartesian discretization. However, a rotator may use radial symmetries in a Cartesian discretization

without using a radially symmetric object parameterization. A potential problem with this approach is that a rotator may alter the system model. We found that the rotator made the ringing artifacts more pronounced in an accurate system model. For a rotator with moderate and predictable blurring, the contrast is enhanced with ringing artifacts that are less pronounced than the noise artifacts. To exploit this effect, an experimental data-based PSF model is the best candidate. Thus, we initially investigated the feasibility of a measured PSF model in the rotator-based algorithm.

The simulation efficiency for resolution modeling in PET can be significantly improved with a set of simple VRTs.
In chapter 3, we described a set of simple VRTs for PET simulation, particularly for resolution modeling. A system model must be independent of object-dependent factors, variation in the crystal alignment, uniformity, electronics properties, and different acquisition parameters. With these constraints, we assumed that the simulation is time-independent and object-independent. A set of VRTs (such as polar angle biasing, hit-testing, positron history reuse, forced passing energy window, and fictitious transport in crystal array) were implemented using egs_pet. The transport parameters were optimized for the specific task. Combining all the above techniques, the simulation efficiency was improved fifteen-fold compared to an analog simulation without system symmetries. This speedup allows resolution modeling for a state-of-the-art PET scanner with a smaller cluster.

Rotationally symmetrical basis functions are advantageous for reducing redundancies in a system model of a cylindrical PET scanner
In chapter 4 and section 6.2.1 of chapter 6, we investigated different basis functions and applied them to a Monte Carlo-based system model. These basis functions are based on Cartesian discretization (cubic voxels) and polar-pixels. The polar-pixels are rotationally symmetric. Thus, the inherent rotational symmetries in a cylindrical PET scanner can be used without additional techniques. And the redundancy of a system model can be reduced by storing the base-symmetry set. The polar-pixels may be problematic for a perfectly cylindrical PET scanner, because the over-segmenting the transverse FOV may lead to very small pixels at the center of the FOV. Thus, the voxel-based or voxel-grid-based approaches remains an interesting topic in resolution modeling.

A proper rotator helps to achieve rotational symmetries in a Cartesian discretization
In contrast to a rotationally symmetric basis function, limited symmetries can be utilized in a Cartesian discretization (i.e. the voxels). In chapter 4, we demonstrated that the Cartesian object parameterization shares the same rotational sym-

metries as the polar-pixels and the strip blobs. This approach is more flexible than the other two approaches. For example, this approach can use all rotational symmetries, the FOV is segmented by non-overlapping voxels, and the voxels facilitate an experimentally derived system model.

Perfect rotators can be implemented with the rotationally symmetrical basis functions.
The rotational symmetry of the polar-pixels implies that the image represented by the polar-pixels can be perfectly rotated to certain quantized angular positions where the rotational symmetry occurs. In chapter 6, we demonstrated one such polar-pixel implementation and observed considerably fewer ringing artifacts. An ideal rotator can be implemented with any object parameterization with rotational symmetry.

In resolution modeling, the blurring (in either projection or image space) estimated by an algorithm is better to use in the same algorithm
In chapter 6, we compared the analytical modeling of the positron range and acolinearity to a full Monte Carlo-based model using an ideal rotator. We found that the algorithm using the analytical model yielded a blurrier system response kernel than the Monte Carlo model, where the blurring kernel was estimated by OS-EM. Our simulation showed that the blurring of the positron range and acolinearity is lower than that reported in literature when ML-EM was employed. Thus, the blurring kernel of the positron range and acolinearity is best estimated by an ML-EM/OS-EM algorithm for a perfectly matched blurring kernel if the blurring kernel must be applied to an ML-EM/OS-EM algorithm. The reason is that the blurring is highly algorithm-dependent. This conclusion is consistent with other studies using resolution modeling in the image space.

The ringing artifacts in our studies are mainly caused by the over-blurred system response kernels and the Gibbs effects
Although a rotator makes the rotational symmetries available in a Cartesian discretization, ringing artifacts are a drawback. In chapter 6, we characterized the ringing artifacts that occurred in our rotator-based reconstruction using an accurate system model. An ideal rotator-based approach was implemented as the gold standard. We found that the ideal rotator-based approach also showed slight ringing artifacts at sharp transitions of the image intensity. According to the definition, these ringing artifacts belong to the well-known family of Gibbs effects. The blurring rotator-based approach exhibited more pronounced ringing artifacts than those of the ideal rotator-based approach. This finding indicates that the ringing in our reconstruction is mainly caused by the rotator, which further over-blurred the system response kernels.

The azimuthal independence assumption is valid for the target PET scanner: Philips Gemini GS and her sibling models
In our studies in chapter 5, we found that all 2-D slices were properly reconstructed. Azimuthal independence is a very important feature in resolution modeling because all of the rotational symmetries can be used in the system model when this assumption holds.

Axial blurring is a minor effect, but remains attractive in resolution compensation for PET
In chapter 5, our studies revealed the importance of modeling axial blurring. In axial modeling, the axial resolution has been significantly improved. The contrast noise trade-off study showed that both the contrast recovery and noise reduction were not significantly improved. However, the improvement in the smaller lesions was greater than the larger lesions. This finding suggests that axial blurring is a minor effect in terms of contrast noise trade-offs but remains attractive because the contrast recovery of small lesions has been improved with this modeling.

Resolution compensation for fully 3-D PET reconstruction is practical
Employing resolution compensation in fully 3-D reconstruction of human PET are hindered by two challenges. The first challenge is the expensive computational cost of generating data for resolution modeling. This issue has been addressed by VRTs and a light-weight Monte Carlo simulator or by measuring PSFs on a sparse grid. For both approaches, inherent symmetries, particularly the radial symmetries, in a scanner can be utilized to reduce the storage requirement of a system model, which is the second challenge. In addition, parameterization and factorized matrix techniques can be used to further downsize the storage requirement of the system model. In chapter 4 and 5, we have demonstrated that it is practical to apply resolution compensation for image reconstruction of fully 3-D, whole-body human PET scanners. Particularly, in chapter 5, we have achieved to a system model of 250 Mb with considerable image quality improvement.

Resolution compensation improves reconstruction considerably
In our studies, we observed that the resolution and contrast noise trade-offs have been improved significantly. In the reconstruction with resolution compensation, the FWHM becomes approximately half of the FWHM without resolution modeling for a point source at the center of the FOV. With resolution compensation, the spatial resolution also becomes uniform across the entire FOV. For an extended source study, the contrast recovery for hot and cold lesions have been significantly improved compared to a reconstruction without resolution compensation. In addition, the noise has been reduced considerably. Thus, resolution modeling also improves the SNR, which indicates that it may reduce the patient scan time similar to what TOF does.

7.2 Future work

For Monte Carlo simulation, it would be interesting to investigate some advanced VRTs (e.g. using a pre-commutated or experimentally measured PDF to further improve the simulation efficiency). For the positron physics, a "condenser" history technique could be used by building spectra of the positron ranges of different materials. For the detector physics, the detector responses could be pre-calculated or measured for the photons with the energy of interest.

For the Monte Carlo-based resolution modeling techniques, it would be interesting to implement an ideal rotator for other rotationally symmetric basis functions such as the generalized natural pixels and strip blobs. Additionally, as suggested by the preliminary results of the experiment-based resolution modeling, the Monte Carlo-based approach can avoid modeling the detector block effects to further improve the simulation efficiency and reduce the redundancy in the system model if the readout logic can be accurately simulated for the Philips Gemini GS PET scanner.

For the experiment-based resolution modeling, our approach allows different effects to be added progressively and more accurate PSF modeling. These effects include solid angle effect, axially variant radial blurring, axial blurring, and some image space effects (e.g. the positron range of ^{82}Rb). It would be interesting to compare the effects of different factors on the image quality and derive an optimal system model with a balanced computational complexity and image quality. In addition, it would be also interesting to include an image space PSF modeling technqiues in the investigation of an optimal system model.

For reconstruction with resolution compensation, it is also interesting to including some clinical studies to evaluate our method, particularly to investigate the effects of the blurring of the rotator. More clinical relevent FOMs may be used to evaluate the effects of over-blurring. The ideal rotator method can also be used as the gold standard. Moreover, employing GP-GPUs to speed up both the reconstruction and Monte Carlo simulation would also be very interesting.

In the future, a patient-specific system model would be preferred to maximize the physical performance of an existing scanner. The object-dependent factors, namely, positron range, object scattering and attenuation can be modeled by a Monte Carlo simulator. The detector response part could use the experimental resolution modeling technique. The computational cost and storage requirement of the patient-specific system model could be considerably reduced through these techniques.

References

[Accorsi et al., 2004] Accorsi, R., Adam, L.-E., Werner, M. E., and Karp, J. S. (2004). Optimization of a fully 3D single scatter simulation algorithm for 3D PET. *Physics in Medicine and Biology*, 49(12):2577.

[AH and AC, 1984] AH, A. and AC, K. (1984). Simultaneous Algebraic Reconstruction Technique (SART): A superior implementation of the ART algorithm. *Ultrasonic Imaging*, 6(1):81 – 94.

[Alessio et al., 2005] Alessio, A. M., Kinahan, P. E., Harrison, R., and Lewellen, T. K. (2005). Measured spatially variant system response for PET image reconstruction. *IEEE Nucl. Sci. Symp. Conf. Record*, 4:1001–1013.

[Alessio and MacDonald, 2008] Alessio, A. M. and MacDonald, L. (2008). Spatially variant positron range modeling derived from CT for PET image reconstruction. *IEEE Nucl. Sci. Symp. Conf. Record*, M03-8:3637–40.

[Alessio et al., 2010] Alessio, A. M., Stearns, C. W., Tong, S., Ross, S. G., Kohlmyer, S., Ganin, A., and Kinahan, P. E. (2010). Application and Evaluation of a Measured Spatially Variant System Model for PET Image Reconstruction. *IEEE Trans. Med. Imag.*, 29(3):938–949.

[Ansorge, 2007] Ansorge, R. (2007). List mode 3D PET reconstruction using an exact system matrix and polar voxels. In *Nuclear Science Symposium Conference Record, 2007. NSS '07. IEEE*, volume 5, pages 3454 –3457.

[Badawi et al., 1999] Badawi, R. D., Miller, M. P., Bailey, D. L., and Marsden, P. K. (1999). Randoms variance reduction in 3D PET. *Physics in Medicine and Biology*, 44(4):941–954.

[Bai et al., 2005] Bai, B., Laforest, R., Smith, A., and Leahy, R. (2005). Evaluation of MAP image reconstruction with positron range modeling for 3D PET. In *Nuclear Science Symposium Conference Record, 2005 IEEE*, volume 5, pages 2686 –2689.

[Bailey et al., 2003] Bailey, D., Townsend, D., Valk, P., and Maisey, M. N. (2003). *Positron Emission Tomography: Basic Sciences*. Elsevier Academic Press, 525 B Street, Suite 1900, San Diego, California 92101-4495, USA.

[Balachandran et al., 1985] Balachandran, S., McGuire, L., Flanigan, S., Shah, H., and Boyd, C. M. (1985). Bremsstrahlung imaging after 32P treatment for residual suprasellar cyst. *International Journal of Nuclear Medicine and Biology*, 12(3):215 – 219, 221.

[Barret et al., 2005] Barret, O., Carpenter, T. A., Clark, J. C., Ansorge, R. E., and Fryer, T. D. (2005). Monte Carlo simulation and scatter correction of the GE Advance PET scanner with SimSET and Geant4. *Phys. Med. Biol.*, 50(3):4823–4840.

[Bertero and Boccacci, 1998] Bertero, M. and Boccacci, P. (1998). *Introduction to inverse problems in imaging*. Institute of Physics Publishing, Institute of Physics Publishing, Dirac House, Temple Back, Bristol BSI 6BE, UK.

[Bielajew and Rogers, 2010] Bielajew, A. F. and Rogers, D. W. O. (2010). Variance Reduction Techniques. Technical Report PRIS_0396, National Research Council of Canada.

[Binkley, 1992] Binkley, D. (1992). Optimization of scintillation-detector timing systems using Monte Carlo analysis. In *Nuclear Science Symposium and Medical Imaging Conference, 1992., Conference Record of the 1992 IEEE*, pages 263 –265 vol.1.

[Brankov et al., 2004] Brankov, J., Yang, Y., and Wernick, M. (2004). Tomographic image reconstruction based on a content-adaptive mesh model. *Medical Imaging, IEEE Transactions on*, 23(2):202 –212.

[Brown, 1979] Brown, K. Q. (1979). Voronoi diagrams from convex hulls. *Information Processing Letters*, 9(5):2238.

[Buonocore et al., 1981] Buonocore, M., Brody, W., and Macovski, A. (1981). A natural pixel decomposition for two-dimensional image reconstruction. *IEEE Trans Biomed Eng.*, 28(2):69–78.

[Buvat and Castiglioni, 2002] Buvat, I. and Castiglioni, I. (2002). Monte Carlo simulations in SPET and PET. *Q J NUCL MED*, 46(4):48–61.

[Buvat and Lazaro, 2006] Buvat, I. and Lazaro, D. (2006). Monte Carlo simulations in emission tomography and GATE: An overview. *Nucl. Instruments and Methods in Phys. Research A*, 569:323–329.

[Casey and Hoffman, 1986] Casey, M. E. and Hoffman, E. J. (1986). Quantification in Positron Emission Computed Tomography: 7. A technique to reduce noise in accidental coincidence measurements and coincidence efficiency calibration. *J. comput. Assist. Tomogr.*, 10:845–850.

[Catana et al., 2010] Catana, C., van der Kouwe, A., Benner, T., Michel, C. J., Hamm, M., Fenchel, M., Fischl, B., Rosen, B., Schmand, M., and Sorensen, A. G. (2010). Toward Implementing an MRI-Based PET Attenuation-Correction Method for Neurologic Studies on the MR-PET Brain Prototype. *J Nucl Med*, 51(9):1431–1438.

[Chaudhari et al., 2008] Chaudhari, A. J., Joshi, A. A., Bowen, S. L., Leahy, R. M., Cherry, S. R., and Badawi, R. D. (2008). Crystal identification in positron emission tomography using nonrigid registration to a Fourier-based template. *Physics in Medicine and Biology*, 53(18):5011.

[Chen et al., 2005] Chen, Y.-C., Furenlid, L., Wilson, D., and Barrett, H. (2005). Calibration of Scintillation Cameras and Pinhole SPECT Imaging Systems. In Kupinski, M. A. and Barrett, H. H., editors, *Small-Animal Spect Imaging*, pages 195–201. Springer US.

[Cherry et al., 1995] Cherry, S., Shao, Y., Tornai, M., Siegel, S., Ricci, A., and Phelps, M. (1995). Collection of scintillation light from small BGO crystals. *Nuclear Science, IEEE Transactions on*, 42(4):1058 –1063.

[Cherry et al., 2003] Cherry, S. R., Sorenson, J. A., and Phelps, M. E. (2003). *Physics in Nuclear Medicine*. Elsevier, Philadelphia, PA.

[Choong, 2009] Choong, W.-S. (2009). The timing resolution of scintillation-detector systems: Monte Carlo analysis. *Physics in Medicine and Biology*, 54(21):6495.

[Cloquet et al., 2009] Cloquet, C., Sureau, F., Defrise, M., Simaeys, G. V., Trotta, N., and Goldman, S. (2009). Space-variant resolution modelling for list-mode reconstruction on the Philips Gemini 16 Power. In *Fully 3D Imag. Recon. in Radi. and Nucl. Med.*, pages 199–202.

[Conti et al., 2009] Conti, M., Eriksson, L., Rothfuss, H., and Melcher, C. (2009). Comparison of Fast Scintillators With TOF PET Potential. *Nuclear Science, IEEE Transactions on*, 56(3):926 –933.

[Cramer, 1977] Cramer, S. (1977). Application of the Fictitious Scattering Radiation Transport Model for Deep-Penetration Monte Carlo Calculations. Technical Report ORNL/TM-4880, Oak Ridge National Laboratory.

[Derenzo, 1981] Derenzo, S. E. (1981). Monte Carlo Calculations of the Detection Efficiency of Arrays of Nai(Tl), Bgo, Csf, Ge, and Plastic Detectors for 511 Kev Photons. *Nuclear Science, IEEE Transactions on*, 28(1):131 –136.

[Derenzo, 1986] Derenzo, S. E. (1986). Mathematical removal of positron range blurring in hight resolution tomography. *IEEE Trans. Nucl. Sci.*, 33:546–49.

[Descourt et al., 2008] Descourt, P., Du, Y., Song, X., Frey, E., Tsui, B., and Visvikis, D. (2008). Angular response function parameterization for collimator/detector in SPECT simulations within the GATE toolkit. In *IEEE Nucl. Sci. Symp. Conf. Record*, pages 4969–4971.

[Enghardt et al., 2004] Enghardt, W., Crespo, P., Fiedler, F., Hinz, R., Parodi, K., Pawelke, J., and Pnisch, F. (2004). Charged hadron tumour therapy monitoring by means of PET. *Nuclear Instruments and Methods in Physics Research Section A: Accelerators, Spectrometers, Detectors and Associated Equipment*, 525(1-2):284 – 288. Proceedings of the International Conference on Imaging Techniques in Subatomic Physics, Astrophysics, Medicine, Biology and Industry.

[Espana et al., 2009] Espana, S., Herraiz, J. L., Vicente, E., Vaquero, J. J., Desco, M., and Udias, J. M. (2009). PeneloPET, a Monte Carlo PET simulation tool based on PENELOPE: features and validation. *Physics in Medicine and Biology*, 54(6):1723.

[Ferreira et al., 2000] Ferreira, N., Trebossen, R., Comtat, C., Gregoire, M.-C., and Bendriem, B. (2000). Iterative crystal efficiency calculation in fully 3-D PET. *IEEE Trans. Med. Imag.*, 19:485–92.

[Fessler, 1994] Fessler, J. A. (1994). Penalized weighted least-squares image reconstruction for positron emission tomography. *IEEE Trans. Med. Img.*, 13(2):290–300.

[Fessler, 2010] Fessler, J. A. (2010). Image reconstruction toolbox (matlab).

[Frey et al., 1993] Frey, E., Ju, Z.-W., and Tsui, B. (1993). A fast projector-backprojector pair modeling the asymmetric,spatially varying scatter response function for scatter compensation in SPECT imaging. *IEEE Trans. Nucl. Sci.*, 40(4):1192–1197.

[Ganan and McClure, 1985] Ganan, S. and McClure, D. (1985). Bayesian image analysis: an application to single photon emission tomography. In *Proc. of Stat. Comp. Sect. of Amer. Stat. Assoc.*, pages 12–20.

[Gordon et al., 1970] Gordon, R., Bender, R., and Herman, G. T. (1970). Algebraic Reconstruction Techniques (ART) for three-dimensional electron microscopy and X-ray photography. *Journal of Theoretical Biology*, 29(3):471 – 481.

[Gray and Macovski, 1976] Gray, R. M. and Macovski, A. (1976). Maximum a posteriori estimation of position in scintillation cameras. *IEEE Trans. Nucl. Sci.*, 23(1):849–852.

[Harrison et al., 2002] Harrison, R., Dhavala, S., Kumar, P., Shao, Y., Manjersshwar, R., Lewellen, T., and Jansen, F. (2002). Acceleration of SimSET photon history generation. In *Nuclear Science Symposium Conference Record, 2002 IEEE*, volume 3, pages 1835 – 1838 vol.3.

[Harrison et al., 1999] Harrison, R. L., Kaplan, M. S., Vannoy, S. D., and Lewellen, T. K. (1999). Positron range and coincidence non-collinearity in SimSET. *IEEE Nucl. Sci. Symp. Conf. Record*, 3:1265–8.

[Haynor et al., 1991] Haynor, D. R., Harrison, R. L., and Lewellen, T. K. (1991). The use of importance sampling techniques to improve the efficiency of photon tracking in emission tomography simulations. *Med. Phys.*, 18(5):990–1001.

[Hebert et al., 1990] Hebert, S. F., Derenzo, S. E., and Uber, D. (1990). Application of mathematical removal of positron range blurring in positron emission tomography. *IEEE Trans. Nucl. Sci.*, 37:1293–99.

[Herman, 1995] Herman, G. T. (1995). Image reconstruction from projections. *Real-Time Imaging*, 1(1):3 – 18.

[Herraiz et al., 2006] Herraiz, J. L., Espana, S., Vaquero, J. J., Desco, M., and Udias, J. M. (2006). FIRST: Fast Iterative Reconstruction Software for (PET) tomography. *Phys. in Med. and Biol.*, 51(18):4547–4565.

[Holdsworth et al., 2003] Holdsworth, C., Badawi, R., Santos, P., Van den Abbeele, A., Hoffman, E., and El Fakhri, G. (2003). Evaluation of a Monte Carlo scatter correction in clinical 3D PET. In *Nuclear Science Symposium Conference Record, 2003 IEEE*, volume 4, pages 2540 – 2544 Vol.4.

[Hornak, 2002] Hornak, J. P. (2002). *Encyclopedia of Imaging Science and Technology*. John Wiley & Sons, Inc.

[Hudson and Larkin, 1994] Hudson, H. and Larkin, R. (1994). Accelerated image reconstruction using ordered subsets of projection data. *Medical Imaging, IEEE Transactions on*, 13(4):601 –609.

[Iwata et al., 1997] Iwata, K., Greaves, R. G., and Surko, C. M. (1997). γ-ray spectra from positron annihilation on atoms and molecules. *Phys. Review A*, 55(5):3585–3604.

[James et al., 2010] James, S. S., Yang, Y., Bowen, S. L., Qi, J., and Cherry, S. R. (2010). Simulation study of spatial resolution and sensitivity for the tapered depth of interaction PET detectors for small animal imaging. *Physics in Medicine and Biology*, 55(2):N63.

[Jan et al., 2004] Jan, S., Santin, G., Strul, D., Staelens, S., and et al. (2004). GATE: a simulation toolkit for PET and SPECT. *Phys. in Med. and Biol.*, 49:4543–4561.

[Johnson et al., 1995] Johnson, C. A., Yan, Y., Carson, R., Martino, R., and Daube-Witherspoon, M. (1995). A system for the 3D reconstruction of retracted-septa PET data using the EM algorithm. *IEEE Trans. Nucl. Sci.*, 42:1223–1227.

[Joung et al., 2001] Joung, J., Miyaoka, R., and Lewellen, T. (2001). cMiCE:a high resolution animal PET using continuous LSO with a statistics based positioning scheme. In *Nuclear Science Symposium Conference Record, 2001 IEEE*, volume 2, pages 1137 – 1141 vol.2.

[Kadrmas, 2004] Kadrmas, D. J. (2004). LOR-OSEM: statistical PET reconstruction from raw line-of-response histograms. *Phys. in Med. and Biol.*, 49(20):4731–4744.

[Kak and Slaney, 2001] Kak, A. C. and Slaney, M. (2001). *Principles of Computerized Tomographic Imaging*. Society of Industrial and Applied Mathematics, S. Haykin, Ed. Englewood Cliffs, NJ.

[Kallergi et al., 1992] Kallergi, M., Qian, W., Clarke, L. P., and Gondeck, A. R. (1992). Bremsstrahlung imaging with the gamma camera. In R. Shaw, editor, *Society of Photo-Optical Instrumentation Engineers (SPIE) Conference Series*, volume 1651 of *Society of Photo-Optical Instrumentation Engineers (SPIE) Conference Series*, pages 212–221.

[Kamel et al., 2003] Kamel, E. M., Burger, C., Buck, A., von Schulthess, G. K., and Goerres, G. W. (2003). Impact of metallic dental implants on CT-based attenuation correction in a combined PET/CT scanner. *European Radiology*, 13(4):724–728.

[Karp et al., 1995] Karp, J. S., Muehllehnert, G., Qui, H., and Yans, X.-H. (1995). Singles transmission in volume-imaging PET with a 137Cs source. *Phys. Med. Biol.*, 40:929–944.

[Karp et al., 2008] Karp, J. S., Surti, S., Daube-Witherspoon, M. E., and Muehllehner, G. (2008). Benefit of Time-of-Flight in PET: Experimental and Clinical Results. *J Nucl Med*, 49(3):462–470.

[Kawrakow et al., 2008a] Kawrakow, I., Gerganov, G., Zhang, L., Madzhunkov, Y., Mitev, K., Schmidtlein, C. R., and Kirov, A. S. (2008a). Verification of a Fast EGSnrc Based Application for Positron Emission Tomography Simulations. In *Abstract book of of the IEEE Nuclear Science Symposium and Medical Imaging Conference*.

[Kawrakow et al., 2009] Kawrakow, I., Mainegra-Hing, E., Tessier, F., and Walters, B. (2009). The EGSnrc C++ class library. Technical Report NRC Report PIRS-898 (rev A), National Research Council, Canada.

[Kawrakow et al., 2008b] Kawrakow, I., Mitev, K., Gerganov, G., Madzhunkov, J., and Kirov, A. (2008b). Efficient photon transport in positron emission tomography simulations using VMC ++. *Journal of Physics: Conference Series*, 102(1):012014.

[Kawrakow et al., 2008c] Kawrakow, I., Mitev, K., Gerganov, G., Madzhunkov, J., and Kirov, A. (2008c). SU-GG-I-109: Using EGSnrc Within GATE to Improve the Efficiency Of positron Emission Tomography Simulations. In *AAPM 50th Meeting : abstracts (Houston, Texas, USA, July 27-31, 2008)*, volume 35, pages 2667–2667. AAPM.

[Kawrakow and Rogers, 2007] Kawrakow, I. and Rogers, D. (2007). The EGSnrc Code System: Monte Carlo Simulation of Electron and Photon Transport. Technical Report PRIS_701, National Research Council of Canada.

[Keereman et al., 2010] Keereman, V., Fierens, Y., Broux, T., De Deene, Y., Lonneux, M., and Vandenberghe, S. (2010). MRI-Based Attenuation Correction for PET/MRI Using Ultrashort Echo Time Sequences. *J Nucl Med*, 51(5):812–818.

[Kim et al., 2005] Kim, J.-H., Czernin, J., Allen-Auerbach, M. S., Halpern, B. S., Fueger, B. J., Hecht, J. R., Ratib, O., Phelps, M. E., and Weber, W. A. (2005). Comparison Between 18F-FDG PET, In-Line PET/CT, and Software Fusion for Restaging of Recurrent Colorectal Cancer. *J Nucl Med*, 46:587–595.

[Kinahan et al., 1998] Kinahan, P. E., Townsend, D. W., Beyer, T., and Sashin, D. (1998). Attenuation correction for a combined 3D PET/CT scanner. *Med. Phys.*, 25(10):2046–2053.

[Kops et al., 2007] Kops, E., Qin, P., Mller-Veggian, M., and Herzog, H. (2007). MRI Based Attenuation Correction for Brain PET Images. In Buzug, T. M.,

Holz, D., Bongartz, J., Kohl-Bareis, M., Hartmann, U., and Weber, S., editors, *Advances in Medical Engineering*, volume 114 of *Springer Proceedings in Physics*, pages 93–97. Springer Berlin Heidelberg. 10.1007/978-3-540-68764-1_15.

[Lamare et al., 2006] Lamare, F., Turzo, A., Bizais, Y., Rest, C. C. L., and Visviks, D. (2006). Validation of a Monte Carlo simulation of the Philips Allegro Gemini PET system using GATE. *Phys. in Med. and Biol.*, 51:943–962.

[Lange and Carson, 1984] Lange, K. and Carson, R. (1984). EM reconstruction algorithms for emission and transmission tomography. *J. Comput. Asst. Tomogr.*, 8(2):306–316.

[Lecoq et al., 2010] Lecoq, P., Auffray, E., Brunner, S., Hillemanns, H., Jarron, P., Knapitsch, A., Meyer, T., and Powolny, F. (2010). Factors Influencing Time Resolution of Scintillators and Ways to Improve Them. *Nuclear Science, IEEE Transactions on*, 57(5):2411 –2416.

[Leroux et al., 2007a] Leroux, J.-D., Selivanov, V., Fontaine, R., and Lecomte, R. (2007a). Accelerated iterative image reconstruction methods based on block-circulant system matrix derived from a cylindrical image representation. In *Nuclear Science Symposium Conference Record, 2007. NSS '07. IEEE*, volume 4, pages 2764 –2771.

[Leroux et al., 2007b] Leroux, J.-D., Thibaudeau, C., Lecomte, R., and Fontaine, R. (2007b). Fast, accurate and versatile Monte Carlo method for computing system matrix. In *Nuclear Science Symposium Conference Record, 2007. NSS '07. IEEE*, volume 5, pages 3644 –3648.

[Levenberg, 1944] Levenberg, K. (1944). A Method for the Solution of Certain Non-Linear Problems in Least Squares. *The Quarterly of Applied Mathematics*, 2:164168.

[Levin, 2008] Levin, C. (2008). New imaging technologies to enhance the molecular sensitivity of positron emission tomography. *Proceedings of the IEEE*, 96(3):439 –467.

[Levin and Hoffman, 1999] Levin, C. and Hoffman, E. (1999). Calculation of positron range and its effect on the fundamental limit of positron emission tomography system spatial resolution. *Phys. in Med. and Biol.*, 44(3):781–799.

[Lewellen et al., 1998] Lewellen, T., Harrison, R., and S., V. (1998). *Monte Carlo simulations in nuclear medicine, Ljungberg, M and Strand, SE and King, MA, editors*, chapter The SimSET program, pages 77–92. IOP Publishin, Bristol, Philadelphia.

[Lewitt, 1992] Lewitt, R. (March 1992). Alternatives to voxels for image representation in iterative reconstruction algorithms. *Phys. in Med. and Biol.*, 37(3):705–716.

[Lewitt and Samuel, 2003] Lewitt, R. M. and Samuel, M. (2003). Overview of methods for image reconstruction from projections in emission computed tomography. *Proc. of the IEEE*, 10:1588–1611.

[Liu et al., 2006] Liu, H., Tian, Y., and Shi, P. (2006). Simultaneous Estimation of PET Attenuation and Activity Images with Divided Difference Filters. In Yang, G.-Z., Jiang, T., Shen, D., Gu, L., and Yang, J., editors, *Medical Imaging and Augmented Reality*, volume 4091 of *Lecture Notes in Computer Science*, pages 301–308. Springer Berlin / Heidelberg. 10.1007/11812715_38.

[Lourakis, 2004] Lourakis, M. (Jul. 2004). levmar: Levenberg-Marquardt nonlinear least squares algorithms in C/C++. [web page] http://www.ics.forth.gr/~lourakis/levmar/ . [Accessed on 31 Jan. 2005.].

[Marquardt, 1963] Marquardt, D. (1963). An Algorithm for Least-Squares Estimation of Nonlinear Parameters. *SIAM Journal on Applied Mathematics*, 11(11):431441.

[Matej and Lewitt, 1995] Matej, S. and Lewitt, R. M. (1995). Efficient 3D grids for image reconstruction in using spherically-symmetric volume elements. *IEEE Trans Nucl. Sci.*, 43:1361–70.

[Matej and Lewitt, 1996] Matej, S. and Lewitt, R. M. (1996). Practical Considerations for 3-D Image Reconstruction Using Spherically Symmetric Volume Elements. *IEEE Trans. on Med. Img.*, 17:68–78.

[Meikle et al., 1995] Meikle, S. R., Bailey, D. L., Hooper, P. K., Eberl, S., Hutton, B. F., Jones, W. F., Fulton, R. R., and Fulham, M. J. (1995). Simultaneous Emission and Transmission Measurements for Attenuation Correction in Whole-Body PET. *J Nucl Med*, 36(9):1680–1688.

[Meikle et al., 1993] Meikle, S. R., Dahlbom, M., and Cherry, S. R. (1993). Attenuation Correction Using Count-Limited Transmission Data in Positron Emission Tomography. *J Nucl Med*, 34(1):143–150.

[Melcher, 2000] Melcher, C. L. (2000). Scintillation Crystals for PET. *J Nucl Med*, 41(6):1051–1055.

[Millet et al., 1996] Millet, P., Delforge, J., Pappata, S., Syrota, A., and Cinotti, L. (1996). Error analysis on parameter estimates in the ligand - receptor model:

application to parameter imaging using PET data. *Physics in Medicine and Biology*, 41(12):2739.

[Mitchell and Netravali, 1988] Mitchell, D. P. and Netravali, A. N. (1988). Reconstruction filters in computer-graphics. In *ACM SIGGRAPH International Conference on Computer Graphics and Interactive Techniques*, volume 22, page 221228.

[Moehrs et al., 2008a] Moehrs, S., Defrise, M., Belcari, N., Guerra, A. D., Bartoli, A., Fabbri, S., and Zanetti, G. (2008a). Multi-ray based system matrix generation for 3D PET reconstruction. *Phys. in Med. and Biol.*, 53(23):6925–6945.

[Moehrs et al., 2008b] Moehrs, S., Defrise, M., Belcari, N., Guerra, A. D., Bartoli, A., Fabbri, S., and Zanetti, G. (2008b). Multi-ray-based system matrix generation for 3D PET reconstruction. *Phys. in Med. and Biol.*, 53(23):6925–6945.

[Moehrs et al., 2006] Moehrs, S., Guerra, A. D., Herbert, D. J., and Mandelkern, M. A. (2006). A detector head design for small-animal PET with silicon photomultipliers (SiPM). *Phys. Med. Biol.*, 51:11131127.

[Montandon and Zaidi, 2005] Montandon, M.-L. and Zaidi, H. (2005). Atlas-guided non-uniform attenuation correction in cerebral 3D PET imaging. *NeuroImage*, 25(1):278 – 286.

[Mora and Rafecas, 2006] Mora, C. and Rafecas, M. (2006). Polar pixels for high resolution small animal PET. In *Nuclear Science Symposium Conference Record, 2006. IEEE*, volume 5, pages 2812 –2817.

[Nishikido et al., 2008] Nishikido, F., Tsuda, T., Yoshida, E., Inadama, N., Shibuya, K., Yamaya, T., Kitamura, K., Takahashi, K., Ohmura, A., and Murayama, H. (2008). Spatial resolution evaluation with a pair of two four-layer DOI detectors for small animal PET scanner: jPET-RD. *Nuclear Instruments and Methods in Physics Research Section A: Accelerators, Spectrometers, Detectors and Associated Equipment*, 584(1):212 – 218.

[Nuyts et al., 1999] Nuyts, J., Dupont, P., Stroobants, S., Benninck, R., Mortelmans, L., and Suetens, P. (1999). Simultaneous maximum a-posteriori reconstruction of attenuation and activity distributions from emission sinograms. *IEEE Trans. Med. Imag.*, 18(5):393–403.

[Ollinger, 1996] Ollinger, J. M. (1996). Model-based scatter correction for fully 3D PET. *Phys. Med. Biol.*, 41:153–176.

[Ortuno et al., 2006] Ortuno, J. E., Guerra, P., Rubio, J. L., Kontaxakis, G., and Santos, A. (2006). 3D OSEM-based iterative image reconstruction for high resolution PET using precalculated system matrix. *Nucl. Instrum. Methods*, 569(2):440.

[Ortuno et al., 2010] Ortuno, J. E., Kontaxakis, G., Rubio, J. L., Guerra, P., and Santos, A. (2010). Efficient methodologies for system matrix modelling in iterative image reconstruction for rotating high-resolution PET. *Physics in Medicine and Biology*, 55(7):1833.

[Otte et al., 2006] Otte, N., Dolgoshein, B., Hose, J., Klemin, S., Lorenz, E., Mirzoyan, R., Popova, E., and Teshima, M. (2006). The SiPM – A new Photon Detector for PET. *Nuclear Physics B - Proceedings Supplements*, 150:417 – 420. Proceedings of the 9th Topical Seminar on Innovative Particle and Radiation Detectors.

[Pan et al., 2005] Pan, T., Mawlawi, O., Nehmeh, S. A., Erdi, Y. E., Luo, D., Liu, H. H., Castillo, R., Mohan, R., Liao, Z., and Macapinlac, H. (2005). Attenuation Correction of PET Images with Respiration-Averaged CT Images in PET/CT. *J Nucl Med*, 46(9):1481–1487.

[Panin et al., 2006a] Panin, V., Kehren, F., Michel, C., and Casey, M. (2006a). Fully 3-D PET reconstruction with system matrix derived from point source measurements. *IEEE Trans. Med. Imag.*, 25(7):907–921.

[Panin et al., 2006b] Panin, V., Kehren, F., Michel, C., and Casey, M. (2006b). PET reconstruction with system matrix derived from point source measurements. *IEEE Trans. Nucl. Sci.*, 53(1):152–159.

[Panin et al., 2006c] Panin, V. Y., Kehren, F., Michel, K., and Casey, M. (2006c). Fully 3-D PET reconstruction with system matrix derived from point source measurements. *IEEE Trans. on Med. Imag.*, 25:907–921.

[Parodi et al., 2005] Parodi, K., Ponisch, F., and Enghardt, W. (2005). Experimental study on the feasibility of in-beam PET for accurate monitoring of proton therapy. *Nuclear Science, IEEE Transactions on*, 52(3):778 – 786.

[Qi and Huesman, 2002] Qi, J. and Huesman, R. H. (2002). Scatter correction for positron emission mammography. *Physics in Medicine and Biology*, 47(15):2759.

[Qi and Huesman, 2005] Qi, J. and Huesman, R. H. (2005). Effect of errors in the system matrix on maximum a posteriori image reconstruction. *Phys. in Med. and Biol.*, 50:3297–3312.

[Qi et al., 1998] Qi, J., Leahy, R. M., Cherry, S. R., Chatziioannou, A., and Farquhar, T. H. (1998). High-resolution 3D Bayesian image reconstruction using the microPET small-animal scanner. *Phys. in Med. and Biol.*, 43:1001–13.

[Rafecas et al., 2004a] Rafecas, M., Mosler, B., Diets, M., Pogl, M., Stamatakis, A., McElroy, D., and Ziegler, S. (2004a). Effect of noise in the probability matrix used for statistical reconstruction of PET data. *IEEE Trans. Nucl. Sci.*, 51(1):149–156.

[Rafecas et al., 2004b] Rafecas, M., Mosler, B., Dietz, M., Pogl, M., Stamatakis, A., McElroy, D. P., and Ziegler, S. I. (2004b). Use of a Monte Carlo-based probability matrix for 3-D iterative reconstruction of MADPET-II data. *IEEE Trans. Nucl. Sci.*, 51:2597–2605.

[Rahmim et al., 2005] Rahmim, A., Cheng, J.-C., and Sossi, V. (2005). Improved noise propagation in statistical image reconstruction with resolution modeling. *IEEE Nucl. Sci. Symp. Conf. Record*, 5:2576–2578.

[Rahmim et al., 2008] Rahmim, A., Tang, J., Lodge, M., Lashkari, S., Ay, M., Lautamaki, R., Tsui, B., and Bengel, F. M. (2008). Analytic system matrix resolution modeling in PET: an application to Rb-82 cardiac imaging. *Phys. in Med. and Biol.*, 53:5947–5965.

[Rannou and Chatziioannou, 2004] Rannou, F. and Chatziioannou, A. (2004). Fully 3D system model estimation of OPET by Monte Carlo simulation. In *Nuclear Science Symposium Conference Record, 2004 IEEE*, volume 6, pages 3433 – 3436 Vol. 6.

[Rault et al., 2008] Rault, E., Vandenberghe, S., Staelens, S., Van Holen, R., and Lemahieu, I. (2008). Optimization of y90 bremsstrahlung image reconstruction using multiple energy window subsets. *J NUCL MED MEETING ABSTRACTS*, 49(MeetingAbstracts_1):399P.

[Reader et al., 2003] Reader, A., Julyan, P., Williams, H., Hastings, D., and Zweit, J. (2003). EM algorithm system modeling by image-space techniques for PET reconstruction. *IEEE Trans. Nucl. Sci.*, 50(5):1392–1397.

[Rehfeld and Alber, 2007] Rehfeld, N. and Alber, M. (2007). A parallelizable compression scheme for Monte Carlo scatter system matrices in PET image reconstruction. *Phys. Med. Biol.*, 52(3):3421–3437.

[Rehfeld et al., 2010] Rehfeld, N. S., Vauclin, S., Stute, S., and Buvat, I. (2010). Multidimensional B-spline parameterization of the detection probability of PET systems to improve the efficiency of Monte Carlo simulations. *Physics in Medicine and Biology*, 55(12):3339.

[Reilhac et al., 2005] Reilhac, A., Batan, G., Michel, C., Grova, C., Tohka, J., Collins, D., Costes, N., and Evans, A. (2005). PET-SORTEO: validation and development of database of Simulated PET volumes. *Nuclear Science, IEEE Transactions on*, 52(5):1321 – 1328.

[Rowe et al., 1993] Rowe, R. K., Aarsvold, J. N., Barrett, H. H., Chen, J.-C., Klein, W. P., Moore, B. A., Pang, I. W., Patton, D. D., and White, T. A. (1993). A stationary hemispherical spect imager for three-dimensional brain imaging. *J Nucl Med*, 34(3):474–480.

[Schaart et al., 2010] Schaart, D. R., Seifert, S., Vinke, R., van Dam, H. T., Dendooven, P., Lhner, H., and Beekman, F. J. (2010). LaBr_3 :Ce and SiPMs for time-of-flight PET: achieving 100 ps coincidence resolving time. *Physics in Medicine and Biology*, 55(7):N179.

[Schaart et al., 2009] Schaart, D. R., van Dam, H. T., Seifert, S., Vinke, R., Dendooven, P., Lohner, H., and Beekman, F. J. (2009). A novel, SiPM-array-based, monolithic scintillator detector for PET. *Phys. Med. Biol.*, 54:35013512.

[Scheins et al., 2006] Scheins, J., Boschen, F., and Herzog, H. (2006). Analytical calculation of volumes-of-intersection for iterative, fully 3-D PET reconstruction. *IEEE Trans. Med. Imag.*, 25(10):1363–1369.

[Scheins and Herzog, 2008] Scheins, J. J. and Herzog, H. (2008). PET Reconstruction Software Toolkit - PRESTO a novel, universal C++ library for fast, iterative, fully 3D PET image reconstruction using highly compressed, memory-resident system matrices. In *Nuclear Science Symposium Conference Record, 2008. NSS '08. IEEE*, pages 4147 –4150.

[Schreibmann et al., 2010] Schreibmann, E., Nye, J. A., Schuster, D. M., Martin, D. R., Votaw, J., and Fox, T. (2010). MR-based attenuation correction for hybrid PET-MR brain imaging systems using deformable image registration. *Medical Physics*, 37(5):2101–2109.

[Selivanov et al., 2000] Selivanov, V., Picard, Y., Cadorette, J., Rodrigue, S., and Lecomte, R. (2000). Detector response models for statistical iterative image reconstruction in high resolution PET. *IEEE Trans. Nucl. Sci.*, 47(3):1168–1175.

[Shepp and Vardi, 1982] Shepp, L. and Vardi, Y. (1982). Maximum likelihood reconstruction for emission tomography. *IEEE Trans. Med. Imag.*, 1:113–122.

[Shokouhi et al., 2004] Shokouhi, S., Vaska, P., Southekal, S., Schlyer, D., Purschke, M., Dzordzhadze, V., Woody, C., Stoll, S., Alexoff, D. L., Rubins,

D., Villanueva, A., and Krishnamoorthy, S. (2004). Statistical 3D image reconstruction for the RatCAP PET tomography using a physically accurate, Monte Carlo based system matrix. *IEEE Nucl. Sci. Symp. Conf. Record*, 6:3901–3905.

[Siddon, 1985] Siddon, R. (1985). Fast calculation of the exact radiological path for a three-dimensional CT array. *Med. Phys.*, 12(2):252–255.

[Snyder et al., 1987] Snyder, D. L., Miller, M. I., Thomas, L. J., and Politte, D. G. (1987). Noise and Edge Artifacts in Maximum-Likelihood Reconstructions for Emission Tomography. *IEEE Trans. Med. Imag.*, 6(3):228–238.

[Staelens et al., 2004] Staelens, S., Strul, D., Santin, G., Vandenberghe, S., Koole, M., D'Assler, Y., Lemahieu, I., and de Walle, R. V. (2004). A three-dimensional theoretical model incorporating spatial detection uncertainty in continuous detector PET. *Phys. in Med. and Biol.*, 49:2337–2350.

[Sureau et al., 2008] Sureau, F. C., Reader, A. J., Comtat, C., Leroy, C., Ribeiro, M., Buvat, I., and Trebossen, R. (2008). Impact of image-space resolution modeling for studies with the High-Resolution Research Tomography. *J. Nucl Med.*, 49:1000–8.

[Surti and Karp, 2004] Surti, S. and Karp, J. S. (2004). Imaging characteristics of a 3-dimensional GSO whole-body PET camera. *J. Nucl. Medi.*, 45:1040–49.

[Tai et al., 2008] Tai, Y.-C., Wu, H., Pal, D., and O'Sullivan, J. A. (2008). Virtual-Pinhole PET. *J Nucl Med*, 49(3):471–479.

[Tang et al., 2008] Tang, J., Rahmim, A., Lautamaki, R., Lodge, M., Bengel, F., and Tsui, B. M. W. (2008). Optimization of dynamic Rb-82 PET cardiac acquisition protocol using Monte-Carlo simulation. *J NUCL MED MEETING ABSTRACTS*, 49(MeetingAbstracts_1):63P-c-.

[Tenney et al., 2004] Tenney, C., Bowsher, J., and Jaszczak, R. (2004). A delta-scatter Monte Carlo model of a rotating parallel-hole collimator for 131I brain tumor imaging. In *Nuclear Science Symposium Conference Record, 2004 IEEE*, volume 5, pages 3084 –3088.

[Terstegge et al., 1996] Terstegge, A., Weber, S., Herzog, H., Muller-Gartner, H., and Halling, H. (1996). High resolution and better quantification by tube of response modelling in 3D PET reconstruction. *IEEE Nucl. Sci. Symp. Conf. Record*, 3:1603–1607 vol.3.

[Thompson et al., 1992] Thompson, C. J., Moreno-Cantu, J., and Picard, Y. (1992). PETSIM: Monte Carlo simulation of all sensitivity and resolution parameters of cylindrical positron imaging systems. *Physics in Medicine and Biology*, 37(3):731.

[Tohme and Qi, 2009] Tohme, M. S. and Qi, J. (2009). Iterative image reconstruction for positron emission tomography based on a detector response function estimated from point source measurements. *Phys. in Medi. and Biol.*, 54:3709–3725.

[van der Have et al., 2008] van der Have, F., Vastenhouw, B., Rentmeester, M., and Beekman, F. (2008). System Calibration and Statistical Image Reconstruction for Ultra-High Resolution Stationary Pinhole SPECT. *Medical Imaging, IEEE Transactions on*, 27(7):960 –971.

[Vandenberghe et al., 2001] Vandenberghe, S., D'Asseler, Y., den Walle, R. V., Kauppinen, T., Koole, M., Bouwens, L., Laere, K. V., Lemahieu, I., and Dierckx, R. (2001). Iterative reconstruction algorithms in nuclear medicine. *Comput. Med. Imag. Graph.*, 25(2):105–111.

[Vandenberghe et al., 2006] Vandenberghe, S., Staelens, S., Byrne, C. L., Soares, E. J., Lemahieu, I., and Glick, S. J. (2006). Reconstruction of 2D PET data with Monte Carlo generated system matrix for generalized natural pixels. *Phys. in Med. and Biol.*, 51:3105–3125.

[Vanhove et al., 2007] Vanhove, C., Andreyev, A., Defrise, M., Nuyts, J., and Bossuyt, A. (Feb 2007). Resolution recovery in pinhole SPECT based on multi-ray projections: a phantom study. *Eur. J. Nucl. Med. Mol. Imag.*, 34(2).

[Verhaeghe et al., 2008] Verhaeghe, J., Van De Ville, D., Khalidov, I., DAsseler, Y., Lemahieu, I., and Unser, M. (2008). Dynamic PET Reconstruction Using Wavelet Regularization With Adapted Basis Functions. *IEEE Trans. Med. Imag.*, 27(7):943–59.

[Vinke et al., 2010] Vinke, R., Lohner, H., Schaart, D., van Dam, H., Seifert, S., Beekman, F., and Dendooven, P. (2010). Time walk correction for TOF-PET detectors based on a monolithic scintillation crystal coupled to a photosensor array. *Nuclear Instruments and Methods in Physics Research Section A: Accelerators, Spectrometers, Detectors and Associated Equipment*, 621(1-3):595 – 604.

[Wallis and Miller, 1997] Wallis, J. and Miller, T. (1997). An optimal rotator for iterative reconstruction. *IEEE Trans. Med. Imag.*, 16(1):118–123.

[Wang and Qi, 2009] Wang, G. and Qi, J. (2009). Generalized Algorithms for Direct Reconstruction of Parametric Images From Dynamic PET Data. *Medical Imaging, IEEE Transactions on*, 28(11):1717 –1726.

[Wang et al., 2004] Wang, W., Hawkins, W., and Gagnon, D. (2004). 3D RBI-EM reconstruction with spherically-symmetric basis function for SPECT rotating slat collimator. *Physics in Medicine and Biology*, 49(11):2273.

[Wang et al., 2007] Wang, W., Hu, Z., and Gagnon, D. (2007). A New Component Approach to Efficiency Normalization for 3D PET. *Nuclear Science, IEEE Transactions on*, 54(1):92 –99.

[Watson et al., 1997] Watson, C., Newport, D., Casey, M., deKemp, R., Beanlands, R., and Schmand, M. (1997). Evaluation of simulation-based scatter correction for 3-D PET cardiac imaging. *IEEE Trans. Nucl. Sci.*, 44:90–97.

[Werling et al., 2002] Werling, A., Bublitz, O., Doll, J., Adam, L.-E., and Brix, G. (2002). Fast implementation of the single scatter simulation algorithm and its use in iterative image reconstruction of PET data. *Physics in Medicine and Biology*, 47(16):2947.

[Wernick and Aarsvold, 2004] Wernick, M. N. and Aarsvold, J. N. (2004). *Emission Tomography - the fundamentals of PET and SPECT*. Elsevier Academic Press, 525 B Street, Suite 1900, San Diego, California 92101-4495, USA.

[Wiant et al., 2010] Wiant, D., Gersh, J. A., Bennett, M., and Bourland, J. (2010). Evaluation of the spatial dependence of the point spread function in 2D PET image reconstruction using LOR-OSEM. *Med. Phys.*, 37(3):1169–82.

[Wollenweber et al., 2000] Wollenweber, S., Kohlmyer, S., and Lewellen, T. (2000). Evaluation of model-based scatter correction accuracy using Monte Carlo calculated phantom inputs. In *Nuclear Science Symposium Conference Record, 2000 IEEE*, volume 2, pages 13/42 –13/46 vol.2.

[Woodcock et al., 1965] Woodcock, E., Murphy, T., Hemmings, P., and Longworth, T. (1965). Techniques Used in the GEM Code for Monte Carlo Neutronics Calculations in Reactors and Other Systems of Complex Geometry. In *Proc. Conf. Applications of Computing Methods to Reactor Problems, ANL-7050, pagep. 557, Argonne National Laboratory*.

[Yang et al., 2011] Yang, Y., James, S. S., Wu, Y., Du, H., Qi, J., Farrell, R., Dokhale, P. A., Shah, K. S., Vaigneur, K., and Cherry, S. R. (2011). Tapered LSO arrays for small animal PET. *Physics in Medicine and Biology*, 56(1):139.

[Zaidi, 1999] Zaidi, H. (1999). Relevance of accurate Monte Carlo modeling in nuclear medical imaging. *Med. Phys.*, 26(4):574 – 608.

[Zeng et al., 1994a] Zeng, G., Gullberg, G., and Huesman, R. (1994a). Using linear time-invariant system theory to estimate kinetic parameters directly from projection measurements. In *Nuclear Science Symposium and Medical Imaging Conference, 1994., 1994 IEEE Conference Record*, volume 4, pages 1739 – 1743 vol.4.

[Zeng et al., 1994b] Zeng, G., Hsieh, Y., and Gullbergand, G. (1994b). A rotating and warping projector/backprojector for fan-beam and cone-beam iterative algorithm. *IEEE Trans. Nucl. Sci.*, 41:2807–2818.

[Zhang and Zeng, 2006] Zhang, B. and Zeng, G. L. (2006). An immediate after-backprojection filtering method with blob-shaped window functions for voxel-based iterative reconstruction. *Phys. in Med. and Biol.*, 51:5825–5842.

[Zhang et al., 2010a] Zhang, H., Bao, Q., Vu, N., Silverman, R., Taschereau, R., Berry-Pusey, B., Douraghy, A., Rannou, F., Stout, D., and Chatziioannou, A. (2010a). Performance evaluation of petbox: A low cost bench top preclinical pet scanner. *Molecular Imaging and Biology*, pages 1–13. 10.1007/s11307-010-0413-y.

[Zhang, 2008] Zhang, L. (2008). Monte Carlo based reconstruction using a rotator for 2-D PET data. In *9e UGent-FirW doctoraatssymposium*.

[Zhang et al., 2010b] Zhang, L., De Beenhouwer, J., Staelens, S., Kawrakow, I., and Vandenberghe, S. (2010b). Efficiency improvement in System Matrix Simulation of PET. *Trans. Nucl. Sci.* In preparation.

[Zhang et al., 2010c] Zhang, L., Staelens, S., Van Holen, R., De Beenhouwer, J., Verhaeghe, J., Kawrakow, I., and Vandenberghe, S. (2010c). Fast and memory efficient Monte Carlo based image reconstruction for whole body PET. *Med. Phys.*, 37(7):3667–3676.

[Zhang et al., 2010d] Zhang, L., Staelens, S., Van Holen, R., Verhaeghe, J., and Vandenberghe, S. (2010d). Characterization of the Ringing Artifacts in Rotator-based Reconstruction with Monte Carlo-based Resolution Compensation for PET. *Med. Phys.*, 37:4648–4660.

[Zhang et al., 2008] Zhang, L., Vandenberghe, S., Staelens, S., Verhaeghe, J., Kawrakow, I., and Lemahieu, I. (2008). Monte-Carlo system modeling for PET reconstruction: a rotator approach. In *Proceedings of the IEEE Nuclear Science Symposium and Medical Imaging Conference*.

Publication list

Journal Publications

- **L. Zhang**, S. Staelens, R. Van Holen, J. Verhaeghe, and S. Vandenberghe, "Characterization of the Ringing Artifacts in Rotator-based Reconstruction with Monte Carlo-based Resolution Compensation for PET," *Medical Physics*, Vol. 37, no. 9, pp. 4648–4660, 2010.
- **L. Zhang**, S. Staelens, R. Van Holen, J. De Beenhouwer, J. Verhaeghe, I. Kawrakow, and S. Vandenberghe, "Fast and memory-efficient Monte Carlo-based image reconstruction for whole body PET," *Medical Physics*, Vol. 37, no. 7, pp. 3667–3676, 2010.
- **L. Zhang**, I. Kawrakow, J. De Beenhouwer, S. Staelens, and S. Vandenberghe, "Efficiency improvement in System Matrix Simulation of PET," *Med. Phys.*, 2011, in preparation.
- **L. Zhang**, R. Van Holen, S. Staelens, S. Vandenberghe, "Experimental Resolution Compensation for Fully 3-D Reconstruction of PET Data," *Med. Phys.*, 2011, in preparation.

Conference Publications

- **L. Zhang**, R. Van Holen, S. Staelens, and S. Vandenberghe, "Experimental PSF Modeling for Fully 3-D PET Reconstruction," *Fully Three-Dimensional Image Reconstruction in Radiology and Nuclear Medicine*, accepted, 2011
- **L. Zhang**, S. Vandenberghe, S. Staelens, J. Verhaeghe, I. Kawrakow, and I. Lemahieu, "Monte-Carlo system modeling for PET reconstruction: a rotator approach," in *Proceedings of the IEEE Nuclear Science Symposium and Medical Imaging Conference*, pp. 5101–5106, 2008.
- **L. Zhang**, S. Vandenberghe, S. Staelens, S. Glick, Y. D'Asseler, and I. Lemahieu, "PET reconstruction with Monte Carlo generated system matrix for strip blobs," in *Proceedings 9th International Meeting on Fully Three-Dimensional Image Reconstruction in Radiology and Nuclear Medicine*, pp. 301–304, 2007.
- **L. Zhang**, S. Vandenberghe, S. Staelens, and I. Lemahieu, "A penalized algebraic reconstruction technique (pART) for PET image reconstruction," in *Proceedings of the IEEE Nuclear Science Symposium*, pp. 3859–3864, 2007.
- I. Kawrakow, G. Gerganov, **L. Zhang**, Y. Madzhunkov, K. Mitev, C. R. Schmidtlein, and A. S. Kirov, "Verification of a Fast EGSnrc Based Application for Positron Emission Tomography Simulations," in *Abstract book of the IEEE Nuclear Science Symposium and Medical Imaging Conference*, pp. 369–369, 2008.
- J. Verhaeghe, X. Zhao, S. Vandenberghe, **L. Zhang**, S. Staelens, Y. D'Asseler, and I. Lemahieu, "Use of a Stereo-Vision System for Head Motion Correction for PET Acquisitions," in *Abstract book of 4th International Conference on Imaging Technologies in Biomedical Sciences*, pp. 41–41, 2007.
- **L. Zhang**, "Monte carlo based reconstruction using a rotator for 2-D PET data," in *9e UGent-FirW doctoraatssymposium*, pp. 98–99, 2008.
- **L. Zhang**, S. Vandenberghe, S. Staelens, and I. Lemahieu, "Strip blob for Monte Carlo-based PET imaging reconstruction." in

Abstracts 7th Belgian Day on Biomedical Engineering, pp. 51–51, 2007.

- **L. Zhang**, S. Vandenberghe, S. Staelens, and I. Lemahieu, "Strip blob for Monte Carlo-based Reconstruction," in *8e UGent-FirW doctoraatssymposium*, pp. 83–83, 2007.